



**IMPROVED MULTINUCLIDE IMAGING OF SPECIAL NUCLEAR MATERIAL
USING A HIGH PURITY GERMANIUM DOUBLE SIDED STRIP DETECTOR**

THESIS

Fred D. Rothenbush Jr., Captain, USA
AFIT/GNE/ENP/05-09

**DEPARTMENT OF THE AIR FORCE
AIR UNIVERSITY**

AIR FORCE INSTITUTE OF TECHNOLOGY

Wright-Patterson Air Force Base, Ohio

APPROVED FOR PUBLIC RELEASE; DISTRIBUTION UNLIMITED

The views expressed in this thesis are those of the author and do not reflect the official policy or position of the United States Air Force, Department of Defense, or the United States Government.

AFIT/GNE/ENP/05-09

IMPROVED MULTINUCLIDE IMAGING OF SPECIAL NUCLEAR MATERIAL
USING A HIGH PURITY GERMANIUM DOUBLE SIDED STRIP DETECTOR

THESIS

Presented to the Faculty

Department of Engineering Physics

Graduate School of Engineering and Management

Air Force Institute of Technology

Air University

Air Education and Training Command

In Partial Fulfillment of the Requirements for the

Degree of Master of Science (Nuclear Science)

Fred D. Rothenbush Jr., BS

Captain, USA

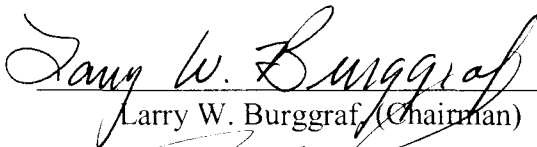
June 2005

APPROVED FOR PUBLIC RELEASE; DISTRIBUTION UNLIMITED

IMPROVED MULTINUCLIDE IMAGING OF SPECIAL NUCLEAR MATERIAL
USING A HIGH PURITY GERMANIUM DOUBLE SIDED STRIP DETECTOR

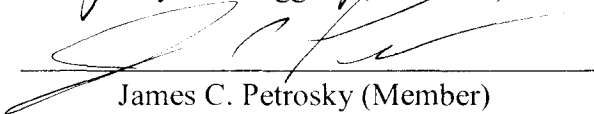
Fred D. Rothenbush Jr., BS
Captain, USA

Approved:



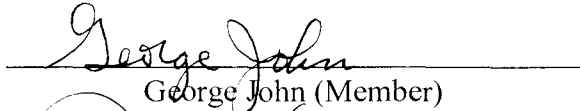
Larry W. Burggraf, (Chairman)

23 May 05
date



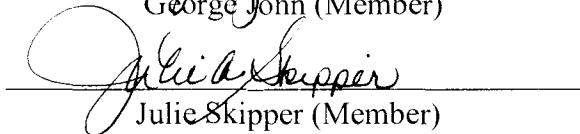
James C. Petrosky (Member)

20 May 05
date



George John (Member)

20 May 05
date



Julie Skipper (Member)

20 MAY 2005
date

Abstract

The purpose of this research is to improve the ability to image Special Nuclear Material (SNM) using a High Purity Germanium Double Sided Strip Detector (HPGeDSSD) for use in the field of nuclear nonproliferation. When used for gamma spectrometry, HPGe detectors can efficiently distinguish various isotopes because of their good energy resolution. The detector used for this research is a liquid nitrogen cooled germanium detector with five charge collection strips on each face. The strips are orthogonal to each other, creating a five by five array of data collection pixels. When the 25 mm by 25 mm detector array is coupled to a converging collimator an imaging system is achieved which provides the ability to image SNM sources which are larger than the detector crystal. For this work, an ideal converging collimator was designed, built and employed. The new collimator provided proper spatial resolution of all sources tested while still providing sufficient efficiency for imaging. Another system improvement is the addition of an OR gate which provides proper timing information, resulting in the ability to image using three strip events for the first time. A new image processing code was developed which employs the ability to use three strip events while reducing the time required to produce an image from approximately five hours down to less than a minute. Additionally, the new code demonstrates the ability to distinguish between multiple isotope sources in a single image through the simultaneous use of multiple energy windows. The system improvements developed during this work combine to improve the overall efficiency and flexibility of the imaging system. The capability to distinguish a

point source from a distributed source, with proper spatial resolution, was demonstrated.

This ability is the primary goal for developing this technology.

Acknowledgments

I would like to express my sincere appreciation to my faculty advisor, Dr. Burggraf, for his guidance and support throughout the course of my thesis effort. His insight and willingness to share his experience are highly appreciated. The other members of my thesis committee, including Dr. James Petrosky, Dr. George John and Dr. Julie Skipper, were very helpful in being able to maintain a focus on the purpose of my research. Cliff Sulham provided me immeasurable guidance on what he learned during his past work with the detector system. His sharing of information saved me weeks worth of trial and error experimentation. I would also like to thank the Defense Threat Reduction Agency for sponsoring this effort. Their willingness to provide finances and basic guidance for the work laid a good foundation to build on.

A special thanks goes to Mr. Bill Keller, Mr. Jim Lewis at Superior Machining and the entire staff in the AFIT model fabrication shop for their support in designing and building the mold for my collimator. Their persistence was crucial to meeting the required timeline. Mr. Hui Tan, X-ray Instruments Associates, provided me key information which allowed me to better utilize the equipment I had available.

Also, a special thanks goes to my fellow classmates who were always open to answering questions and giving me a common sense check on many of my ideas. Finally, my greatest thanks must go to my wife and three children for their unending support as I put in long hours to complete this research, none of it could have been done without their support.

Fred D. Rothenbush Jr.

Table of Contents

| | Page |
|---|------|
| Abstract..... | iv |
| Acknowledgments..... | vi |
| List of Figures..... | ix |
| List of Tables..... | xii |
| I. Introduction | 1 |
| Motivation | 1 |
| Background..... | 2 |
| Objective..... | 6 |
| Scope | 8 |
| Assumptions | 9 |
| General Approach..... | 9 |
| Sequence of Presentation..... | 9 |
| II. Theory | 11 |
| Chapter Overview..... | 11 |
| Germanium Detectors [6]..... | 11 |
| Strip Detectors | 15 |
| Imaging Using a Strip Detector..... | 17 |
| Image Analysis [13] | 21 |
| Weapon Assumptions..... | 22 |
| III. Equipment | 25 |
| Chapter Overview..... | 25 |
| Detector [10][14]..... | 26 |
| DGF Hardware [17]..... | 29 |
| Power Distribution Module [16] | 31 |
| Crate and Crate Controller [5][16] | 31 |
| Collimator..... | 32 |
| Image Processing Code | 33 |
| Radiation Sources..... | 35 |
| Controlling Software / SCSI Interface | 39 |
| IV. Procedure..... | 40 |
| Chapter Overview..... | 40 |
| Collimator Design and Fabrication | 40 |
| Equipment Setup | 47 |
| Noise..... | 51 |

| | |
|--|-----|
| Charge Sharing Between Strips..... | 51 |
| Software Settings..... | 51 |
| Resolution Determination..... | 53 |
| Efficiency Calculation..... | 53 |
| Collimator Alignment..... | 54 |
| Imaging..... | 56 |
| V. Results | 58 |
| Chapter Overview..... | 58 |
| Noise..... | 58 |
| Charge Collection/Sharing | 59 |
| Preamplifier Decay Constant (TAU)..... | 61 |
| Energy Calibration..... | 62 |
| Rise Time Optimization | 64 |
| Energy Resolution of the Detector | 66 |
| Efficiency of the Detector | 68 |
| Investigation of edge pixel collimator holes | 69 |
| Collimator Alignment..... | 71 |
| Image Formation | 76 |
| VI. Conclusions and Recommendations..... | 87 |
| Chapter Overview..... | 87 |
| Detector Performance..... | 88 |
| Input Logic Module Performance | 89 |
| Digital Gamma Finder Module Performance | 90 |
| Collimator Performance | 90 |
| Imaging Performance | 91 |
| Recommendations for Future Work | 91 |
| Summary..... | 92 |
| Appendix A. Collimator Design Code..... | 94 |
| Appendix B. Image Processing Code | 104 |
| Appendix C. Resolution Measurement Spectra..... | 113 |
| Bibliography | 117 |
| Vita | 119 |

List of Figures

| Figure | Page |
|---|------|
| 1. Converging collimator imaging system | 4 |
| 2. Detector pixel array..... | 4 |
| 3. Collimator fields of view on the detector faces | 5 |
| 4. Planar HPGe detector configuration [6] | 13 |
| 5. Trapezoidal filter applied to a pre-amplifier pulse [17]..... | 15 |
| 6. Electrode strip configuration of a strip detector [8]..... | 16 |
| 7. Center and edge pixel positions | 17 |
| 8. Position localization for a center pixel..... | 18 |
| 9. Position localization for an edge pixel | 19 |
| 10. Pu-239 gamma spectrum from an HPGe detector [4]..... | 23 |
| 11. Fetter Model of a hypothetical implosion weapon | 24 |
| 12. HPGeDSSD imaging system schematic | 25 |
| 13. Photo of HPGeDSSD imaging system electronics | 26 |
| 14. Detector, dewar and collimator stage..... | 27 |
| 15. ORTEC germanium strip detector dimensions | 28 |
| 16. Clock and strip distribution..... | 29 |
| 17. Imaging configuration using converging hole collimator..... | 33 |
| 18. Activated Sn strip spectrum | 37 |
| 19. Proposed collimator hole pattern | 41 |
| 20. Proposed hole pattern fields of view on detector center plane | 41 |

| | |
|--|----|
| 21. Edge pixel test collimator | 42 |
| 22. Optimized collimator hole pattern | 43 |
| 23. Collimator fields of view on the detector and source | 44 |
| 24. Collimator mold assembly | 45 |
| 25. Fully assembled collimator mold..... | 46 |
| 26. Experiment test setup..... | 48 |
| 27. DGF-4C module backplane connection..... | 49 |
| 28. Center pixel alignment configuration | 55 |
| 29. Pre-amplifier noise comparison between two strips | 59 |
| 30. Two strip event charge collection | 60 |
| 31. Three strip event charge collection | 61 |
| 32. Energy calibration of the HPGeDSSD..... | 64 |
| 33. Plot of FWHM vs. energy filter rise time | 65 |
| 34. Strip R4 activated Sn spectrum used for resolution measurement | 66 |
| 35. Plot of FWHM vs. energy for individual charge collection strips..... | 67 |
| 36. Detector efficiency measurements..... | 68 |
| 37. Edge effect spectra..... | 70 |
| 38. Rear strip spectra for center pixel alignment | 72 |
| 39. Front strip spectra for center pixel alignment | 72 |
| 40. Rear strip spectra for top right pixel alignment | 73 |
| 41. Front strip spectra for top right pixel alignment | 74 |
| 42. Rear strip spectra for bottom left pixel alignment | 75 |

| | |
|--|----|
| 43. Front strip spectra for bottom left pixel alignment | 75 |
| 44. Cs-137 point source image results using only two strip events | 77 |
| 45. Cs-137 point source image results using two and three strip events | 78 |
| 46. Image results of distributed Sn source using two energy windows | 80 |
| 47. Image results of distributed Sn source using a 389-395 keV energy window | 80 |
| 48. Image results of distributed Sn source using a 424-430 keV energy window | 81 |
| 49. Two source image of Eu-152 and Cs-137 point sources | 82 |
| 50. Two source image using 341-347 keV (Eu-152) energy window | 83 |
| 51. Two source image using 660-665 keV (Cs-137) energy window | 84 |
| 52. Image of pit simulation source 71 cm from detector | 85 |
| 53. Image of Eu-152 source 71 cm from detector | 86 |
| 54. Combination of four images to spell DTRA..... | 87 |
| 55. Source positioning for activated Sn strips to produce the DTRA “T” | 87 |

List of Tables

| Table | Page |
|---|------|
| 1. Activated Sn strip gamma emissions | 36 |
| 2. Radiation source used | 38 |
| 3. DGF-4C module jumper settings | 48 |
| 4. Detector output to DGF-4C module connections | 50 |
| 5. Common XIA software settings..... | 53 |
| 6. Pre-amplifier decay constants | 62 |
| 7. Gain settings..... | 63 |
| 8. Detector efficiency measurements | 68 |
| 9. Cs-137 point source image matrix using only two strip events | 77 |
| 10. Cs-137 point source image matrix using two and three strip events | 78 |
| 11. Detector FWHM measurements | 89 |

IMPROVED MULTINUCLIDE IMAGING OF SPECIAL NUCLEAR MATERIAL USING A HIGH PURITY GERMANIUM ORTHOGONAL STRIP DETECTOR

I. Introduction

Motivation

The Defense Threat Reduction Agency (DTRA), as part of fulfilling their mission of safeguarding American interests from weapons of mass destruction, has been tasked to develop quality tools and services for detecting and monitoring special nuclear material (SNM). On site inspections of countries that are signatories of various arms control treaties are a major part of DTRA's SNM monitoring mission. Some examples are the inspections and monitoring operations at facilities in Russia, Ukraine, Kazakhstan and Belarus in support of the Strategic Arms Reduction Treaty (START).

The purpose of these inspections is to verify and determine the presence and quality of SNM. Very often the SNM is contained within nuclear weapons which the countries are permitted to possess in accordance with arms control treaties. In these cases, a major role of the inspections is to ensure that the actual weapon SNM has not been removed and replaced with a spoof material designed to mimic the actual weapon pit. For this work, the SNM is assumed to be weapons grade plutonium. Proper verification of the SNM size, shape and isotopic composition can help determine the presence of a possible spoof weapon.

The weapon storage configuration for inspection is assumed to involve the weapon remaining in a storage cask. The radius of the cask is assumed to be 71 cm [15]. Due to treaty limitations, only passive inspection techniques are allowed. This limits the

radiation available for measurement to that emitted by the weapon pit with enough energy to penetrate the cask. Owing to attenuation, only gamma radiation above 200 keV is energetic enough to have a measurable flux that can be detected on the outside of the cask [14]. The information required to verify the possibility of a spoof weapon includes the gamma spectrum of the weapons grade plutonium (WGPu) along with the basic size and shape of the pit. Detectors currently used for on site inspections are not capable of distinguishing whether a weapon contains SNM in the form of a point source or a distributed source. They also cannot distinguish WGPu from plutonium having less fissile Pu-239 content.

Background

Previous research at the Air Force Institute of Technology demonstrated the capability of differentiating WGPu from reactor grade plutonium using the same HPGeDSSD used for this work [14]. In addition, the use of a collimator made it possible to distinguish a point source from a distributed source located at the collimator front face. The previous collimator utilized a set of parallel holes. This limited the size of the source to that of the detector crystal, 25 mm by 25 mm. Further analysis of the previous design also showed that the field of view for each collimator hole on the detector was larger than a single pixel. This led to an inaccurate spatial resolution of the source. Using a converging collimator, one should be able to determine the basic shape and size of a larger source. Proper spatial resolution can be maintained by ensuring that each collimator hole field of view covers only a single pixel.

The detector is smaller than conventional HPGe detectors, which results in lower detection efficiencies for higher gamma energies. However, as a significant trade-off, the orthogonal strip array provides the position sensitivity required to image SNM contained within a weapon pit. The physical dimensions of a weapon pit are discussed in Chapter 2.

Strip Detector Imaging: Position sensitivity is a crucial requirement for the development of a detector system capable of producing an image. The HPGe double sided strip detector design provides the position sensitivity required for imaging without sacrificing the energy resolution required for differentiating WGPu. The previous work conducted with this detector proved that a collimated system can produce the data required to develop a source image. The previous source size limitation can be overcome by mating the strip detector to a converging hole collimator. A collimator is used to reduce incident photons to a known range of incident angles. While the absolute efficiency of the detector is greatly reduced by the reduction of incident photons on the detector, it provides the ability to image a source larger than the detector strip array. Figure 1 shows the coupling of a detector with a converging collimator to create an imaging system.

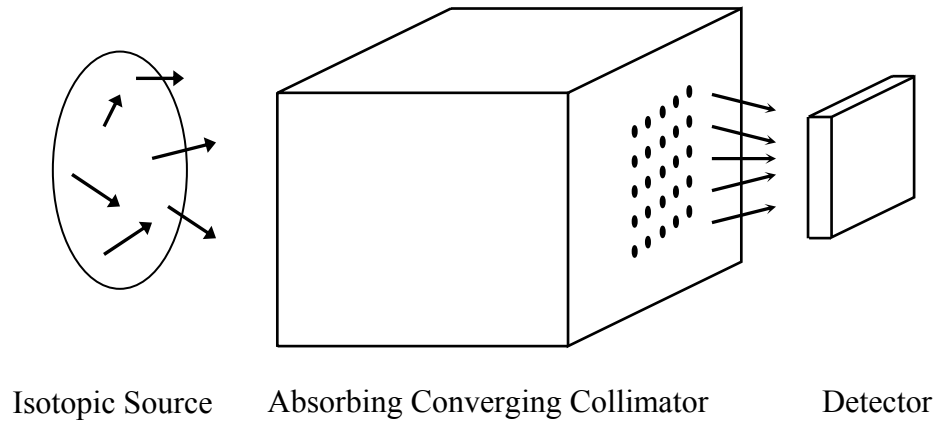


Figure 1: Converging collimator imaging system

Imaging Device: The device used for imaging employs an HPGe orthogonal strip detector with 25 pixels in a five by five array, as shown in Figure 2. Each pixel measures 5mm by 5mm. Due to hardware limitations, only a four by four array is utilized for imaging during this work. However, the collimator is designed for use with the entire five by five array to allow the flexibility of choosing which four by four combination is used.

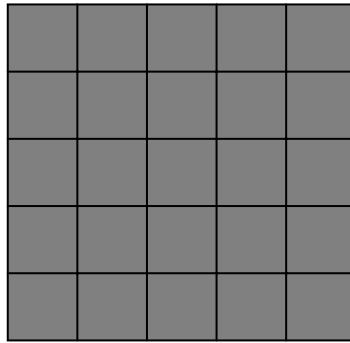


Figure 2: Detector pixel array

In order to produce an image with proper spatial orientation, a collimator is required to ensure that the counted photons originated from a particular source volume. The imaging collimator for this work is 60 mm by 60 mm by 190 mm and is made of CerroBEND, a lead bismuth alloy. It has a 5 by 5 array of 25 square holes, each 2.9 mm wide. Although the holes have a constant dimension along their entire length, they are arranged in a converging pattern to allow imaging of a source larger than the detector crystal. Proper alignment of the collimator with the detector and source ensures that each collimator hole produces a source view in only one detector pixel, thus providing proper spatial resolution of the source. Figure 3 shows the collimator fields of view superimposed on the detector crystal as calculated using the collimator design code presented in Appendix A. The black holes represent the configuration on the rear of the crystal. The grey holes represent the configuration on the front of the crystal.

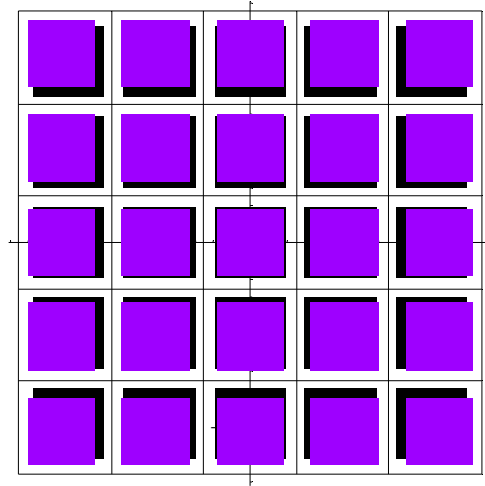


Figure 3: Collimator fields of view on the detector faces

Data Acquisition: The output signals from the HPGeDSSD preamplifiers are fed to a series of Digital Gamma Finder (DGF) modules. The modules process the digital

pulses and produce an output file consisting of module identification, the charge collection strip hit patterns, timestamps and channel numbers for each event acquired. In the previous work using the HPGeDSSD system, it was not possible to stop and start all of the DGFs at the same time. This made the assignment of events coincident on opposite faces of the detector difficult. The difficulty was in the inability to obtain proper timing information because once a module filled its first level of memory, referred to as a spill, it would download its data to the output file. Meanwhile, the other modules would continue acquiring data until their first level memory was full, at which time they would download their data and begin a new spill. Since the timestamp recorded for an event is counted from the time the current spill began, after the first spill of information was downloaded each module would be recording different times for events which were actually coincident in time. Therefore, the inability to start and stop all modules at the same time degraded the efficiency of the system. This problem should be overcome by the addition of an input logic module that will maintain consistent timing information between all modules. This should result in the ability to start and stop all module data acquisitions at the same time.

Objective

The focus of this thesis is to develop an improved imaging system using an HPGe double-sided strip detector (HPGeDSSD). The first improvement is the design and construction of a converging hole collimator which maintains proper spatial resolution of the source without sacrificing the efficiency of the system. This includes being able to image a source similar in size, shape and configuration to that encountered during on site

weapon inspections. The convergence angles of the collimator holes allow imaging of a source consistent in size and shape with that encountered during on site inspections.

Using a technique similar to a simple Anger camera [1], the 25 detector pixels are capable of producing an image showing the basic shape and size of a distributed source. This provides the ability to differentiate a distributed source from a point source.

An additional system improvement includes a more efficient image processing code. The previous imaging code required approximately five hours of data processing to produce a single image. Shortening this to a few minutes would make the system useful for on site weapons inspections. The previous code was also limited to imaging across only a single energy window. A code which can produce images using multiple energy windows would provide greater flexibility for data acquisition and analysis.

The final system improvement involves the addition of an input logic module which should force all DGF modules to start and stop at the same time. This should result in proper relative timing of all acquired pulses and thus allow proper assignment of coincident pulses.

The photon energies used for imaging must be high enough to escape a weapon cask with a measurable flux. Since the efficiency of a germanium detector decreases with increasing photon energy, the energy of the imaging photons must be in a range which balances acquisition with detector efficiency. The imaging of SNM in a weapon pit can be done by observing the gamma radiation from the dominate isotope, Pu-239, which has prominent peaks at 413.71 keV and 375.05 keV. Both of these peaks should be high enough in energy to escape from the system and still be low enough in energy to be efficiently detected and imaged. The 413 keV peak has a yield of 0.00147% and the

375 keV peak has a yield of 0.00155 %. In an operational system one or both of these peaks are proposed to be used for imaging the pit. For much of this work, the SNM will be simulated using a neutron activated Sn source. The activated Sn has a prominent peak at 391.73 keV and 427.89 keV.

Scope

This thesis work began with initial analysis of the collimator design using the Mathematica code in Appendix A. Collimator Design Code Using the results of the design code, several collimators were made to determine detector response to varying hole sizes. This also led to a test to determine the feasibility of using holes located at the edge of the detector pixels in order to increase the spatial resolution of the system. These tests were also used to characterize the response of gamma radiation incident at several locations throughout a pixel, as well as determine the settings to ensure that each strip had the proper energy calibration. The results of the collimator tests led to the design of a 25 hole converging collimator. It was then shown that mating the HPGeDSSD to the converging hole collimator produces the ability to image both point and distributed gamma ray sources. The raw data was processed using the MATLAB code shown in Appendix B. Image Processing Code, resulting in a four by four pixel image of the source, a surface plot of the acquired image and a histogram showing the number of counts acquired at energies within user specified energy windows. The user can choose to use one or two energy windows.

Assumptions

In order to best simulate an operational environment, several assumptions have to be made. The first is an assumption that the SNM to be imaged is symmetrical, since the image is only two dimensional. However, while this assumption must be made during inspections, this project uses a source which is not always symmetrical for demonstrating the ability of the HPGeDSSD to image. The second assumption is that the maximum amount of time allowed to image weapon pits during inspections will be 30 minutes, however this work does not impose restrictions on the counting times. The third assumption is that the SNM located within the pit is plutonium. Finally it is assumed that during the inspection process, the SNM cannot be removed from the 71 cm radius steel cask, which requires that only passive inspections be utilized.

General Approach

Calibration of each detector strip to the same energy scale is necessary to produce an image of a specific isotope contained within a radioactive source. Proper alignment of the converging collimator must then be verified in order to produce the desired image. Proper settings for the data acquisition components help to produce raw data which is processed through a MATLAB code to produce an image.

Sequence of Presentation

Chapter 2 gives the reader an introduction to the physics of germanium detectors, the pulse processing required, an introduction to strip detectors, and finally how the strip

detector is used to create an image. Chapter 3 describes the detector, processing electronics, controlling software, collimator, image processing code, and radiation sources used during the experiment. Chapter 4 details the experimental and computational procedures employed during the project. Chapter 5 presents the results obtained during the project, and Chapter 6 finishes with conclusions and recommendations for further work.

II. Theory

Chapter Overview

This chapter introduces the principles of germanium detectors, pulse processing, and strip detectors. These principles are the foundation for the experimental setup and analysis, which are discussed in Chapters 4 and 6 respectively.

Germanium Detectors [6]

Germanium detectors, like all semiconductor detectors, operate by the collection of electron-hole pair charges produced by ionizing radiation in the detector material. Of the various ways gamma rays can produce electron-holes pairs in the germanium crystal, only two interaction mechanisms have any significance for this work: photoelectric absorption and Compton scattering. Both processes result in the production of electron-hole pairs within the germanium. Under the influence of an applied electric field, the negatively-charged electrons will drift through the crystal following the lines of force produced by the electric field. The hole, representing a net positive charge, will also tend to move in the electric field, but in a direction opposite that of the electron. The direction of motion for each is approximately perpendicular to the detector electrical contacts. The motion of both of these charges contributes to the observed conductivity of the germanium, resulting in a charge pulse being collected on the detector electrical contacts. The amplitude of the resulting charge pulse is proportional to the amount of energy deposited by the gamma photon.

The number of electron-hole pairs produced by a gamma photon is a function of the stopping power (dE/dX), and the energy required to produce an electron-hole pair. The number of electron-hole pairs that contribute to the output signal is determined by the charge collection efficiency, which is dependent on the carrier mobility, lifetime of the carriers, and the collection time. The collection time decreases with an increasing field gradient within the detector volume.

Efficient charge collection is achieved by ensuring the applied bias voltage produces full charge carrier depletion from the entire active volume of the detector. Achieving full depletion reduces the detector capacitance and maximizes the signal-to-noise ratio, making it a preferred configuration in most applications. The depletion depth becomes very important for application at gamma ray energies from 200 to 700 keV. The greater the depletion region, the better the detector will be at stopping higher energy gammas. The thickness of the depletion region d for a planar detector configuration is given by [6]

$$d = \left(\frac{2\varepsilon V}{eN} \right)^{\frac{1}{2}} \quad (1)$$

where:

V is the reverse bias voltage,
 N is the net impurity concentration in the bulk semiconductor material,
 e is the electronic charge, and
 ε is the dielectric constant ($16 \varepsilon_0$ for germanium).

Therefore at a fixed bias voltage, the only way to increase the depletion depth is to lower the impurity concentration. For the detector used in this research, this was achieved by using high purity germanium, where the impurity concentrations are approximately 10^{10} atoms/cm³. This allows for a depletion region of about 13mm at 1000V, thus fully depleting the 9 mm thick crystal used for this work.

Figure 4 shows the configuration of a planar HPGe detector fabricated out of p-type germanium [6].

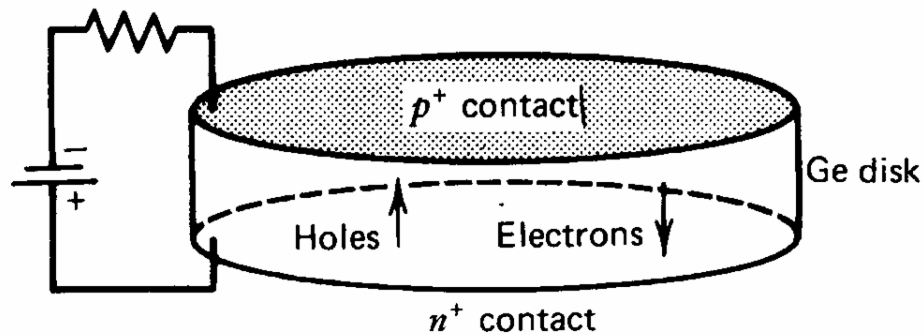


Figure 4: Planar HPGe detector configuration [6]

Planar HPGe detectors have electrical contacts on two flat surfaces. The n⁺ contact is formed by lithium evaporation, and the p⁺ contact is formed by ion implantation of boron atoms. When the junction is reverse biased a depleted region develops. Typically, HPGe detectors are operated as fully depleted detectors. Reverse biasing of the detector required that a positive voltage be applied to the n⁺ contact of the detector and the p⁺ contact be maintained at a relative ground. When planar germanium detectors are fully depleted and are operated with a large over voltage, the electric field can be assumed to be uniform from one contact to the other. This allows the electrons and holes to be

treated as drifting under the influence of a constant electric field through the entire volume of the detector.

The most important parameters for any gamma spectrometer are the efficiency and energy resolution. The efficiency determines the number of counts that can be collected over a given time, while the energy resolution is a measure of the ability to distinguish gamma-rays with similar energies. For germanium detectors the resolution is expressed as the full width at half maximum (FWHM) for a particular full energy peak.

Pulse shaping/processing [17]

Collection of the electron-hole pairs produces a charge pulse. Each charge pulse is processed by a preamplifier which is built into the detector cryostat housing. The magnitude of the voltage pulses sent from the preamplifier to the pulse processing electronics, is dependent on the amount of charge collected and therefore dependent on the energy that was deposited and collected.

When the pulse is sent from the preamplifier to the pulse processing electronics, the pulse's waveform is digitized in an analog to digital converter (ADC). Next the signal is passed to a real time processing unit (RTPU) where a digital filter is applied to shape and amplify the pulse. The filter used is a trapezoidal filter; this filter typically has a flat top, which covers the rise time of the pulse that makes the pulse height measurement less sensitive to the variations of the signal shape. An example of a trapezoidal filter applied to an ADC output pulse is shown in Figure 5.

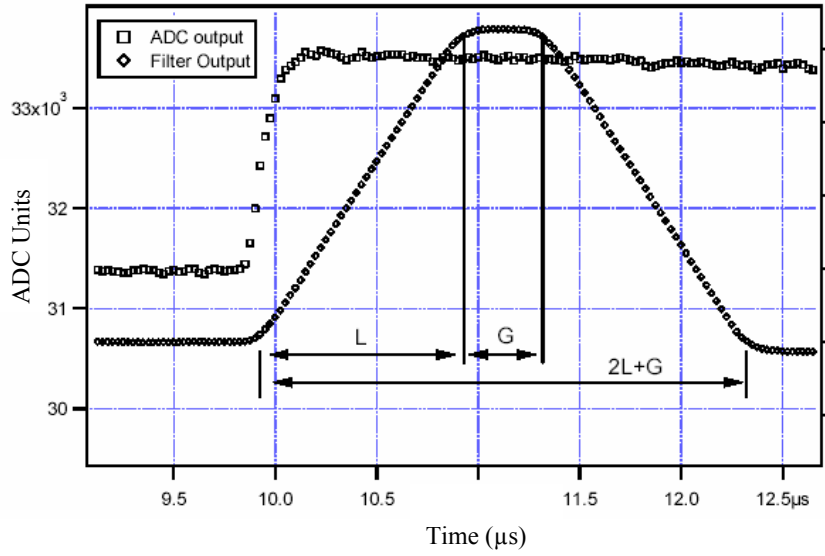


Figure 5: Trapezoidal filter applied to a pre-amplifier pulse [17]

The rise time L , and the flat top G of the filter can be controlled by the user through the XIA controlling software to maximize the energy resolution.

Strip Detectors

A germanium orthogonal strip detector combines the energy resolution of a high purity germanium detector with the ability to produce an image. Historically the high energy resolution and imaging capabilities of the germanium strip detectors have been exploited through astrophysics applications [8]. Germanium strip detectors are similar to planar HPGe detectors, except that single contacts to collect the charges on each side are replaced with discrete strips of contacts which are orthogonal to each other. Figure 6

shows the configuration of the charge collection strips for a five by five strip detector, like that used for this work.

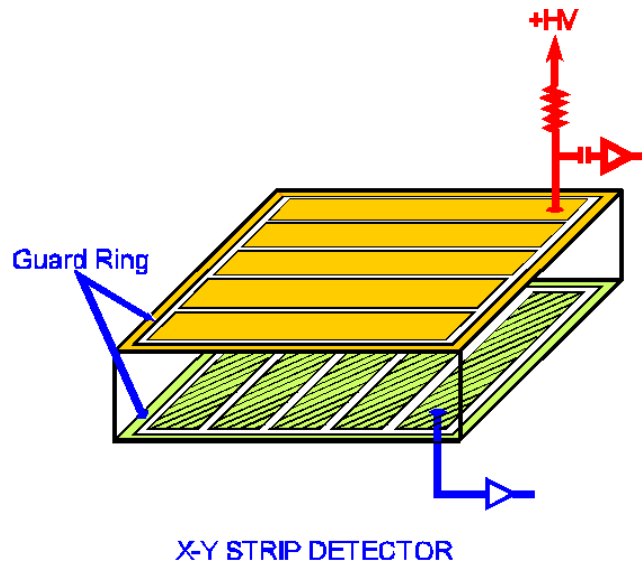


Figure 6: Electrode strip configuration of a strip detector [8]

With a standard HPGe planar detector the charge is typically read out from one of the two contacts, usually the n+ contact which collects the electrons. However, with a germanium strip detector all of the contacts are read out to individual preamplifiers. Since each interaction within the germanium must produce a hole and an electron, at least one of the strips on each side must collect the charges. This ability to collect electrons and holes on opposite sides of the germanium is what provides the means for producing an image.

Imaging Using a Strip Detector

The intersections of the orthogonal electrode strips which collect the electrons and holes produce a five by five array of pixels. The ability to distinguish which strips collect the charge from a particular ionizing interaction provides a way to obtain two-dimensional position localization of the interaction.

Following the recommendation from previous imaging work performed using this system, I proposed using two categories of image pixels. First are the “center pixels” which correspond to collimator holes centered on one of the 25 detector pixels formed by the intersection of a front and back strip. Second are the “edge pixels” which correspond to collimator holes centered on the intersection of two strips on one face and centered on a strip on the opposite face. Figure 7 shows the relative locations of the two categories of pixels superimposed onto the 25 detector pixels. In theory, the use of edge pixels would increase the spatial resolution of the system by narrowing the origin of the gamma ray down to a smaller area.

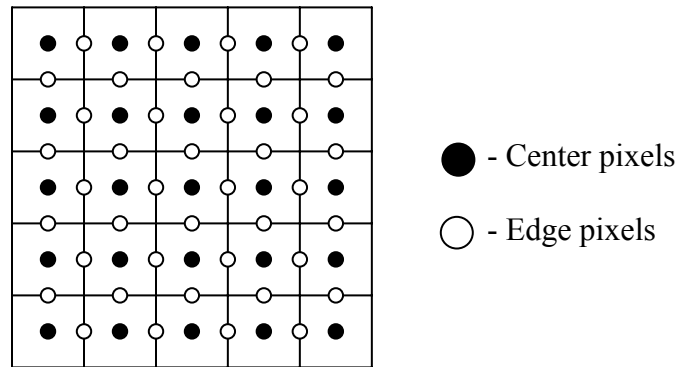


Figure 7: Center and edge pixel positions

In order for an event on a center pixel to be used in the formation of the image, a front strip and a back strip must both record an event that occurred at the same energy and at the same time. To be considered the same energy two pulses must be within one FWHM of a full energy event peak. To be considered the same time, the two pulses must fall within some coincidence window of time. For this project the time coincidence window was set to 100 ns. This was optimized experimentally.

Therefore, if a front strip and a back strip have a coincident event in energy and time, the location of the interaction can be inferred as the place where the two strips intersect. This is referred to as a two strip event. These events are the result of a gamma depositing energy in only one pixel of the detector. For example, if a charge collection strip on the front, F2, and a charge collection strip on the back, R3, both record events coincident in time and energy, then the intersection of the two strips is the location of the event, as shown in Figure 8.

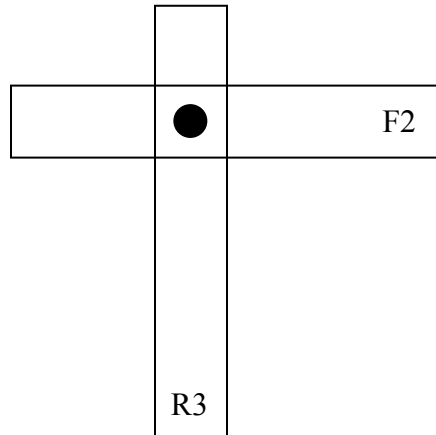


Figure 8: Position localization for a center pixel

In order for a three strip event on an edge pixel to be used in the formation of the image, one strip on either the front or back must record a full energy peak for the energy being sought. In addition, the energy peaks on two adjacent strips on the opposite side of the detector must sum up to an energy that is within one FWHM of the full energy event peak of the original strip. All three peaks must fall within the time coincidence window, just as with the center pixel two strip events. For example, suppose a charge collection strip on the back, R3, records an event. In order to count as an edge pixel event, there must be two adjacent strips on the front, say F3 and F4, whose combined event is coincident in both time and energy with the event recorded on R3. This would result in the assignment of the event to the edge pixel shown in Figure 9.

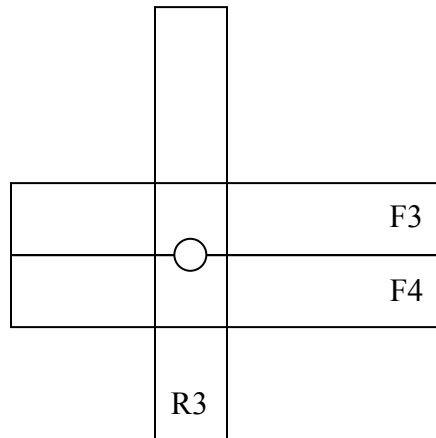


Figure 9: Position localization for an edge pixel

In order for such an event to be recorded, one of two things would have to occur. First, a gamma could undergo a photoelectric absorption very close to the gap between the adjacent strips. If close enough to the gap, some charge would be collected by one strip and the rest by the adjacent strip. The second scenario involves single or multiple

Compton scatters which send the reduced energy gamma into the adjacent pixel where it would undergo either a photoelectric absorption or more Compton scatters followed by photoelectric absorption. In both scenarios the adjacent strips would show a charge sharing of the full energy event recorded on the opposite side of the crystal.

As discussed in later chapters, the use of collimator holes producing edge pixels proved to be impracticable for gamma imaging. However, if an event shares charge between two adjacent strips and one opposite face strip, as discussed for the edge pixels, it can still be used for imaging if proper timing information is acquired. If the charge collection on adjacent strips occurs within the time resolution of the system, namely 25 ns, the interactions appear to occur simultaneously in two pixels and therefore cannot be used. However, if the timestamps for the two adjacent strip charge collections is separated by more than 25 ns the interaction timestamps will be separated by at least one time unit. This separation in time allows the event to be assigned to the pixel which recorded the interaction first. This assignment of three strip events to a single pixel is based on the assumption that the gamma interaction resulted in Compton scattering of the gamma into the adjacent pixel. The time required for the gamma to scatter into the adjacent pixel, interact, and produce a signal produces the time difference between the interactions recorded in the two pixels. This assumption requires that the incident gamma be well collimated to ensure that the first Compton scatter interaction occurs in the pixel where the gamma first entered the detector.

If the source irradiating the detector is well collimated, and the location of the interaction within the detector is known, the location from which the photon emanated

can also be known. The uncertainty in the photon's location of origin is limited by the size of the collimator field of view on the source.

Image Analysis [13]

The image analysis for this project involved images consisting of a four by four array of grayscale pixels. Each pixel corresponds to one pixel formed by two of the orthogonal detector charge collection strips. Each event recorded by the detector is analyzed to see if it meets the specified requirements to be counted as an image event. If the image requirements are met, then the event is assigned to its appropriate pixel location. When all events have been processed, the resulting four by four matrix is used to construct the grayscale image. The range of values for each pixel will be from zero to the number of events recorded for that particular pixel, which may be as high as several thousand depending upon the source. The maximum pixel value in the image is then assigned a value representing pure white (255). A count of zero corresponds to black (0), all other pixels are then assigned a grayscale value based upon their value relative to the maximum value in the image.

The possibility of having values ranging up to several thousand counts complicates the imaging process because there are only 256 distinguishable brightness values for 8-bit grayscale imaging. These values correspond to an 8-bit number ranging from 0 to 255, 0 being black and 255 being white. Therefore, if the image contains values above 255 then all pixel values must be scaled to fit within the 0 to 255 range.

The pixel value scaling is further complicated by the fact that only about 20-30 gray levels can be visually distinguished by the human eye. However, a good quality printing system can produce more than 30 gray levels. This can lead to difficulty in properly distinguishing between different pixel values in an image. Providing a grayscale legend for an image can greatly aid in distinguishing the true relative brightness between pixels. However, the best grayscale image analysis is performed by referring to the actual pixel values rather than the resulting grayscale image. This type of analysis would be quite difficult for an image containing several thousand pixels but it works quite well for the 16 pixel images produced for this work.

Weapon Assumptions

The material and physical dimensions of a nuclear weapon are key components that will affect the ability of the HPGeDSSD to produce an image of the SNM. The SNM considered for this project is assumed to be Pu-239. The high energy portion of a Pu-239 spectrum collected with a germanium detector by the Idaho National Engineering & Environmental Laboratory is shown in Figure 10. The peaks of interest for this project are the 375 keV (not shown) and 413 keV peaks. These peaks are simulated using the 391 keV and 427 keV peaks from a neutron-activated tin source. Further discussion of the neutron-activated tin spectrum can be found in Chapter 3.

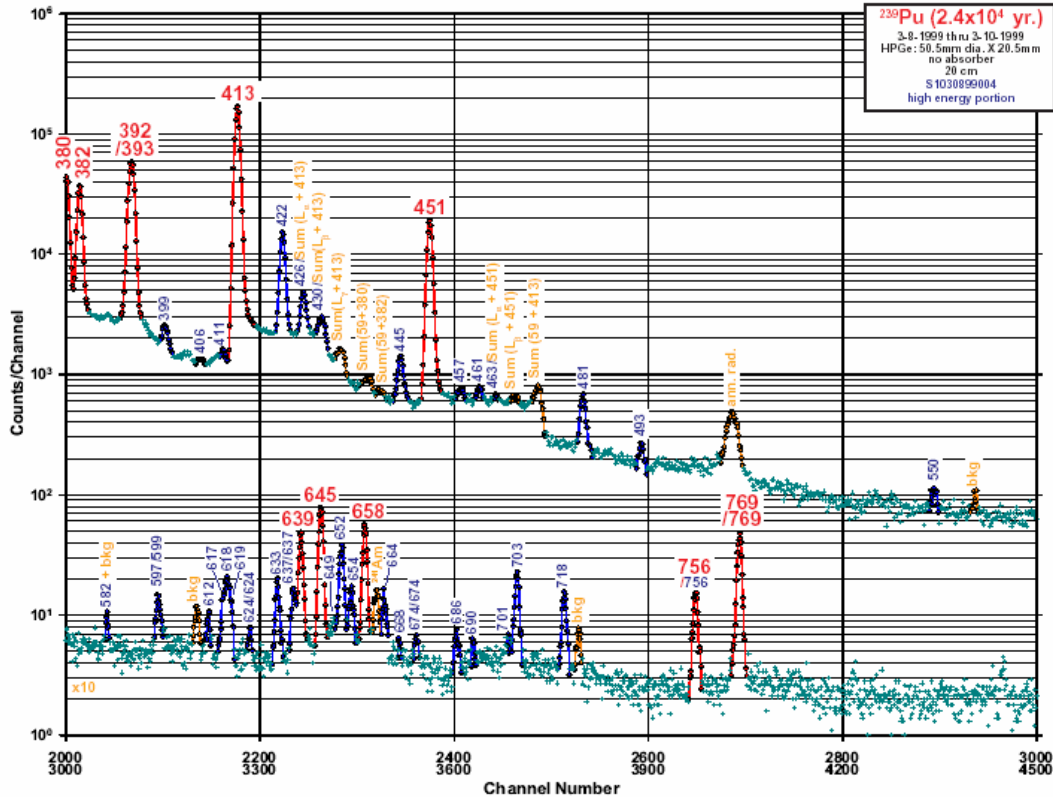


Figure 10: Pu-239 gamma spectrum from an HPGe detector [4]

The time required to produce an image depends primarily on the radiation flux at the detector that are to be imaged. In an imaging application of nuclear weapons, the flux is low because of the attenuating materials surrounding the SNM, as well as the low activity of plutonium due to its long half life. An understanding of the physical dimensions of the pit and the shielding around a weapon can be obtained by studying a model published by Steve Fetter in “Detecting Nuclear Materials” [3]. In this publication, Fetter presents what he refers to as the general characteristics of an implosion-type fission weapon. Figure 11 is a description of a hypothetical weapon presented in reference [3].

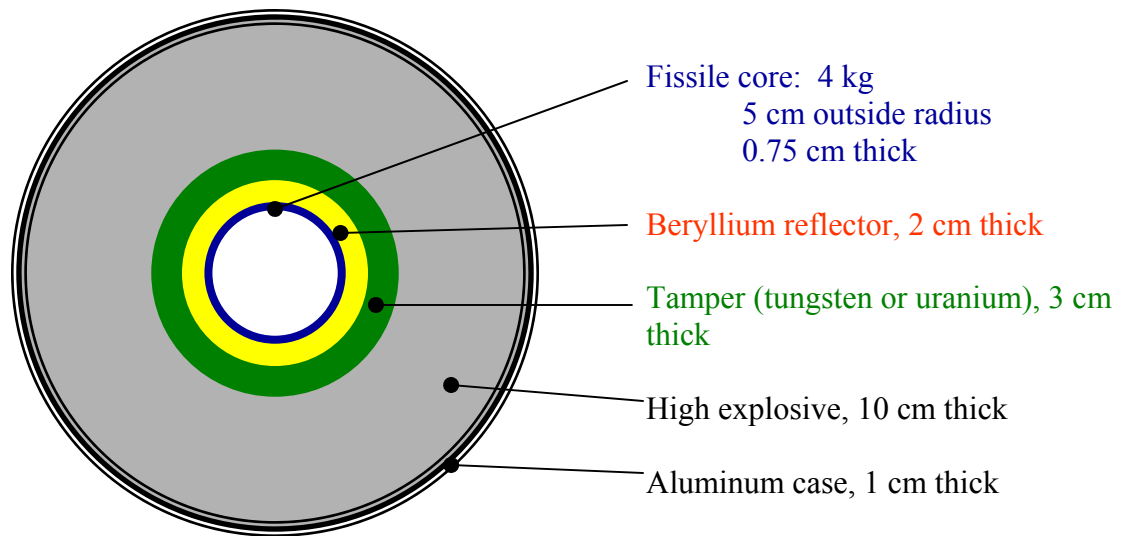


Figure 11: Fetter Model of a hypothetical implosion weapon

III. Equipment

Chapter Overview

The components of the imaging system used for this work include the germanium strip detector, the converging hole collimator, two digital gamma finder (DGF) data acquisition cards, the input logic unit, the power distribution module (PDM), the CAMAC crate, the crate controller, the software to control the DGFs, and the software to produce the image. A schematic of the entire system is shown in Figure 12. A photo of the HPGeDSSD imaging system electronics configuration is shown in Figure 13.

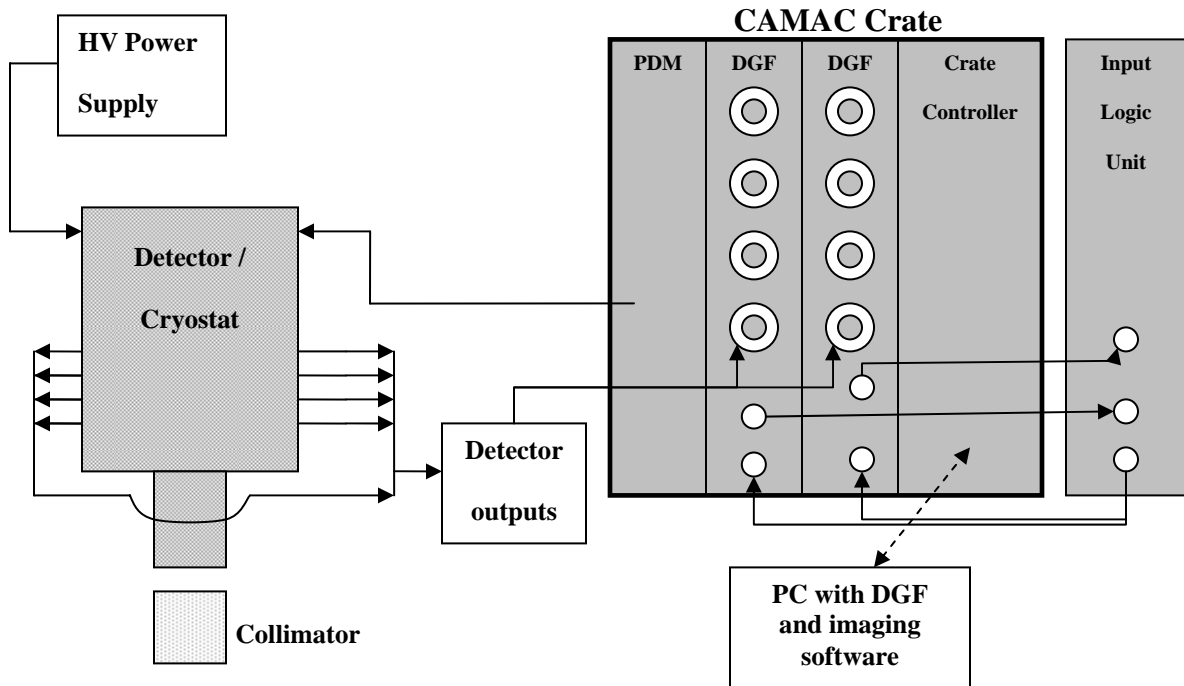


Figure 12: HPGeDSSD imaging system schematic

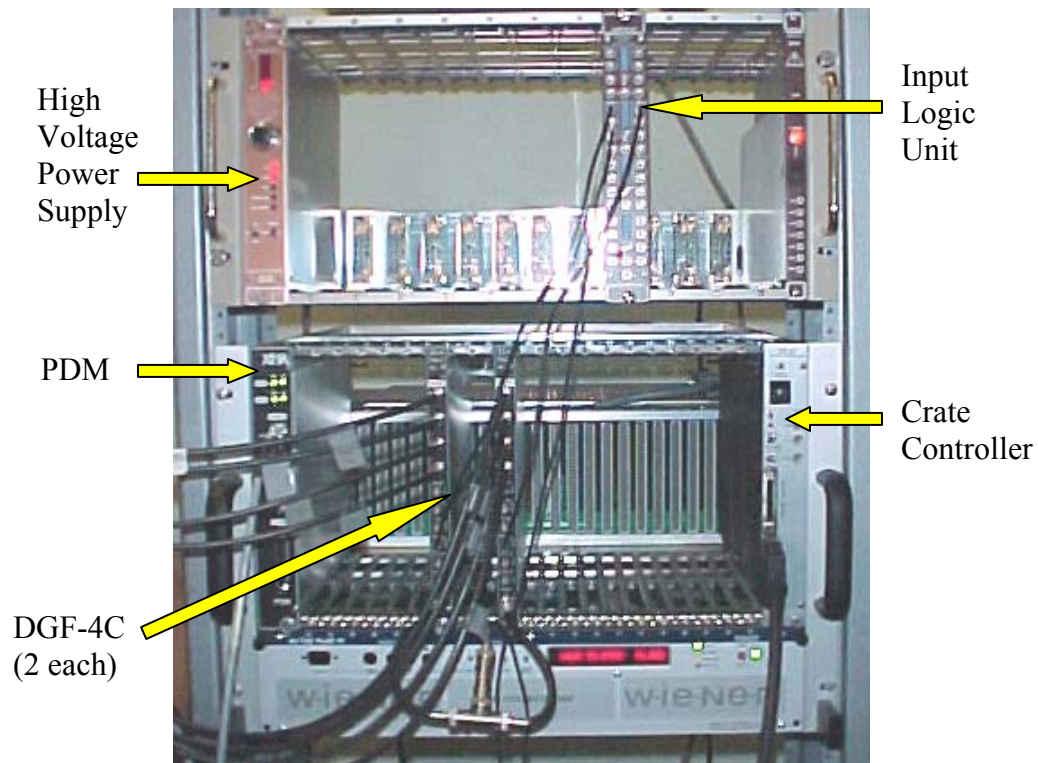


Figure 13: Photo of HPGeDSSD imaging system electronics

Detector [10][14]

The detector used for this project was an ORTEC Model HPGeDSSD, Serial number 42-WPAFB-01. The detector is an HPGeDSSD that operates at approximately 77K using liquid nitrogen. A photo of the detector, dewar and collimator stage is shown in Figure 14.

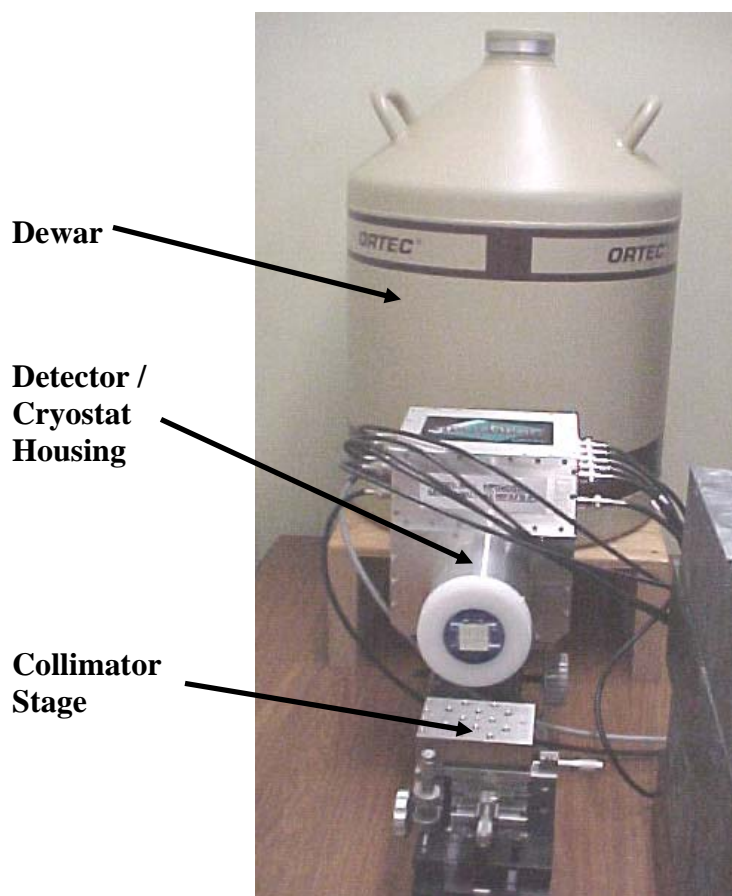


Figure 14: Detector, dewar and collimator stage

The detector has five charge collecting strips on each 25 mm by 25 mm side. It was designed and specified by Mr. Matt Lange, a previous AFIT student. The strips on opposing sides are orthogonal to each other, which allows for the determination of location when a gamma interaction occurs within the germanium crystal. This effectively creates 25 pixels on the detector. Each of the charge collection strips is 25 mm long and 5 mm wide, so that the total active surface area of the detector is 25 mm by 25 mm. The detector has an active depth of 9 mm. The dimensions of the detector and the charge collection strips are shown in Figure 15.

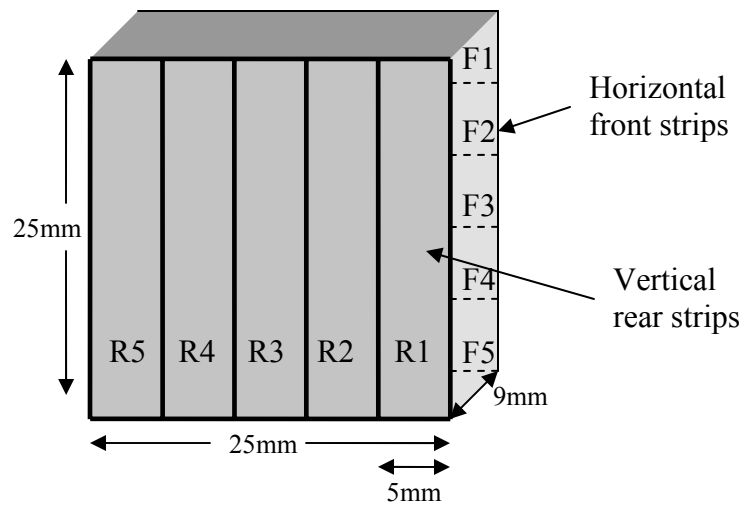


Figure 15: ORTEC germanium strip detector dimensions

The detector is secured inside a cylindrical cryostat housing which allows it to be cooled to 77K. The housing also contains a total of 10 preamplifiers, one for each charge collection strip. In order to minimize the influence of the housing on the incident gamma rays, there is a 0.5 mm thick beryllium entrance window, as well as 0.3 μm of inactive germanium along the center axis of the housing. The detector is oriented so that the 25 mm by 25 mm face is perpendicular to the long axis of the collimator center hole.

In order to optimize the collection of electron-hole pairs, the detector is operated at a +1000 V bias. The charge collecting strips on the back face of the detector are lithium and are at +1000 V bias. The strips on the front face are boron and are at about +1 V. Each of the strips is electrically separated from one another. Since there is a 1000 V potential between the front and rear strips, the two sides can be treated as parallel plates, which force any electrons or holes to the charge collection strips.

DGF Hardware [17]

For this project, two X-Ray Instrumentation Associates (XIA) DGF model 4C, Revision E-1 CAMAC modules were used. Their serial numbers were 1240 and 1244. The DGF-4C is a four channel all-digital waveform acquisition and spectrometer card. The incoming signals from the detector are digitized by analog-to-digital converters (ADC). Digital waveforms are analyzed by the digital signal processor (DSP) for pulse shape analysis. Then the waveforms, timestamps, and the pulse shape analysis results are read by the host system. The modules can process up to 200,000 counts per second for all four channels combined. The individual modules support coincidence spectroscopy and can be synchronized to the same clock. Trigger signals can be distributed between modules. The acquisition of data was simplified by assigning separate triggers to the front and back detector strips. Data corresponding to coincidence between modules is determined in the image processing code. Figure 16 shows the clock and charge collection strip distribution used for this work.

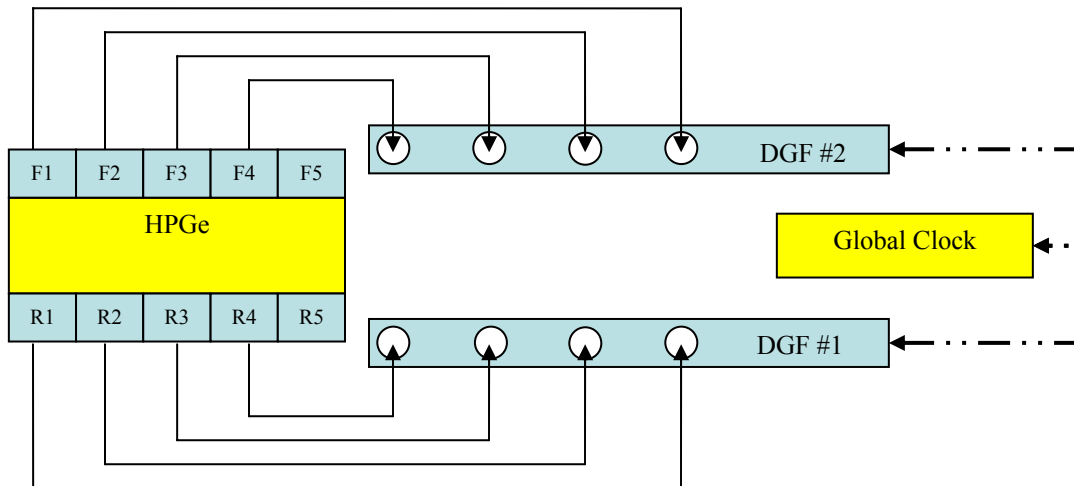


Figure 16: Clock and strip distribution

The DGF-4C modules have four building blocks: the analog signal conditioning, the real-time processing units (RTPU), the digital signal processors (DSP), and the CAMAC interface.

Analog Signal Conditioning: Each of the analog inputs has its own signal conditioning unit, which adapts the input signals to the input voltage range of the ADC. There is also a software controllable gain setting at this stage. The ADC is a waveform digitizer.

RTPU: There is one RTPU for each channel, and it consists of a field programmable- gate-array (FPGA) and a first-in first-out (FIFO) memory. When data arrive from the ADC, the RTPU applies a digital trapezoidal filter which acts as a shaping amplifier. In addition to the pulse shaping, the RTPU contains a pileup inspector. If the logic detects a second pulse too close to the one being processed, so that the pulse height measurement of the first pulse would be corrupted, both of the pulses are rejected. If the pulse is not rejected as a pile up event, a trigger is issued to notify the digital signal processor (DSP) that there is raw data ready for processing. When the trigger is issued to the DSP, the RTPU is latched until it has been serviced by the DSP.

DSP: The DSP controls the operation of the pulse processing electronics, reads the raw data from the RTPU, determines the pulse heights, time stamps each pulse, and prepares the data for output to the controlling computer.

CAMAC Interface: The CAMAC interface is the means of communication with the DGF-4C.

Input logic unit [11]

The input logic unit used is an ORTEC Quad 4-Input Logic Unit Revision D, model C04020 and serial number 382. The logic functions it can perform are: coincidence (AND), anti-coincidence (veto), fan-in (OR), fan-out, fast negative NIM-to-TTL conversion, and pulse lengthening. For this work, the fan-in (OR) function was utilized. Each of the four inputs accepts NIM fast negative logic pulses. Front-panel, three-position slide switches select the logic requirements separately for each input.

For this work, the Busy Out ports on the DGF-4Cs are each connected to an input on the logic module. The logic module output is distributed to each DGF-4C Sync In port. This setup allows both modules to start and stop acquisition at the same time. Coupling this with a global clock for both modules allows the determination of coincident events.

Power Distribution Module [16]

The PDM used for this effort is an XIA CAMAC module Revision 3 and serial number 108. The PDM provides + 12 V and + 24 V preamplifier supply voltages. It is capable of supplying power for up to 20 preamplifiers.

Crate and Crate Controller [5][16]

The CAMAC crate used in this research is a Wiener type UEC 01 VH / Typ 342, part number 0305.0102, and serial number 3698023. It is a 25-slot CAMAC crate. The

crate controller is a Jorway model 73A-2, serial number 662. It is the interface between the CAMAC crate and the host computer. The interface is via a SCSI connection.

Collimator

Proper collimation of the incoming photons is crucial for producing an image. In order to obtain true spatial discrimination, the fields of view for the collimator holes should not overlap at either the source or the detector. Several collimators were made in-house for this work. All were made from AIM-70 (CerroBEND) using an in-house mold design. AIM 70 is made of 50% bismuth, 26.7% lead, 13.3% tin, and 10% cadmium. It has a melting point of 70° C which make it ideal for building collimators in-house.

Several single hole and three hole collimators were used to characterize the detector response. A slot hole collimator 50 mm by 50 mm by 100 mm with a 1 mm slot was used to determine the detector response near the edges of the charge collection strips. The characterization of the response near the strip edges helped ensure the design of the final collimator would provide proper spatial discrimination. A parallel hole collimator developed by Nuclear Fields Inc. for previous work with the detector was used to test the image processing code before the final collimator was completed. The parallel hole collimator is made of PbSb alloy and consists of 25 round holes 3.6 mm in diameter. It is 30 mm by 30 mm by 50 mm.

The collimator used for final imaging was designed using a Mathematica code developed in house. The code and its output are presented in Appendix A. Collimator Design Code. The imaging collimator measures 60 mm by 60 mm by 190 mm. It has a 5

by 5 array of square holes, 2.9 mm wide along their entire length. The holes converge outward from the detector to permit imaging objects larger than the detector crystal. The hole configuration allows a 5 cm radius source to be imaged from a distance of 71 cm from the source side of the collimator. This configuration was chosen to simulate imaging a nuclear weapon pit while it is in a storage cask. Figure 17 shows the configuration used to properly align the converging hole collimator with the detector for imaging operations.

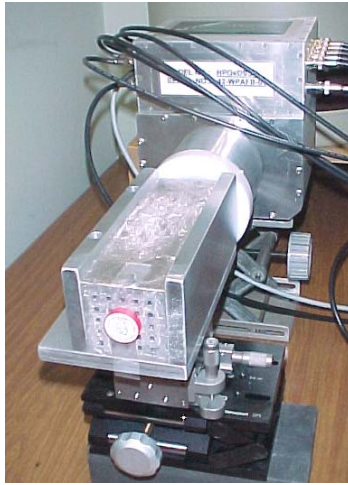


Figure 17: Imaging configuration using converging hole collimator

Image Processing Code

In order to produce an image, the raw data collected from the DGFs was processed using a processing code written in the MATLAB computer language. The code contains 9 main algorithms for processing the raw data. The 9 steps are listed below, and the full code is presented in Appendix B. Image Processing Code.

1. Read in the raw data and user inputs. The raw data is saved using the IGOR software as a text file. The user is prompted to input up to two energy windows and calibration for the image. A default calibration is also available. The user also has the option to use three strip events in addition to two strip events.

2. Sort the data. An event data set consists of the hit pattern, timestamp and channel number corresponding to the energy. Each event is sorted into one of four matrices depending on which module it is for and whether it is a single strip or two strip coincident event.

3. Each single rear strip event is then compared to each single front strip event to determine events coincident in both time and energy.

4. When coincident events are found in step 3, each event hit pattern is used to determine which strip received the event. An event hit is then assigned to the appropriate image pixel by adding one to its value.

5. Two strip events for the rear strips are compared to each single front strip event to determine three strip events coincident in both time and energy.

6. When three strip coincident events are found in step 5, each event hit pattern is used to determine which strips received the event. An event hit is then assigned to the image pixel which recorded its portion of the charge first by adding one to its value.

7. Two strip events for the front strips are compared to each single rear strip event to determine three strip events coincident in both time and energy.

8. When three strip coincident events are found in step 7, each event hit pattern is used to determine which strips received the event. An event hit is then assigned to the image pixel which recorded its portion of the charge first by adding one to its value.

9. The final image, as seen by the detector, is then shown along with a surface plot of the image and a histogram showing the number of events recorded for each energy throughout the specified energy windows.

In steps 6 and 8 above, the assignment of a three strip event to a single pixel is controlled by the timing of the pulses produced on adjacent strips. The timing resolution of the DGF modules is 25 ns. This means that pulses on adjacent strips which record the same time must have occurred within 25 ns of each other. Therefore, adjacent strip events which occur at the same recorded time cannot be used with this system. However, if the time between adjacent strip pulses is more than 25 ns then it is assumed that the gamma ray entered the detector at the strip which recorded its pulse first. This assumption is possible because the timing trigger for the pulses is based off a threshold value and not a percentage of the individual pulse.

Radiation Sources

Activated Tin Source [14]. In order to simulate Pu-239, a distributed radiation source was needed that had photons in the 375 and 413 keV ranges. The easiest source to get that satisfied the necessary requirement was neutron activated tin. The 5 Sn strips were 5 mm wide and 25 mm long and approximately 1.7 mm thick. The five Sn strips were activated at the Ohio State University research reactor on 28 August 2003. The strips had masses ranging from 1.493g to 1.512g. All five strips were placed in the OSU reactor central irradiation facility (CIF) for two and a half hours, while the reactor was run at 90% power. After the irradiation of the sources was completed, the reactor was

shut down and the sources remained in the CIF overnight to allow the extremely short lived isotopes to decay. Then the sources were removed from the CIF and were placed into a pig, where they were allowed to sit for three weeks to let the short-lived activation products decay away. After this cooling off period, only long-lived activation products remained. The long-lived activation products resulting from neutron activated Sn are given in Table 1. The activities of the strips are unknown. Because of its relatively short half-life, Sn-117m was not detected during this work. However, the relatively short lived Sb-124 was still present because there was such a large quantity present following the neutron activation. A spectrum of one neutron-activated Sn sample, as seen in the DGF controlling software, recorded by a single strip from the HPGeDSSD is shown in Figure 18. The collection time for the spectrum was 2 hours. The spectrum was collected on 3 December 2004 (463 days after activation).

Table 1: Activated Sn strip gamma emissions

| Nuclide | Gamma-ray Energy [keV] | Branching Ratios (%) | Half-life |
|---------|------------------------|----------------------|------------|
| Sn 117m | 158.91 | 86.0 | 14 days |
| Sn 113 | 255.30 | 1.8 | 115 days |
| | 391.73 | 64.97 | |
| Sb 124 | 602.7 | 98.26 | 60 days |
| Sb 125 | 176.57 | 6.82 | 2.76 years |
| | 427.89 | 30.0 | |
| | 463.34 | 10.5 | |
| | 600.56 | 17.9 | |
| | 606.34 | 5.03 | |
| | 635.88 | 11.31 | |

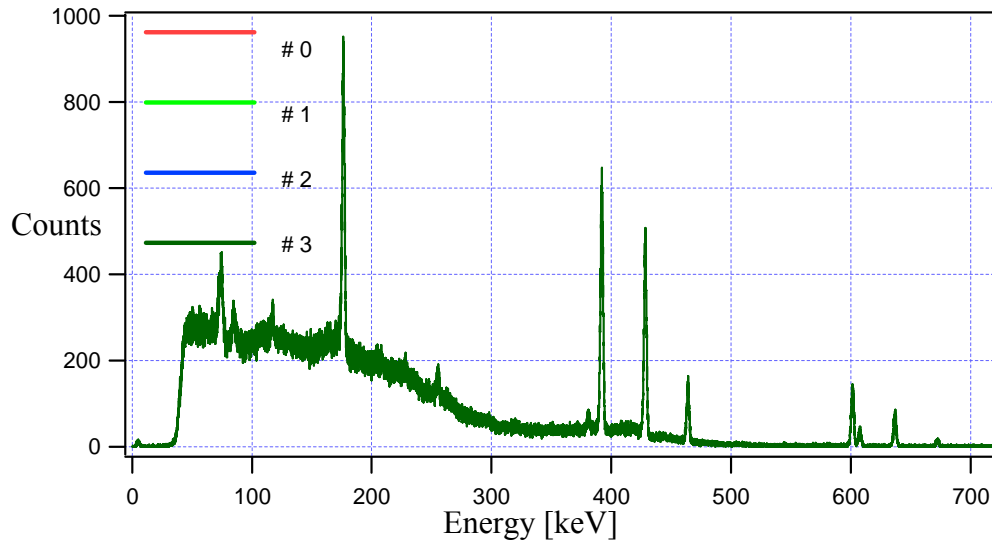


Figure 18: Activated Sn strip spectrum

Simulated Weapon Pit Source [9]: In order to test the ability of the system to image a weapon pit in a configuration similar to that encountered during on site weapon inspections, a distributed Cs-137 bowl source was used. The source was designed and specified by Mr. Mike Nelson, a previous AFIT student. The bowl was constructed from a polymer material to form a hemisphere shell. The outer and inner surfaces are 0.3 inches (7.62 mm) thick surrounding a hollow cavity constructed to be 0.3 inches (7.62 mm) across. The outer radius of the hollow cavity is 5 cm. The configuration produces a 5 cm radius hemispherical source cavity which is 7.62 mm thick. The interior cavity contains a Cs-137 source suspended in approximately 54 ml of 1M HCL. The reference activity of the source was 650 μCi on 10 January 2003.

Shortly after fabrication, the source was found to be leaking the Cs-137 solution. This led to the source being sealed in a plastic bag for safe handling and storage. I was

unable to determine the amount of source solution which had leaked out, but it appeared from the acquired images that enough was lost to affect the symmetry of the source.

Standard Sources: The following standard sources were used for determining the calibration, efficiency and resolution of the detector. The sources were also used for aligning the collimator with the detector and showing the ability to image various sources at the same time using multiple energy windows.

Table 2: Radiation source used

| Source (Reference date) | Nuclide | Gamma-ray Energy [keV] | Initial Activity (μ Ci) | Branching Ratio (%) | Half-life |
|--|---------|------------------------------|------------------------------------|------------------------|-------------|
| Multi Nuclide – T108 Isotope Products Laboratories (15 Jul 04) | Am-241 | 60 | 0.02912 | 36.0 | 432.17 |
| | Cd-109 | 88 | 0.4260 | 3.63 | 462.6 days |
| | Co-57 | 122 | 0.01529 | 85.6 | 271.79 days |
| | Ce-139 | 166 | 0.01963 | 79.9 | 137.64 days |
| | Hg-203 | 279 | 0.06120 | 81.5 | 46.595 days |
| | Sn-113 | 392 | 0.07482 | 64.9 | 115.09 days |
| | Sr-85 | 514 | 0.09425 | 98.4 | 64.849 days |
| | Cs-137 | 662 | 0.06875 | 85.1 | 30.17 years |
| | Y-88 | 898 | 0.1481 | 94.0 | 106.63 days |
| | Co-60 | 1173 | 0.08091 | 99.86 | 5.272 years |
| | Co-60 | 1333 | 0.08091 | 99.98 | 5.272 years |
| | Y-88 | 1836 | 0.1481 | 99.4 | 106.63 days |
| Na-22 – T107 Isotope Products Laboratories (15 Feb 03) | Na-22 | 511 | 0.8796 | 99.94 | 950.8 days |
| | | 1275 | 0.8796 | 99.94 | 950.8 days |
| Eu-152 – T110 Isotope Products Laboratories (15 Dec 04) | Eu-152 | 244 | 10.14 | 7.5 | 4933 days |
| | | 344 | 10.14 | 26.6 | 4933 days |
| Cs-137 – T089 Isotope Products Laboratories (1 Aug 98) | Cs-137 | 662 | 10.02 | 85.1 | 30.17 years |

Controlling Software / SCSI Interface

The controlling software used for the DGF-4C modules was the XIA DGF-4C viewer, release number 3.04. This software runs inside the IGOR Pro software which was supplied by XIA with the purchase of the DGF-4C modules. The controlling software provides the user a platform from which all settings can be adjusted for the entire pulse processing system. It also provides an environment for analyzing the resulting data. The SCSI interface card used in the PC is an Adaptec 2930 SCSI card.

IV. Procedure

Chapter Overview

In order to help optimize the imaging system, a collimator design code was developed. This allowed for design of several collimators in order to test the detector response under variable configurations. An image processing code was also developed early on. Both codes were updated throughout the experiment to meet the required needs as they were identified.

Prior to any collimator testing, the equipment was set up and the proper hardware and software settings required to create an image were determined. This included characterizing the detector by determining the noise present, the proper energy calibration and efficiency of the detector. With each strip calibrated to the same energy scale, several test collimators were used to determine the optimum size parameters of the final collimator. This work also included investigating the possibility of using holes located at the edge of each pixel. Once a feasible collimator design was developed, mold drawings were made and the mold was fabricated. The collimator was then built and put into the system for imaging.

Collimator Design and Fabrication

The Mathematica code developed for the collimator design is shown in Appendix A. The code allows the user to optimize the design by varying the size of the holes, collimator length, and focal length of the converging holes. All holes are required to be the same size for the entire length of the collimator.

Theoretically, a converging collimator using edge pixels could be used to increase the spatial resolution of the source size and shape while increasing the size of the source as compared to the previous work with this detector. One such example is the partial nine by nine array of 65 holes shown in Figure 19. Black filled circles represent the source face configuration and the white open circles represent the detector face configuration. Figure 20 shows the resulting fields of view for each collimator hole in the center of the detector crystal.

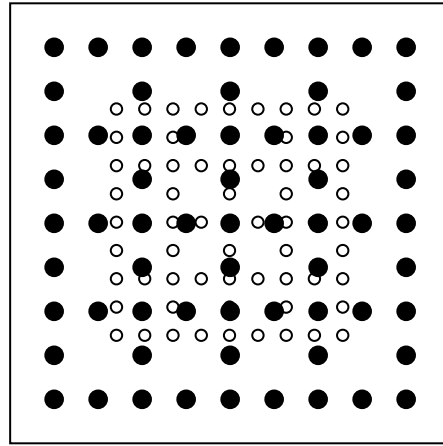


Figure 19: Proposed collimator hole pattern

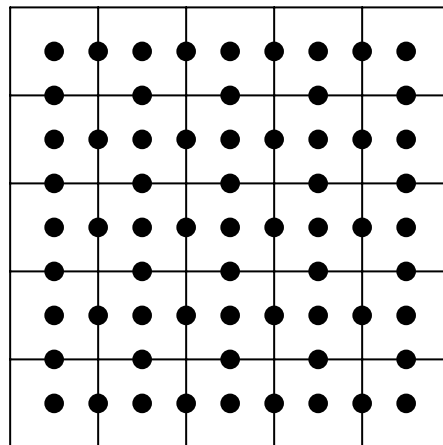


Figure 20: Proposed hole pattern fields of view on detector center plane

A test collimator, shown in Figure 21, was built to test the feasibility of using edge pixel collimator holes for gamma imaging. This was done by using a tin strip source collimated with a 1 mm wide gap along the entire 25 mm length of the strip. The response of strips F2 and F3 was investigated with the collimated source located at various locations near the edge between the strips. I expected to be able to find a range near the gap in which each strip recorded very few full energy peaks. This would then determine the size limit of an edge pixel hole. If the edge pixel records a full energy peak on a single strip then it would be assigned to the center strip pixel for that strip and therefore not provide proper spatial resolution of the source. As discussed in Chapter 5, the recorded data showed that the edge pixel holes would have to be too small to provide enough efficiency for imaging. This led me to use only center pixel holes for the final collimator design.



Figure 21: Edge pixel test collimator

The original collimator design code utilized round holes. However, analysis of the design showed that using square holes would increase the field of view areas on the source and the detector by approximately 25%. This increase in the volume of the detector utilized and the volume of the source visible to the detector results in shorter data acquisition times and a higher efficiency of the system.

The primary objective for the collimator design was to maximize the amount of the detector used while also maximizing the amount of the source seen. In addition, proper spatial resolution must be achieved by ensuring the fields of view within the detector and at the source do not overlap. Figure 22 shows the optimized collimator design hole pattern. The collimator is 190 mm long with 2.9 mm square holes and a 1.16 m focal length. The black holes represent the hole configuration on the side nearest to the detector. The gray holes represent the hole configuration on the side nearest to the source. Appendix A presents the design code and its output for the optimized collimator configuration.

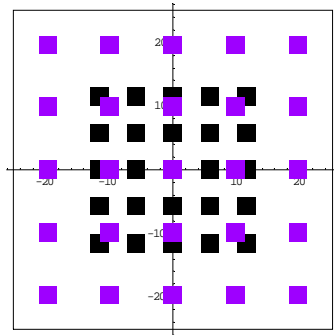


Figure 22: Optimized collimator hole pattern

Figure 23 shows the resulting fields of view superimposed on the detector pixel array and simulated weapon pit source. In the left image, the black areas represent the

fields of view on the rear face of the detector. The gray areas represent the fields of view on the front face of the detector. In the right image, the circular area represents the cross section of a 5 cm radius source centered 710 mm from the front face of the collimator. As Figure 23 shows, each collimator hole has a field of view measuring approximately 2.5 mm on each side. Thus the origin of each photon emitted can be known to within approximately 6.25 cm².

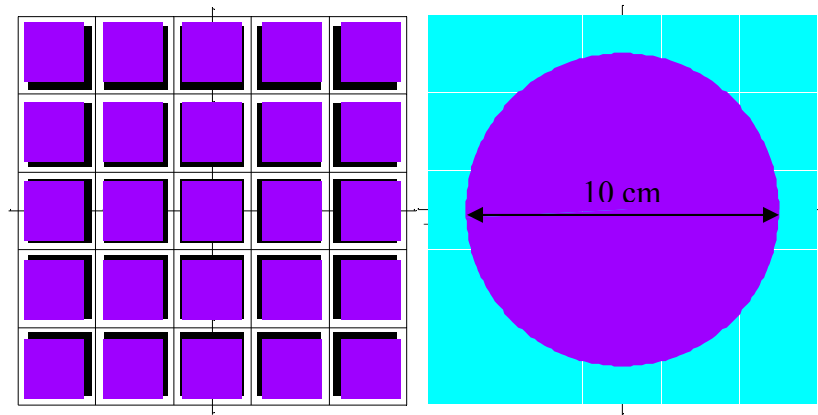


Figure 23: Collimator fields of view on the detector and source

Once the desired collimator dimensions were determined, initial mold design drawings were developed. These drawings were then taken to a local machine shop, Superior Machining Inc., for final mold design and initial fabrication. Final mold fabrication included development of the 25 square rods used to produce the holes and cutting out the square holes in the endplates for proper placement of the rods. These final fabrication steps were complete by the AFIT Model Fabrication Shop. Figure 24 shows the components of the collimator mold assembly.

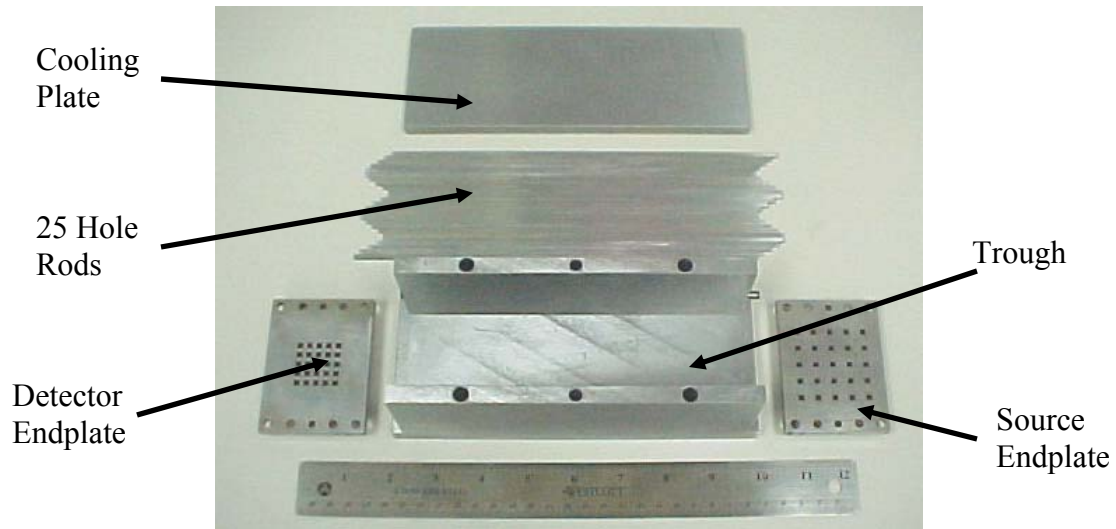


Figure 24: Collimator mold assembly

Upon completion of the mold, the final collimator was poured in house using CerroBEND. The first step for pouring the collimator was to assemble the mold. The detector and source endplates were attached to the trough and the 25 rods were placed in the endplates. Due to limitations in the electrical discharge machining (EDM) device required to cut the holes in the endplates, the square holes had to be cut perpendicular to the endplate faces. This led to the requirement of oversized holes which allow each rod to be placed at the proper angle. The use of oversized holes produced gaps on some edges between the endplates and the rods. In order to keep the CerroBEND from leaking out the gaps, I packed the gaps with white lithium grease. Each rod was also coated with a thin film of white lithium grease to aid in removal after the CerroBEND solidified.

Figure 25 shows the collimator mold fully assembled.



Figure 25: Fully assembled collimator mold

The CerroBEND used to make the collimator melts at 70° C so I melted it at 85° C to ensure I would have time to pour it before it began to solidify. Once the material was melted, I then heated the assembled mold in the oven for 15 minutes in order to keep the material from solidifying too fast as it hit the mold. The mold was then removed from the oven and the melted CerroBEND was poured in. The full mold was placed back into the oven to help remove some of the air bubbles in the CerroBEND formed while pouring. The mold was then removed from the oven and the cooling plate was placed on top of the mold to aid in uniform cooling. A small fish tank air pump was placed in the pan next to the mold as it cooled to provide vibrations which aid in removing air bubbles. As the assembly cooled, I tapped the 25 rods back and forth to help keep the CerroBEND from adhering to the rods.

Once the CerroBEND had cooled sufficiently, I then had to remove the 25 rods. Unlike most metals, as CerroBEND cools it actually expands rather than contracts. This

led to some difficulty in removing the rods, even with the application of the white lithium grease. The rods had to be driven out using a small hammer and rods of square key stock steel slightly smaller than the dimensions of the rods. Once the rods were removed and the holes were cleaned out, the collimator was placed into a base assembly fabricated to allow it to be attached to a translation stage for proper alignment with the detector.

Equipment Setup

The first step in setting up the equipment was to ensure that all of the internal switch settings and jumper settings for the Jorway crate controller were in the correct position. There are four internal switches that were all placed in the OFF position, a jumper was placed spanning X2 and X3, and it was verified that the controller was internally terminated. Then the controller was placed into the two right-most slots of the crate, and the PDM was placed into the two left-most slots.

Initially, only a single DGF-4C module was used to verify that the communication with the host computer was functioning properly. All internal jumper settings were verified as being positioned correctly for a single module. Once the ver 3.04 XIA software was installed on the host computer, it was connected to the controller with a SCSI cable and the module was successfully booted. During the start up process the SCSI bus ID number and crate number are required. The bus ID number is 2 and the crate number is set to 3 the way the system is currently configured.

Once the module was booted up a signal pulse generator was used as a signal input to become familiar with the controlling software. Figure 26 shows the setup used during this familiarization.

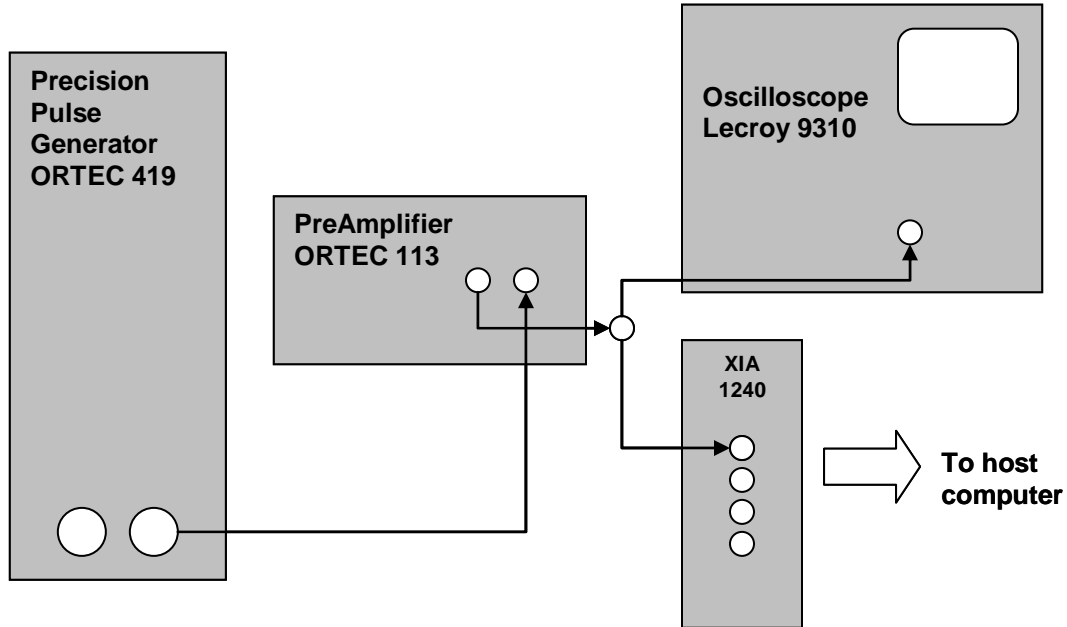


Figure 26: Experiment test setup

After becoming familiar with the software, two DGF-4C modules were placed into the crate and connected across their backplane to distribute the master clock, and the internal jumpers were all placed in the XIA recommended positions. The following notation is used throughout this project, module 1 (rear strips) is the right XIA module and module 2 (front strips) is the left XIA module. The following jumper settings were used when both modules were placed in the crate together.

Table 3: DGF-4C module jumper settings

| | Module 1 - 1244 | Module 2 - 1240 |
|----------|-----------------|-----------------|
| Jumper 1 | Installed | Removed |
| Jumper 2 | Installed | Removed |
| Jumper 3 | Installed | Installed |
| Jumper 4 | Installed | Installed |
| Jumper 5 | Board Clock | External |

After the modules were placed in the crate, a ribbon cable provided by XIA was used to connect the modules together via the 8 pin connectors on the back of each module. Figure 27 shows the backplane connections as viewed from behind the modules.

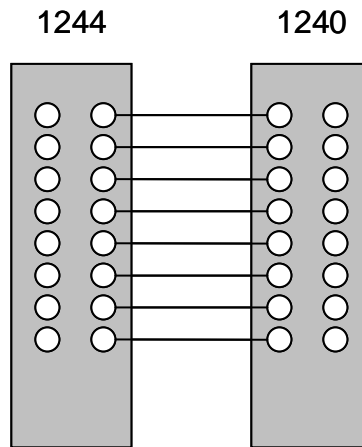


Figure 27: DGF-4C module backplane connection

After the modules had been hooked together across the backplane, the logic module was connected to the front of the modules. The DGF ‘busy out’ connectors were hooked to the input of the logic module, and the DGF ‘synch in’ connectors were hooked to the output of the logic module. Once all connections had been made, the two modules were booted up and four pulse generators were connected to the inputs of the DGF-4C’s. All four of the signals were recorded by the DGF software in MCA mode, showing that the system was functioning properly and ready for the detector outputs to be connected to the DGF-4C modules.

The dewar for the HPGeDSSD was verified to be full and the detector was connected to an ORTEC 659 high voltage power supply. The power supply internal

board was placed in the positive polarity position, and in a position to allow automatic shut off. The high voltage shut down (HVSD) connector, on the detector, was hooked to the back of the power supply at its automatic shut down connection. This is a safety feature which will force a shutdown of the high voltage power supply if the detector temperature is allowed to rise above liquid nitrogen levels.

The high voltage supply line was hooked to the HV-In connector on the detector, and the PDM was connected to the preamplifier supply connection on the detector. The detector outputs were connected to the DGF-4C modules. For this work, strips F1-F4 and R1-R4 were used to produce the desired four by four array. Then the high voltage power was turned on and slowly increased to +1000 volts in 100 volt increments. At each increment of 100 volts, the detector outputs were observed using the oscilloscope feature in the DGF software to ensure that as power was increased the noise on each channel decreased. Table 4 lists which connections were made between detector outputs and DGF-4C module inputs.

Table 4: Detector output to DGF-4C module connections

| Detector | Module | Channel |
|----------|--------|---------|
| Output | Number | Number |
| F1 | 2 | 0 |
| F2 | 2 | 1 |
| F3 | 2 | 2 |
| F4 | 2 | 3 |
| R1 | 1 | 0 |
| R2 | 1 | 1 |
| R3 | 1 | 2 |
| R4 | 1 | 3 |

The XIA notation for connectors is: the top connector on the DGF-4C modules is channel 0, and the bottom connector is channel 3.

Noise

Noise present on each detector strip can be viewed using the oscilloscope function within the DGF software. During application of the high voltage bias to the detector, the noise can be observed to ensure it decreases as the bias increases. Failure of the noise to decrease would indicate a problem with the bias being applied.

Charge Sharing Between Strips

To ensure complete charge collection was being achieved, all ten detector outputs were viewed simultaneously on oscilloscopes. Two four channel and one two channel oscilloscopes were used. All ten of the channels were set to trigger off of the channel displaying the detector output F1. Each pulse could then be matched to a single pulse or multiple pulses occurring on the opposite face of the detector.

Software Settings

Preamplifier decay constants: One of the user inputs within the XIA software is the preamplifier decay constant. This is used by the software to correct for pulses that arrive before the previous pulse has returned to baseline. Since the response of each strip is slightly different, a preamplifier constant is required for each strip. Optimization of the

preamplifier decay constant is performed using the DGF software. Ten values of the constant are calculated and the average value is shown to the user for acceptance or rejection.

Gain Settings: Proper energy calibration of each strip is crucial when imaging in a narrow energy range. This requires that each strip be carefully calibrated to the same energy scale. This is accomplished by adjusting each strip gain setting so that it will place the centroid of a full energy peak (FEP) at a specified channel. The FEP chosen for the energy calibration was the 392 keV peak from Sn-113. The location for this peak was chosen to be channel 20200.

Energy Filter Rise Time: Optimization of energy resolution was performed by determining the energy filter rise times which resulted in a minimized FWHM for each strip. This was done at the suggestion of the XIA users guide for maximizing performance. Fourteen data points were taken at different energy filter rise times, and each spectra resolution was measured. All measurements were taken using a Cs-137 source with a collection time of 600 seconds.

Common XIA Software Settings: Each of the DGF-4C modules and channels has other settings that have to be set within the software. Many of the settings are the same for all of the channels. The settings that are constant for each channel are listed in Table 5.

Table 5: Common XIA software settings

| | |
|--|------|
| Trigger filter rise time (μs) | 0.1 |
| Trigger filter flat top (μs) | 0.1 |
| Energy filter flat top (μs) | 2.4 |
| Threshold | 200 |
| Cutoff | 5000 |
| Binning factor | 1 |
| Coincidence pattern | 115E |

Resolution Determination

As described above, the energy filter rise time was optimized for each strip in an attempt to optimize the resolution of the detector as a whole. For the purpose of imaging, the resolution was measured at 391.7 keV with emissions from the Sn-113 isotope, in the activated Sn source, with a counting time of 36,000 seconds. The resolution of each of the charge collection strips was measured using a normal distribution fit that is performed by the XIA software. The fit was used because it automatically subtracts out the background. The fit gives both the absolute FWHM, and the percentage FWHM. For purposes of reporting the resolution, the absolute FWHM value is used.

Efficiency Calculation

To determine the efficiency of the detector, four radiation sources of known activities were used, for a total of six full energy peaks. The efficiency decreases with increasing photon energy. Depending on its activity, each source, one at a time, was placed at a specified distance along the axis of the detector. The counting time for each source was also varied depending upon the source activity. For the calculation of the

solid angle, I assumed a right circular detector with a radius that had a surface area equal to the surface area of the ORTEC detector. I then established a setup with a source-to-detector separation much larger than the source dimension. This allowed me to use the following equation for calculating the solid angle [6]

$$\Omega = 2\pi \left(1 - \frac{d}{\sqrt{d^2 + a^2}} \right) \quad (3)$$

where:

Ω = Solid angle

d = Distance between the source and detector [cm]

a = Detector radius [cm]

The intrinsic efficiency was then calculated using the following equation [6]

$$\varepsilon_{\text{int}} = \frac{\text{counts recorded}}{A \cdot t \cdot b \cdot \frac{\Omega}{4\pi}} \quad (4)$$

where:

ε_{int} = Intrinsic efficiency

A = Activity of the source (Bq)

t = Counting time (sec)

b =Branching ratio

Ω = Solid angle

Collimator Alignment

Proper alignment of the converging collimator with the detector strips is required to create an image with proper spatial resolution. Proper alignment is defined as aligning each collimator hole with only one corresponding detector pixel. This ensures that a

gamma photon producing an event in a particular pixel originated from within a known volume of the source. Initially, I assumed that the detector was located in the center of the cylindrical cryostat housing. The detector manufacturer reports that the front detector strips are between 10 and 15 mm from the front of the cryostat housing. This uncertainty required that proper collimator alignment be performed experimentally.

The collimator was placed into a base assembly and secured to a three axis adjustable stage. The collimator was then aligned with the approximated center of the cryostat housing, and spectra of a point Eu-152 source located at the center collimator hole were taken. Figure 28 shows the configuration used for this step. The actual Eu-152 source is only 5mm diameter so it is only visible through one collimator hole when properly positioned. The collimator was then repositioned according to the resulting spectra. This process was repeated until the source peak was seen only on the two strips corresponding to the center pixel, namely strips R3 and F3.



Figure 28: Center pixel alignment configuration

The next step was to ensure proper alignment of the remaining pixels. This was performed by placing the Eu-152 source at one of the collimator corner holes and acquiring new spectra. The distance from the collimator to the cryostat housing was then adjusted according to the resulting image. This process was repeated until the image of the point source was located in the appropriate pixel. Proper alignment was then verified by placing sources at the opposite corner hole of the collimator and ensuring that the collimator hole covered only one detector pixel. Once the collimator alignment was complete, data acquisition was ready to begin.

Imaging

To create images, the raw data were collected by the detector, and processed by the MATLAB image processing code presented in Appendix B. The resulting images were then analyzed in order to determine certain characteristics of the system.

Data Collection: For the collection of imaging data, the XIA software must be set to take list mode data. In the run tab of the XIA software, the run type must be set to energy and time only. In this list mode, only the hit patterns, timestamps and energies are stored for each event. During operation, the memory in the level 1 buffer for each input can only store up to 744 events, and then it must dump the data to a larger memory. Each of the collections of 744 events is referred to as a spill. Within the XIA software one can specify a maximum time for each spill, assuming that the buffer is not filled before the time runs out. One also must specify the number of spills to be stored during data collection. Once the data collection is complete, the DGF-4C module downloads all of

the data to the PC as a binary file. Within the XIA software, the data can be converted from its binary form and saved as a text delimited file. It is this file that is read in by the image processing code.

Image Processing Code: Chapter 3 presents the key algorithms found in the code. The actual code is presented in Appendix B. Application of the code requires a few user inputs. First, the user must choose how many energy windows to image within. The user must then choose to use only two strip events or both two and three strip events. Next, the user selects the upper and lower limits of the energy windows. The last user input is whether to accept the default energy calibration or input a new one. The code then proceeds to read in and process the raw data. The final output of the code includes a figure window with the four by four pixel image of the source as seen from the detector along with a surface plot of the image and a histogram showing the number of counts for each energy within the specified range. The resulting images can be exported to a desired location in various formats for further analysis.

Image Analysis: The image processing code proved to be a valuable tool for analyzing certain features of the images. The primary areas of interest for the image analysis included the utilization of two strip events versus three strip events, the ability to distinguish a point source from a distributed source, and the ability to image using multiple energy windows. Data were taken for several image configurations including single source and multiple source setups. The images were then processed using a variety of energy windows in order to explore the above mentioned areas of interest.

V. Results

Chapter Overview

This chapter presents the results of the detector characterization, the statistics involved with the imaging, and the actual imaging done with the detector.

Noise

When measuring the noise present on each of the channels, it was found that the R2 pre-amplifier output had an approximately 10% larger noise component than any of the other charge collection strip outputs. The oscilloscope built into the DGF-4C controlling software was used for these measurements. All channels showed noise characteristic of low frequency mechanical or seismic vibrations. One possible explanation to the increase in noise on channel R2 is that the pre-amplifier is more sensitive to the above mentioned vibrations. The extra noise on this strip does not degrade the energy resolution considerably. Figure 29 shows a comparison between the charge collection strip R2 noise level and the R4 strip noise level. The other six charge collection strips have noises that are comparable to the R4 strip.

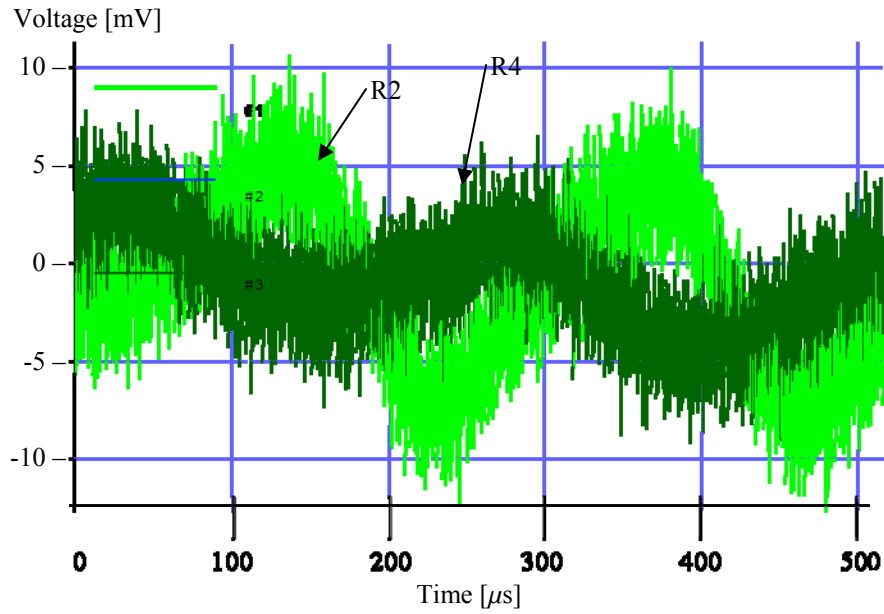


Figure 29: Pre-amplifier noise comparison between two strips

Charge Collection/Sharing

To ensure that full charge collection is accomplished, the preamplifier outputs were viewed on multiple oscilloscopes as discussed in chapter 4. Figure 30 shows the preamplifier outputs resulting from a coincident event recorded on two strips, one front strip and one rear strip. This event is the result of a gamma depositing energy in only one detector pixel. It is clear that the same amount of charge is collected on each strip. Thus it is assumed that the gamma deposited energy in only one pixel and the entire charge was collected.

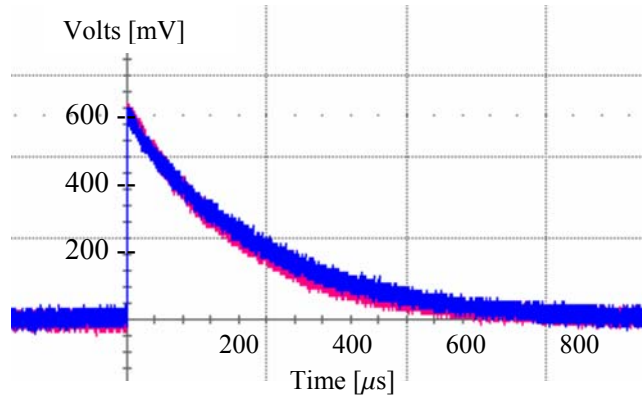


Figure 30: Two strip event charge collection

Figure 31 shows the resulting preamplifier outputs resulting from a coincident event recorded on three strips, one rear strip, R3, and two front strips, F1 and F2. Although not obvious at the scale presented, the pulse recorded on strip F2 was recorded approximately 25 ns before the pulse on strip F1. This leads to the assumption that the original gamma entered the detector at the pixel defined by the intersection of strips F2 and R3. The pulse recorded on strip F2 was apparently the result of one or more Compton scattering events which eventually caused the reduced energy gamma to enter the pixel defined by the intersection of strips F1 and R3 where it continued to deposit energy. The single pulse recorded by strip R3 is a result of the very short amount of time between the Compton scatter interaction(s) and the final photoelectric absorption interaction.

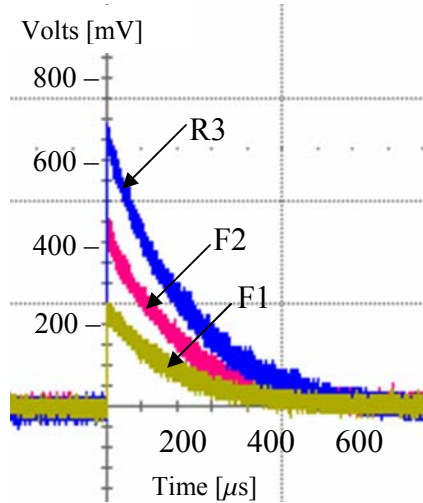


Figure 31: Three strip event charge collection

The charge sharing between the two front strips is obvious. Close analysis shows that the sum of the charge collected on the two rear strips is equal to the charge collected on the front strip. The same results were found if the charge sharing was between two rear strips. Once again, this leads to the assumption that full charge collection is being accomplished.

Preamplifier Decay Constant (TAU)

One of the user inputs within the XIA software is the preamplifier decay constant. As discussed in 4, the DGF software contains a function for obtaining this value. It does so by computing ten values for the preamplifier decay constant of a specified strip and returning the average of the ten. The user is then able to keep the computed value, obtain a new average, or use a built-in function to find the value computed from a single pulse.

For this work I utilized the built-in averaging function and obtained the values shown in Table 6.

Table 6: Pre-amplifier decay constants

| Strip | Tau [μ s] |
|-------|----------------|
| F1 | 47.4 |
| F2 | 43.8 |
| F3 | 41.8 |
| F4 | 52.1 |
| R1 | 43.1 |
| R2 | 45.0 |
| R3 | 47.6 |
| R4 | 45.7 |

Energy Calibration

As described in Chapter 4, proper energy calibration is crucial in order to image within a given energy range. This requires that the gain setting for each strip be adjusted so that the centroid of a specified full energy peak is recorded in a predetermined channel. For this work, the specified peak centroid of 392 keV was aligned with channel 20200. As shown in Table 7, this required different gain settings for each strip. Because of the inability to reproduce exact high voltage bias values, new gain setting adjustments are required when the high voltage bias is removed from the detector. The settings shown below are those used when determining the energy resolution of the detector. Each setting was verified by conducting several runs to ensure the centroid channel number did not shift by more than ± 1 channel. According to these settings, the largest difference between a particular centroid on different charge collection strips should be four channels.

Table 7: Gain settings

| Output | Gain | Channel |
|--------|--------|---------|
| F1 | 1.3084 | 20203 |
| F2 | 1.2718 | 20202 |
| F3 | 1.1970 | 20198 |
| F4 | 1.1967 | 20200 |
| R1 | 1.2895 | 20202 |
| R2 | 1.2347 | 20201 |
| R3 | 1.2460 | 20199 |
| R4 | 1.2225 | 20200 |

After all eight charge collection strips had been calibrated, the energy calibration had to be known for use in the image processing code. The energy of an event in raw data is recorded in the list mode data collection as a channel number. There is no way of determining the energy calibration scale within the XIA software. So the raw data were read into the image processing code as channel numbers, and the code allows the user to either accept a default calibration or manually enter the energy calibration. The default energy calibration used by the image processing code used six full energy peaks, whose values of channel and energy were plotted in Excel. Once the data were plotted, Excel performed a least squares fit on the data and determined an equation of the line. The plot of the data is shown in Figure 32.

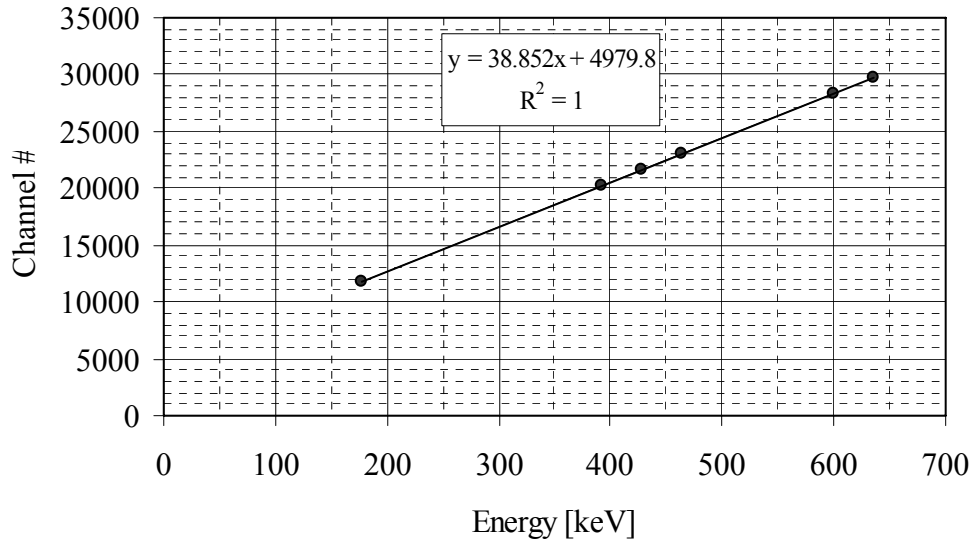


Figure 32: Energy calibration of the HPGeDSSD

The calculated value of the least squares fit is

$$\text{Channel} = 38.852 * \text{Energy}[\text{keV}] + 4979.8 \quad (6)$$

Since the data were collected in MCA mode with an energy cutoff of 5000, the data were shifted to the right by 5000 channels. This does not occur when operating in list mode data collection, so the energy fit used within the code is

$$\text{Channel} = 38.852 * \text{Energy}[\text{keV}] - 20.2 \quad (7)$$

Rise Time Optimization

The resolution of the detector is dependent on both the rise time and flat top time of the energy trapezoidal filter. The XIA documentation suggests that the resolution is relatively independent of the flat top time, and highly dependent on the energy filter rise

time. It also suggests that the values of the energy filter rise time should be varied in order to determine the optimal rise time for each charge collection strip. To optimize the rise time of individual strips, eleven values of the energy filter rise time were used, and the FWHM of the 392 keV full energy peak of a tin strip source were measured. Figure 33 is a plot of the eleven values obtained for each strip.

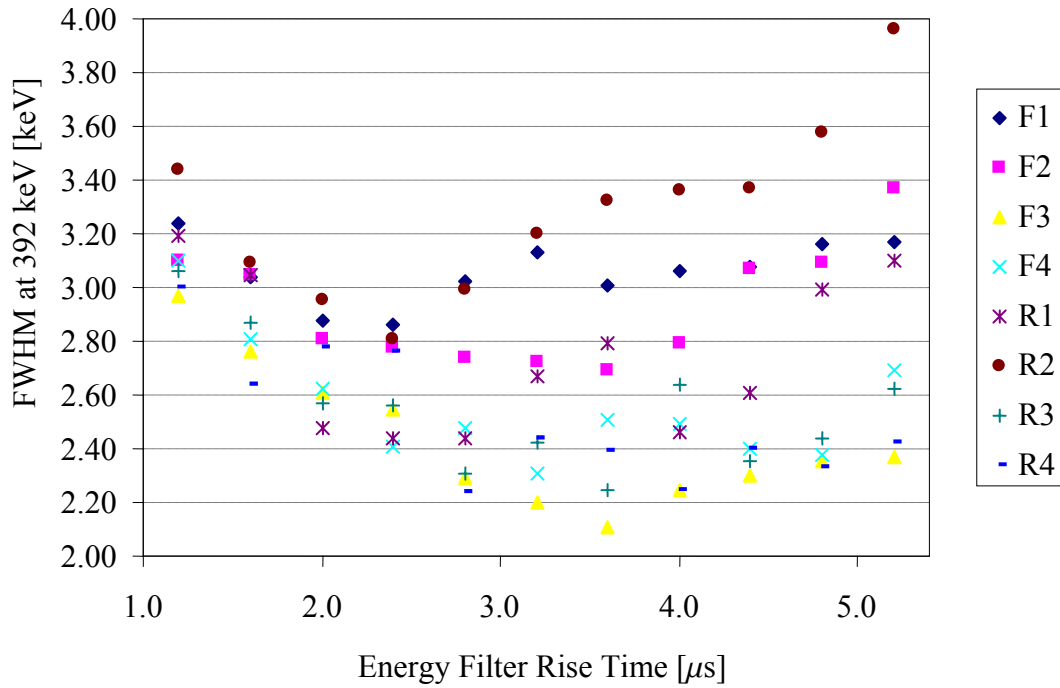


Figure 33: Plot of FWHM vs. energy filter rise time

The minimum resolution for each strip occurred at various rise time values. Therefore, the best optimization should be achievable by using the best rise time for each charge collection strip individually. However, because of a limitation in the DGF-4C controlling software, using various energy filter rise times restricts the coincident time window allowed for determining coincident events in adjacent strips. The desired

coincidence window is 100 ns. If two strips have energy filter rise times varying by just $0.4\ \mu\text{s}$, the shortest coincidence window allowed is 400 ns. This led to the use of a $2.4\ \mu\text{s}$ energy filter rise time for all charge collection strips. This value was chosen in order to maintain the narrowest energy window for imaging.

Energy Resolution of the Detector

In order to characterize a detector, the energy resolution must be known. Chapter 4 discusses the process of measuring the energy resolution. Since the HPGeDSSD has ten charge readouts, each of these must be characterized. Figure 34 is one example of the spectra collected to measure the resolution. All eight charge collection strips were measured and the remaining seven spectra are shown in Appendix C. The time for the data collection was 36000 seconds.

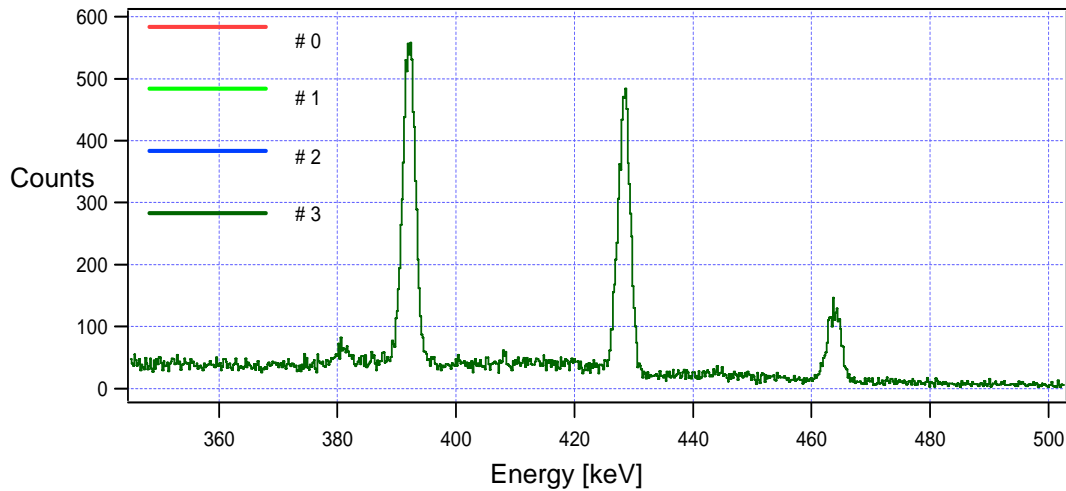


Figure 34: Strip R4 activated Sn spectrum used for resolution measurement

From each spectrum the XIA software was used to find the absolute FWHM of each of the full energy peaks. Figure 35 shows the FWHM measurements for all of the

charge collection strips using a $2.4\ \mu\text{s}$ energy filter rise time. These measurements of FWHM can be used to help determine the width of the energy window required for imaging. The energy window for imaging a particular isotope must be wide enough to include the minimum and maximum expected values for the particular full energy peak across all charge collection strips. For this work it was found that an energy window of about 6 keV is sufficient for comparing charge pulses collected on opposite faces of the detector. This value corresponds to approximately two times the FWHM for the worst charge collection strip, namely R2.

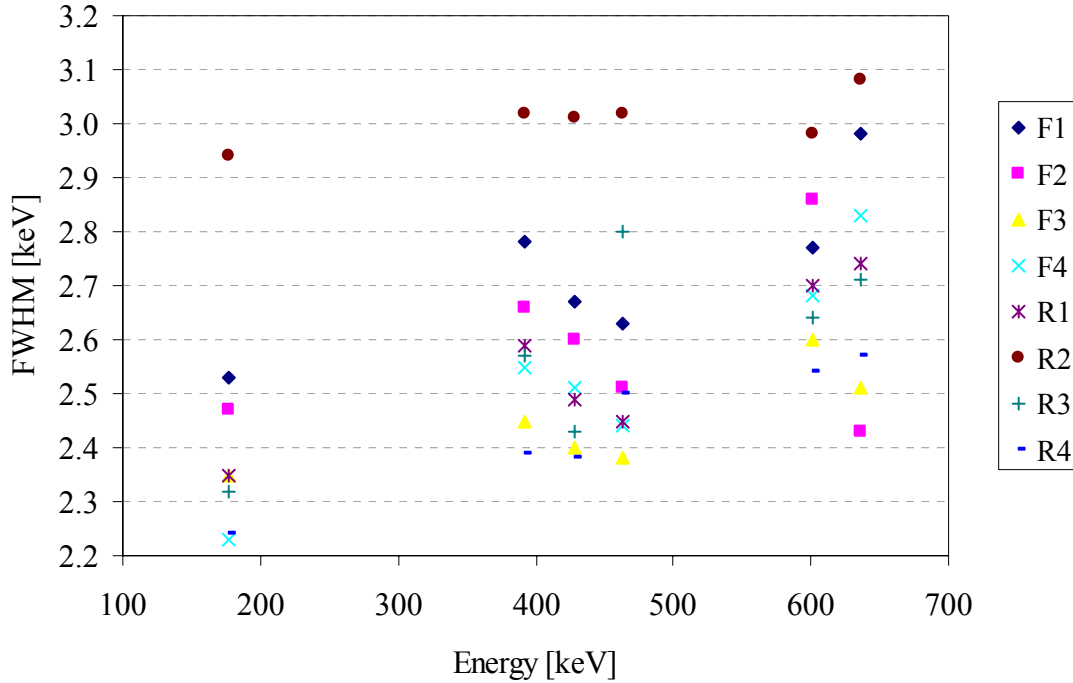


Figure 35: Plot of FWHM vs. energy for individual charge collection strips

Peak Efficiency of the Detector

The peak efficiency of the detector must be known in order to determine the time required to produce an image. As discussed in Chapter 4, the peak efficiency was measured for six full energy peaks. Table 8 shows the values of efficiency that were measured using four radiation sources, and Figure 36 shows the data plotted on a log-log scale.

Table 8: Detector efficiency measurements

| Full energy peak [keV] | Intrinsic Peak Efficiency |
|------------------------|---------------------------|
| 122 | 0.44121 |
| 244 | 0.088358 |
| 344 | 0.042821 |
| 392 | 0.031591 |
| 511 | 0.020091 |
| 662 | 0.010875 |

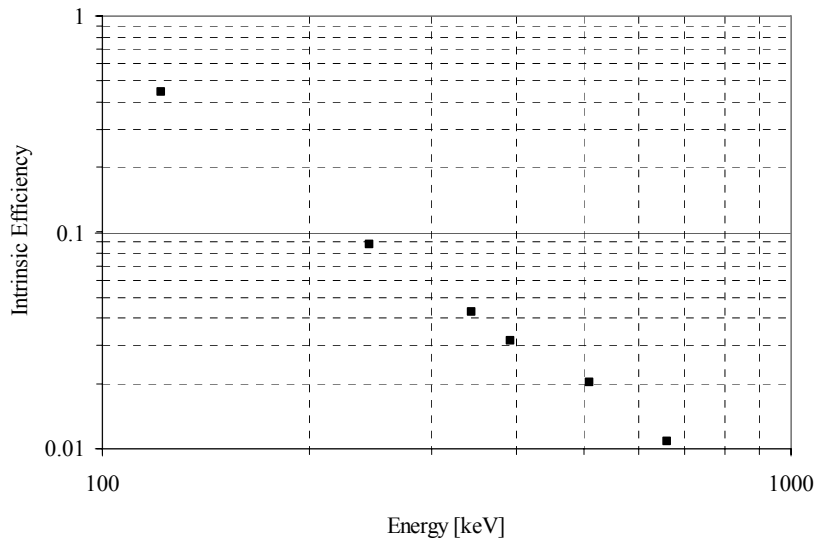


Figure 36: Detector peak efficiency measurements

The higher efficiency found around 122 keV is due to the fact that photoelectric absorption dominates over Compton scattering up to about 200 keV. This domination of photoelectric absorption increases the likelihood that these lower energy gammas will deposit all of their energy within the germanium. On the other hand, as the energy increases the likelihood increases that the gamma will undergo one or multiple Compton scatters and then depart from the detector. This results in a lower percentage of gammas that deposit their entire energy in the germanium, thus decreasing efficiency with increasing gamma energy. More analysis would be required to determine an optimum detector crystal design which would increase the peak efficiency of the detector.

Investigation of edge pixel collimator holes

As discussed in Chapter 4, I investigated the feasibility of using collimator holes located at the edge of the detector pixels. Other research investigating the response near a strip gap was performed at the European Synchrotron Radiation Facility [12]. This work used a source beam of x-rays ranging from 15 to 100 keV collimated to 10 microns wide. The results showed that a very large number of full energy peaks were recorded when the source was about 50 microns from the gap. This would then require a collimator hole width of less than 100 microns to ensure that charge would be shared between two strips most of the time. What I had hoped to find was that the distance from the gap which resulted in a large percentage of three strip events would be significantly larger for higher

energy photons, resulting in the ability to use edge pixel holes with high enough efficiency for imaging.

Using a 1 mm by 25 mm collimated tin strip source, I gathered spectrum at various locations near the edge between strips R2 (channel # 1) and R3 (channel # 2).

Figure 37 shows the spectrum taken with the center of the collimated source located 0.5 mm from the gap towards the center of strip R2.

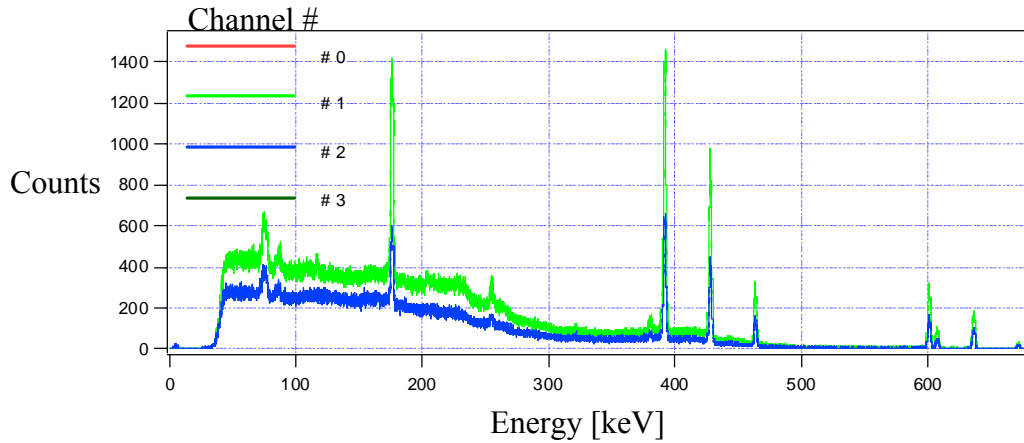


Figure 37: Edge pixel test spectra

As the spectrum above shows, both strips recorded a very large number of full energy peaks. The current system of processing an event does not provide a way to distinguish a full energy peak recorded near the gap from a full energy peak recorded at the center of a detector strip. This causes all full energy peaks to be recorded as center pixel events. Only full energy peaks which share charge between two strips on one side of the detector and is recorded as a full energy peak on the opposite side could be assigned to an edge pixel. Therefore, the edge pixel hole diameter would have to be less than 2 mm. A hole less than 2 mm diameter does not provide enough efficiency for imaging. Also, in order to maintain a true image, all holes should be the same size in

order to provide approximately the same efficiency. This would preclude the use of different hole sizes for edge pixels and center pixels, which would require obtaining a good point spread function for each pixel based on its size and location.

The results of the edge effect test showed that I would not be able to increase the spatial resolution of the system by adding edge hole pixels. This led me to use only one collimator hole per detector pixel. However, I was still able to use three strip events by assigning them to a single detector pixel.

Collimator Alignment

Proper alignment of the converging collimator is critical for proper spatial resolution of an image. As discussed in Chapter 4, the first step in aligning the collimator was to align the center hole of the collimator with the center pixel of the detector. This was done by aligning the collimator with the approximate center of the detector using a Eu-152 source on the center collimator hole. Spectra were then taken and the collimator position was adjusted according to the spectra. This process was repeated until the source was seen only at the center pixel. Figure 38 and Figure 39 show the final spectra taken for this step. Since the peaks were clearly present only on strips R3 and F3, both channel #2, it was assumed that the collimator was indeed centered on the detector.

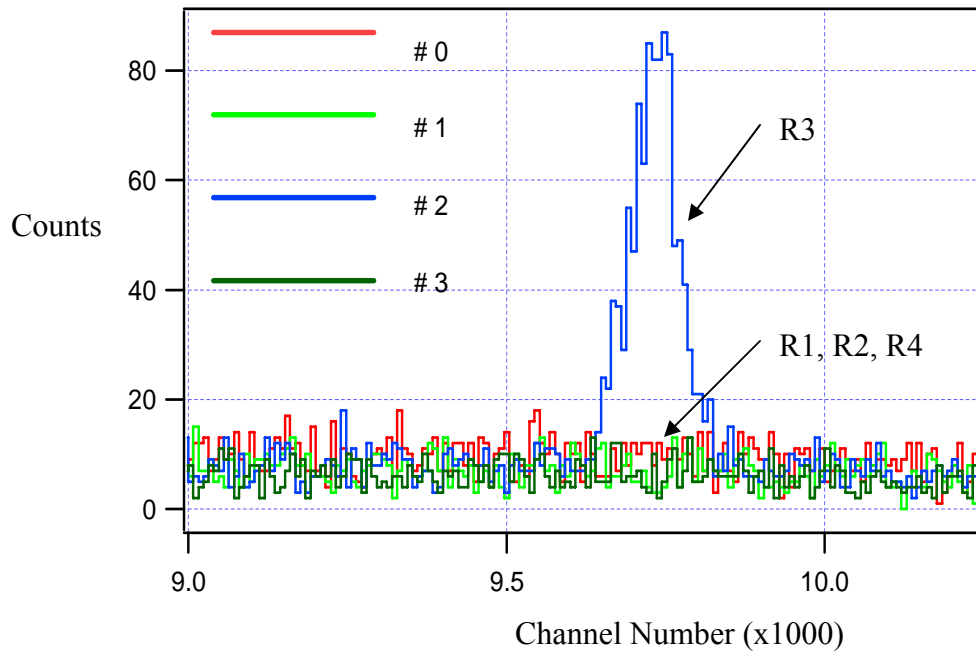


Figure 38: Rear strip spectra for center pixel alignment

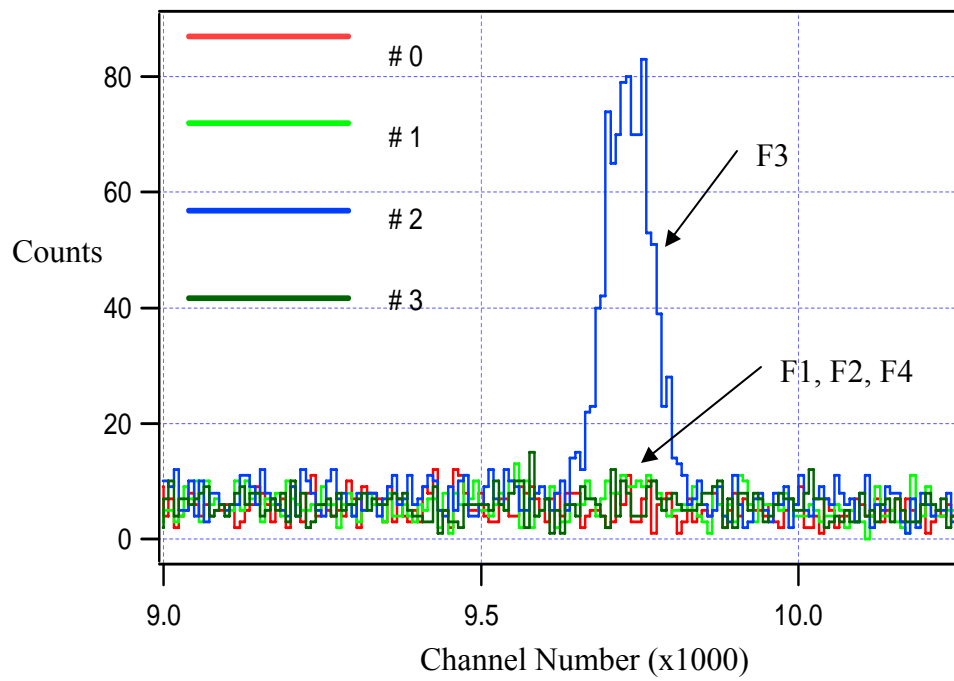


Figure 39: Front strip spectra for center pixel alignment

The next step in aligning the collimator involved placing the source at the top right image pixel of the detector and taking spectra. Just as before, the spectra were analyzed and the collimator was adjusted accordingly. After only a few adjustments, the top right pixel was properly aligned. Figure 40 and Figure 41 show the final spectra taken, which verified proper alignment of the top right pixel. Proper alignment is inferred from the fact that on strips R1 and F1 show the peak.

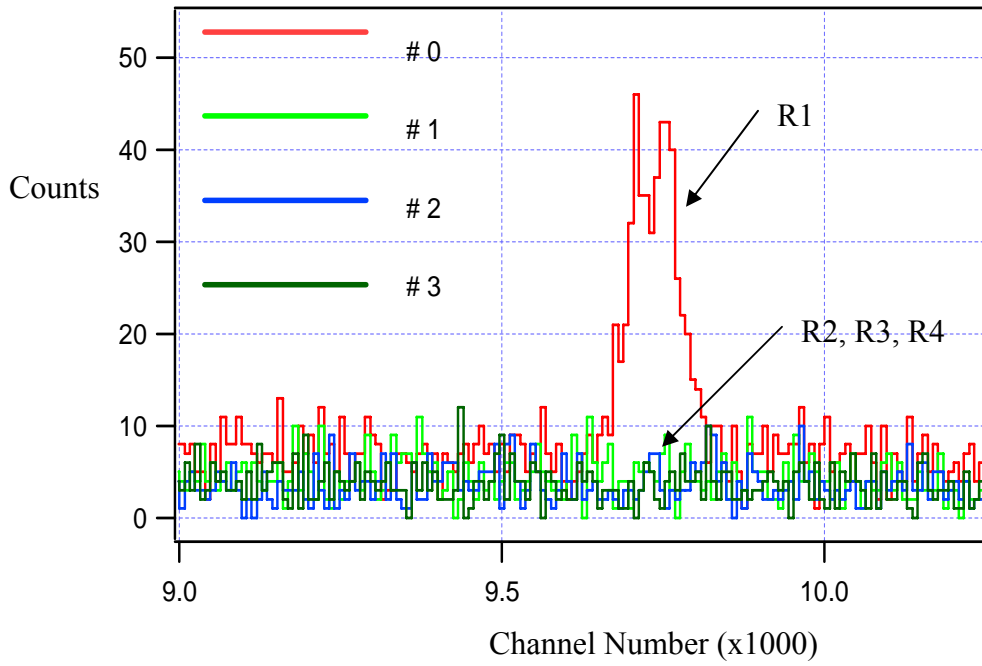


Figure 40: Rear strip spectra for top right pixel alignment

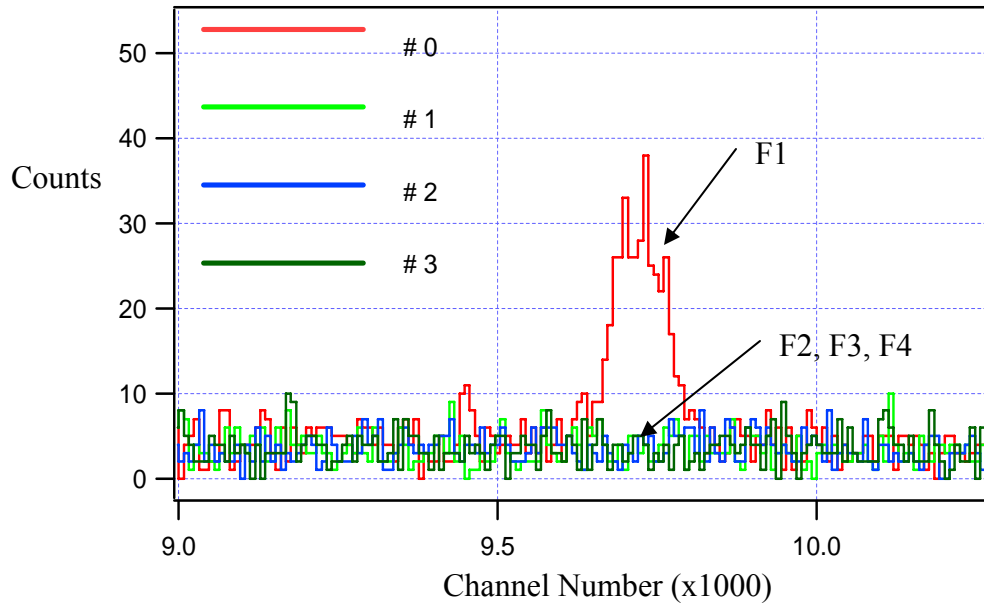


Figure 41: Front strip spectra for top right pixel alignment

The same process was repeated for the bottom left image pixel to verify proper alignment. Figure 42 and Figure 43 show the resulting spectra for the bottom left pixel. Just as before, proper alignment was inferred from the fact that strips R4 and F4 show the peak. With the detector properly aligned, I was then ready to begin taking image data.

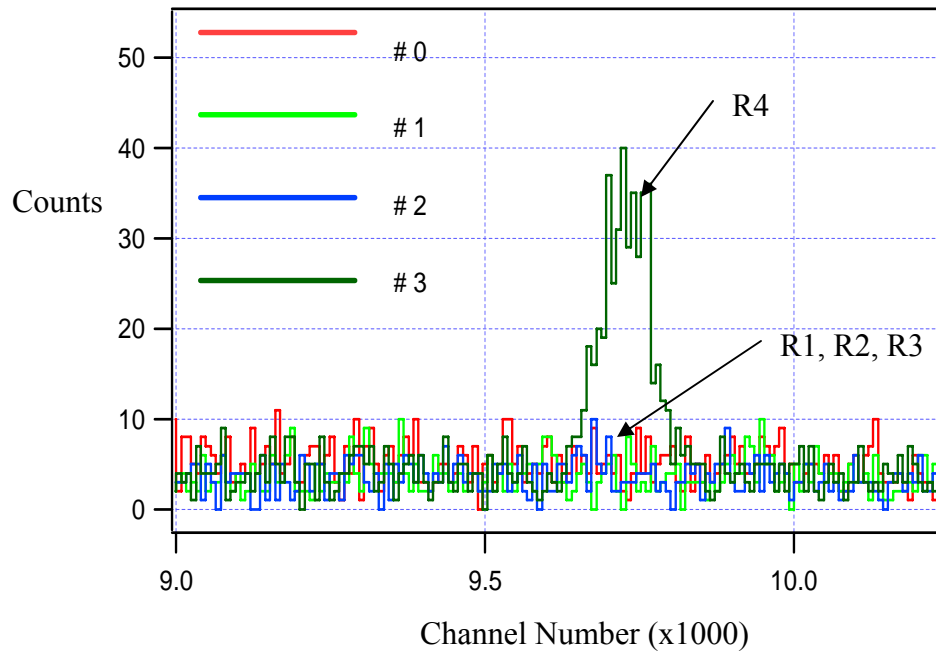


Figure 42: Rear strip spectra for bottom left pixel alignment

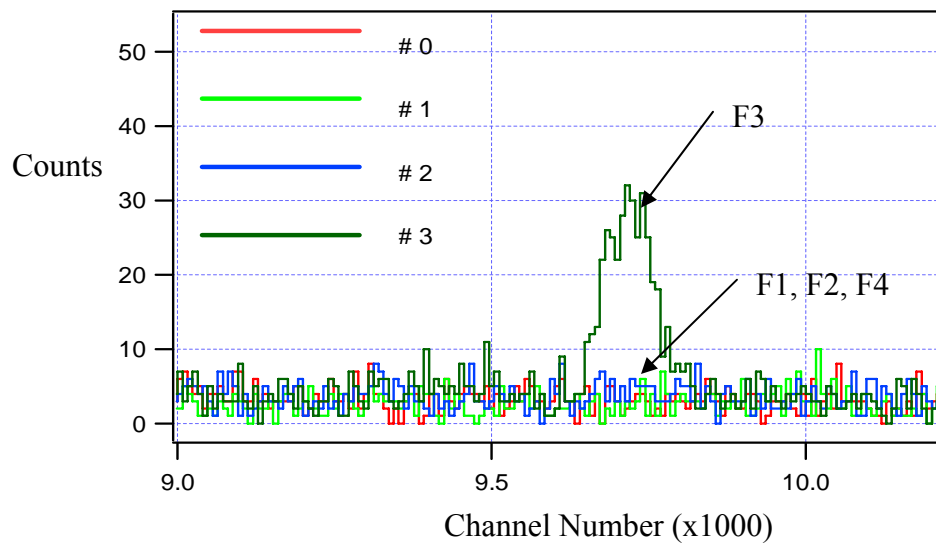


Figure 43: Front strip spectra for bottom left pixel alignment

Image Formation

Several representative images were collected to demonstrate the performance of the detector. As discussed in Chapter 4, the areas of interest for image analysis included the utilization of two strip events versus three strip events, the ability to distinguish a point source from a distributed source, and the ability to image using multiple energy windows. The resulting MATLAB outputs are shown below. Each output consists of a four by four pixel standard grayscale image, a three dimensional surface plot of the image showing relative counts in each pixel, and a histogram showing the number of counts for each 1 keV increment within the specified energy windows. For each of the standard pixel images and surface plots, black represents zero counts and white indicates the highest number of counts within the image. A grayscale legend is also provided to assist in comparing variations in the image.

Figure 44 shows the image results of a Cs137 point source that was imaged for 9426 seconds and processed using only two strip events and a 660-666 keV energy window. Table 9 shows the resulting image matrix for Figure 44.

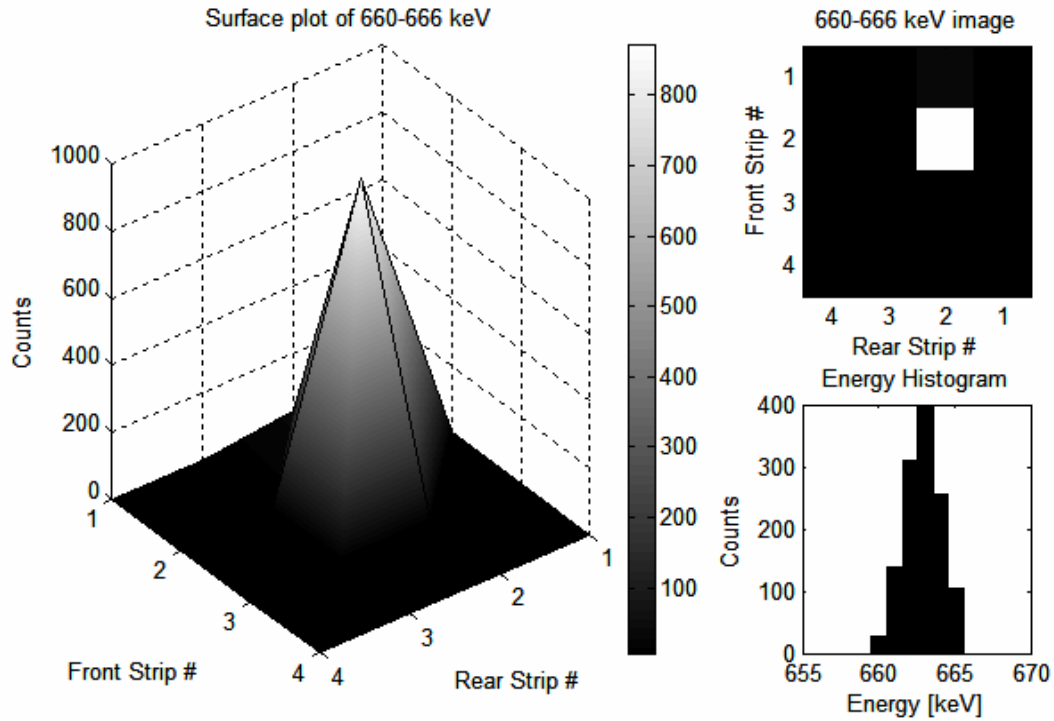


Figure 44: Cs-137 point source image results using only two strip events

Table 9: Cs-137 point source image matrix using only two strip events

| | | | |
|---|---|-----|---|
| 0 | 0 | 32 | 0 |
| 0 | 4 | 877 | 0 |
| 0 | 1 | 1 | 0 |
| 1 | 0 | 0 | 0 |

Good collimation of the source in Figure 44 is evident by the relatively low number of counts recorded in pixels which were not visible to the source. Several other pixels were tested for good collimation with similar results to those shown above. Time precluded gathering enough data to develop a point spread function to account for efficiency differences between the detector pixels. Therefore, for this work it was assumed that the efficiency from pixel to pixel was relatively constant.

Figure 45 shows the image results of processing the same data set as that used in Figure 44 using both two and three strip events and the same 660-666 keV energy window. Table 10 shows the resulting image matrix for Figure 45.

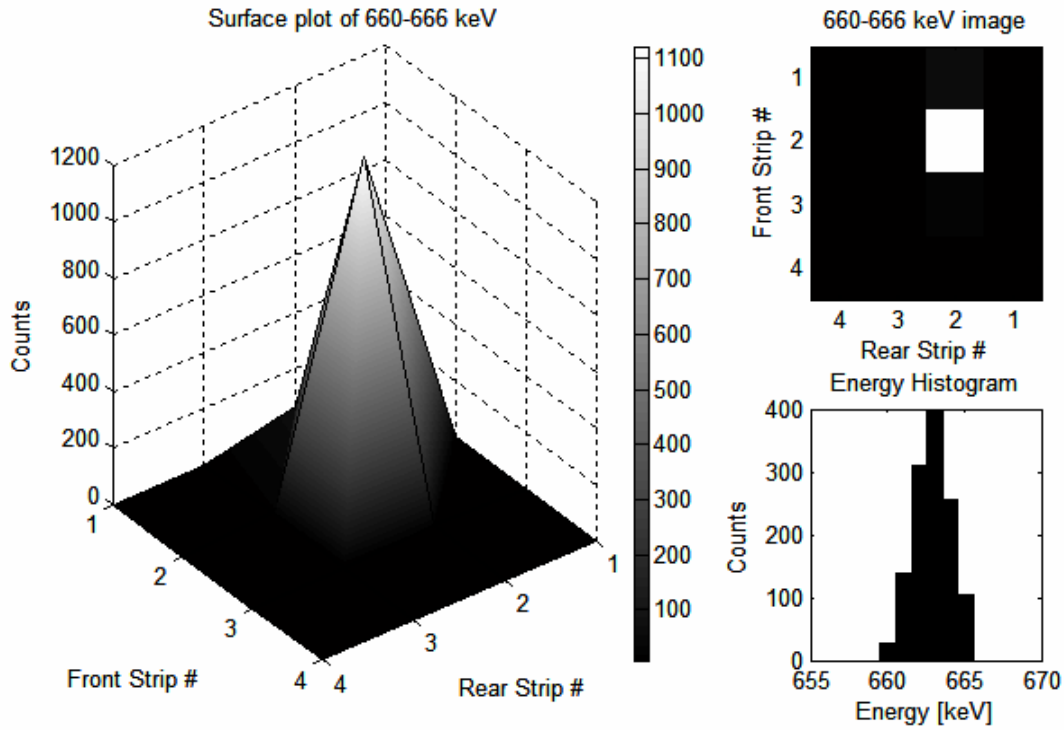


Figure 45: Cs-137 point source image results using two and three strip events

Table 10: Cs-137 point source image matrix using two and three strip events

| | | | |
|---|----|------|---|
| 0 | 0 | 65 | 0 |
| 0 | 16 | 1131 | 2 |
| 0 | 1 | 18 | 0 |
| 1 | 0 | 0 | 0 |

Comparison of Figure 44 and Figure 45 shows that the addition of three strip events increased number of counts recorded in the illuminated pixel by 28%. On the

other hand, this increase in counts comes at the cost of significantly increasing the number of counts in the adjacent nearest neighbor pixels. At first glance one may conclude that the addition of three events degrades the image. However, many more images would be required in order to quantify the effect of adding three strip events. For applications which involve very low count rate, such as with on site weapon inspections, the addition of three strip events could prove crucial to obtaining enough counts for a viable image. Further research is required to determine when the use of three strip events can be justified.

Figure 46 shows the image results of an activated Sn distributed source comprised of five Sn strips in the shape of the letter “A” which was imaged for 30526 seconds, approximately 8.5 hours. The image was developed using two energy windows, namely 389-395 keV and 424-430 keV. Recall that these are the peaks chosen to simulate Pu-239 in a weapon storage cask. The histogram of the image clearly shows that each energy window made a significant contribution to the final image. Figure 47 and Figure 48 show the contributions each energy window made in Figure 46. These images show the ability to image a distributed source of SNM using either a single or multiple energy windows. Comparison of these distributed source images to those obtained from a point source clearly show the ability of the system to distinguish a point source from a distributed source.

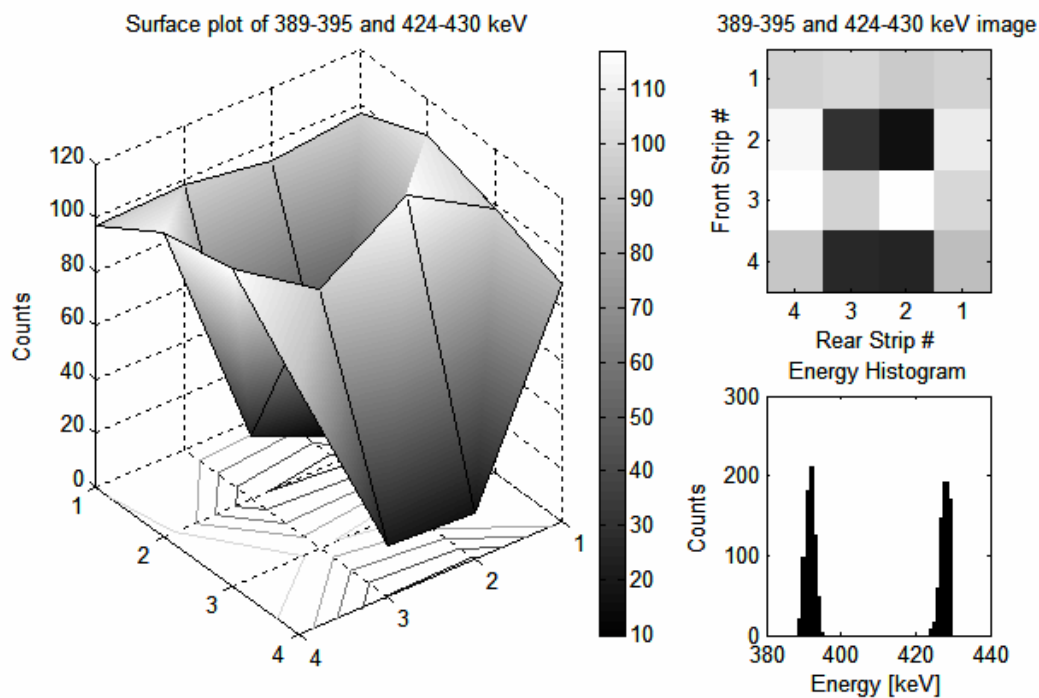


Figure 46: Image results of distributed Sn source using two energy windows

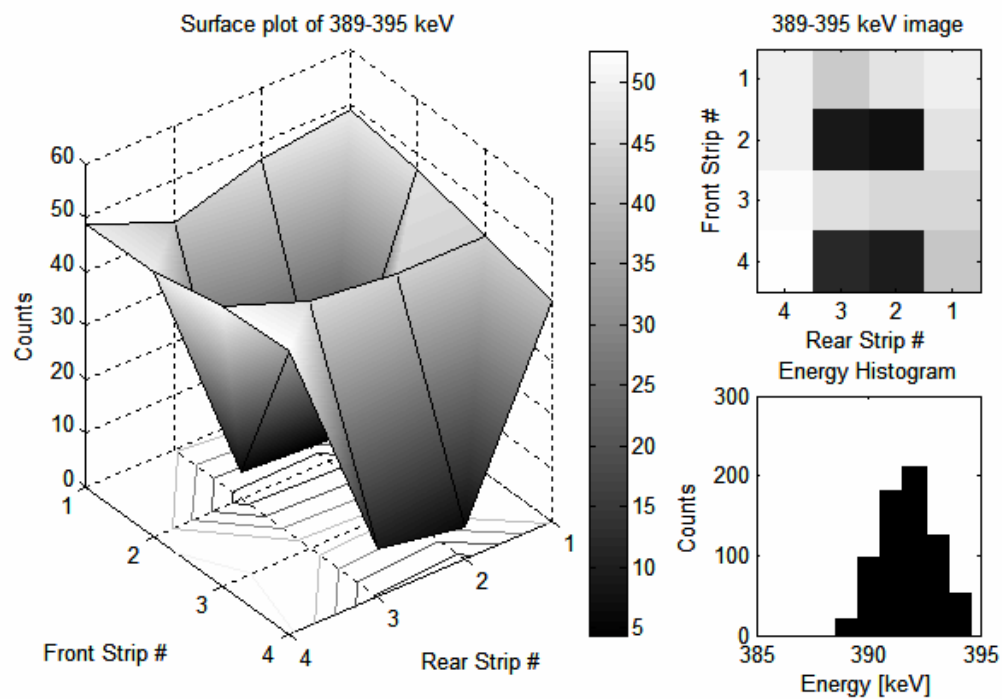


Figure 47: Image results of distributed Sn source using a 389-395 keV energy window

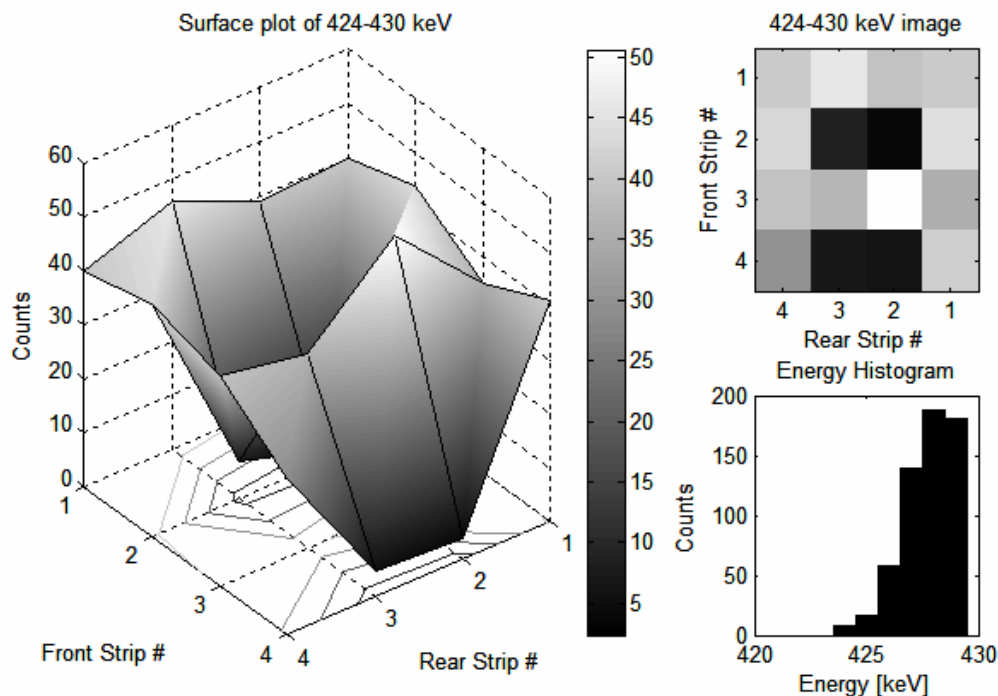


Figure 48: Image results of distributed Sn source using a 424-430 keV energy window

Close analysis of the three figures above shows that the best qualitative image contrast was actually achieved using only the 389-395 keV energy window. This may lead one to assume that you really only need to image in one energy window at a time. However, keep in mind that one major advantage in being able to image in multiple energy windows comes from the fact that weapon inspection times are limited, and that the flux of measurable gamma photons emitted through a weapon cask is quite small. Therefore, having the ability to combine counts from numerous peaks greatly increases the overall efficiency of the system. The image processing code could easily be updated to handle as many energy windows as desired.

Another way in which imaging across multiple energy windows can increase the efficiency of the system is by providing the ability to image multiple nuclides

simultaneously or individually using a single data set. The presence and physical orientation of multiple isotopes could provide information about the weapon design. However, some caution must be used when using multiple energy windows to image multiple nuclides. The key lies in the fact that the highest value recorded on the image is the highest count for any pixel within the specified energy windows. An example of this is shown in Figure 49. The image is of a Eu-152 point source in the bottom left corner and a Cs-137 point source near the top right corner imaged across the 341-347 keV (Eu-152) and 660-665 keV (Cs-137) energy windows.

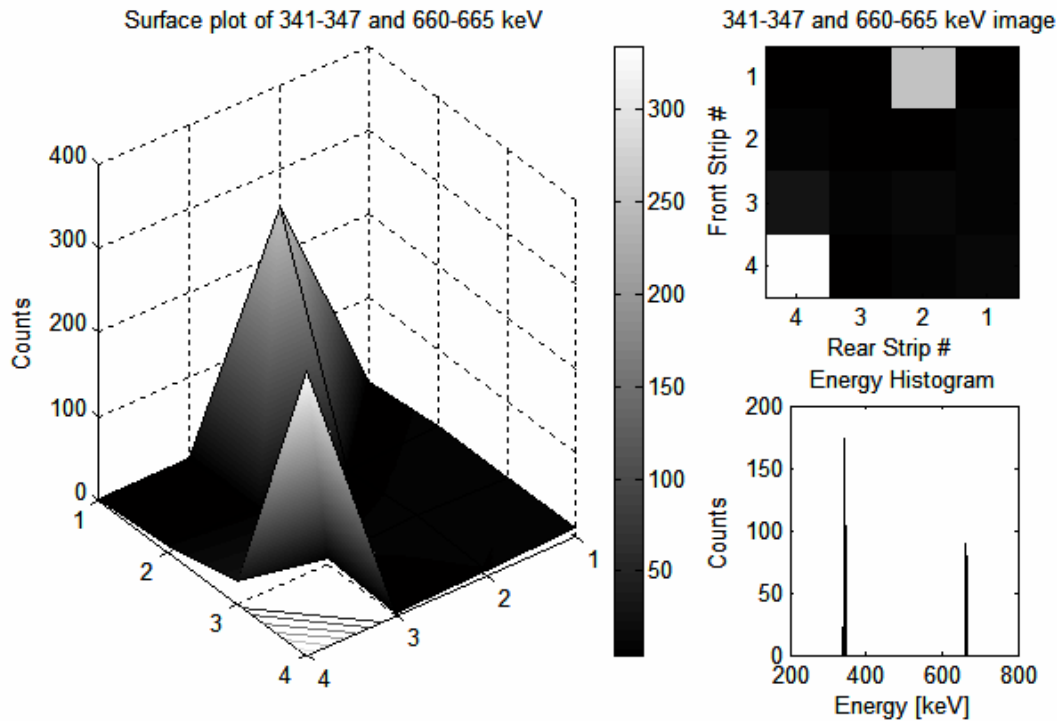


Figure 49: Two source image of Eu-152 and Cs-137 point sources

The higher activity of the Eu-152 source is evident by the higher number of counts recorded under the 341-347 keV window. Careful choices of the energy windows

clearly make visible the orientation of the two sources. However, it is not clear if the visible shapes consist of a mixture of the two nuclides or if they are in fact two separate sources. Additional images can be produced using the same data set with individual energy windows to ensure that in fact the two apparent sources are different nuclides and that the counts for a particular pixel is not from a mixture of the two nuclides. Figure 50 and Figure 51 show the resulting images using the energy windows for each source individually. The resulting image in Figure 50 is actually corrupted by higher energy Cs-137 gammas which are Compton scattered down into the energy window being viewed.

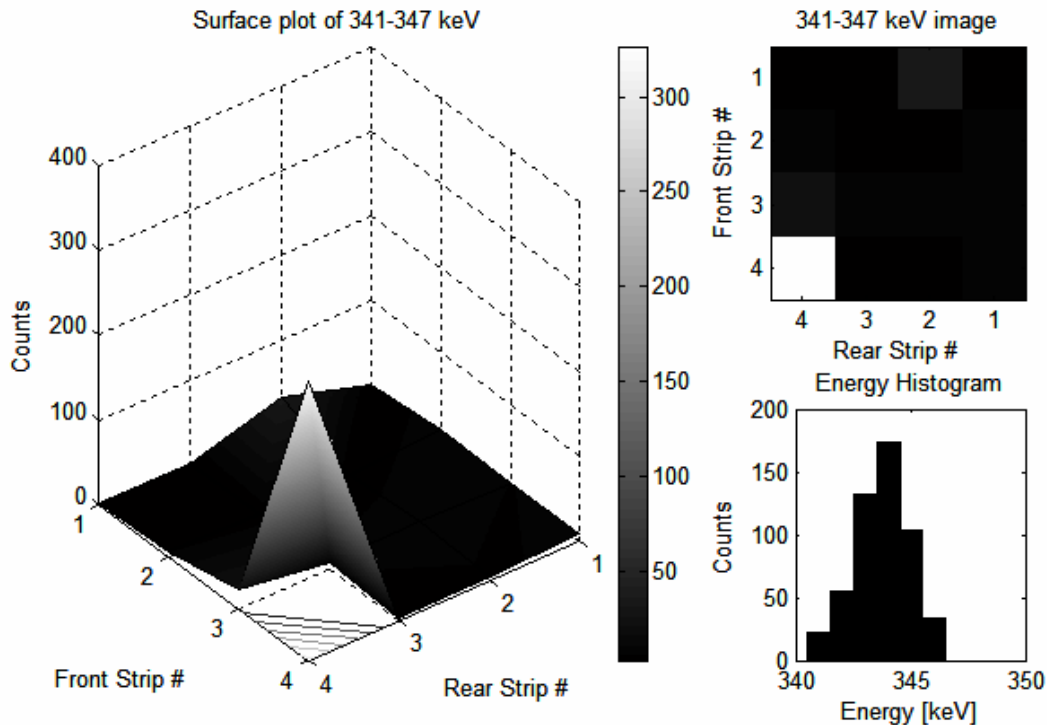


Figure 50: Two source image using 341-347 keV (Eu-152) energy window

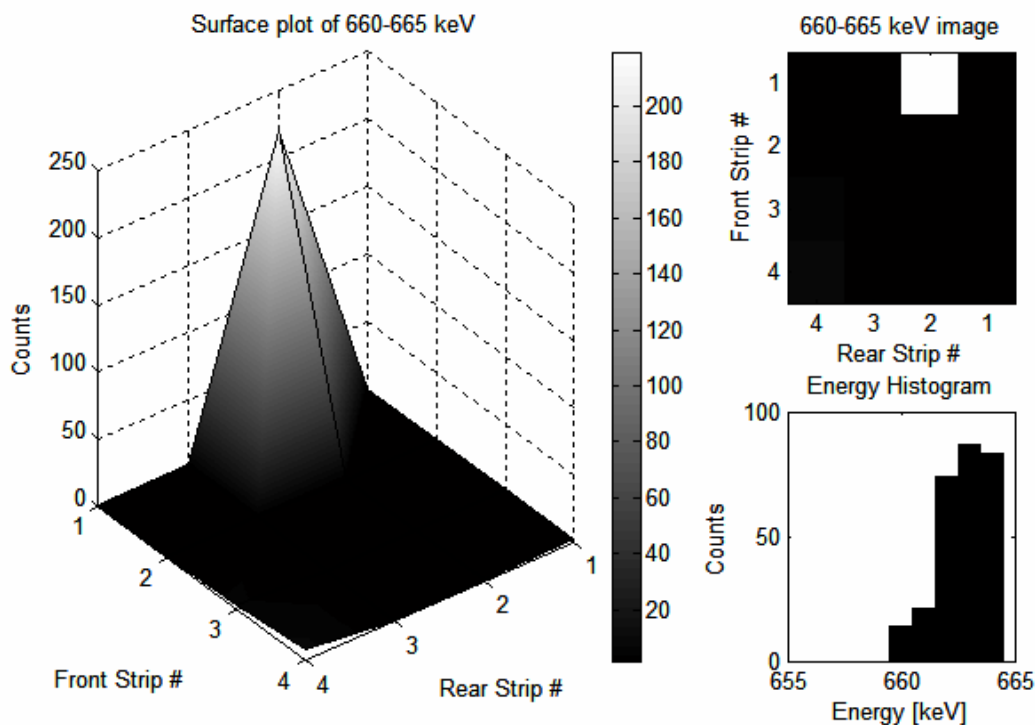


Figure 51: Two source image using 660-665 keV (Cs-137) energy window

Several other multi-nuclide images were developed during this work with results comparable to those presented above. This analysis resulted in a high degree of confidence of the use of multiple energy windows to identify multiple nuclides within a source image.

The ability of the system to distinguish a distributed source from a point source in a configuration consistent with that encountered during on site weapons inspections was tested using the pit simulation source described in Chapter 3 and a Eu-152 point source. Each source was placed 71 cm from the collimator along the center axis of the 4 by 4 pixel array used for imaging. Figure 52 shows the resulting image of the pit simulation source for a collection time of 14964 seconds. Although a circular symmetric image was

not obtained, it is still clear that the source is indeed distributed. The non-symmetric image could be a result of the source leakage discussed in Chapter 3.

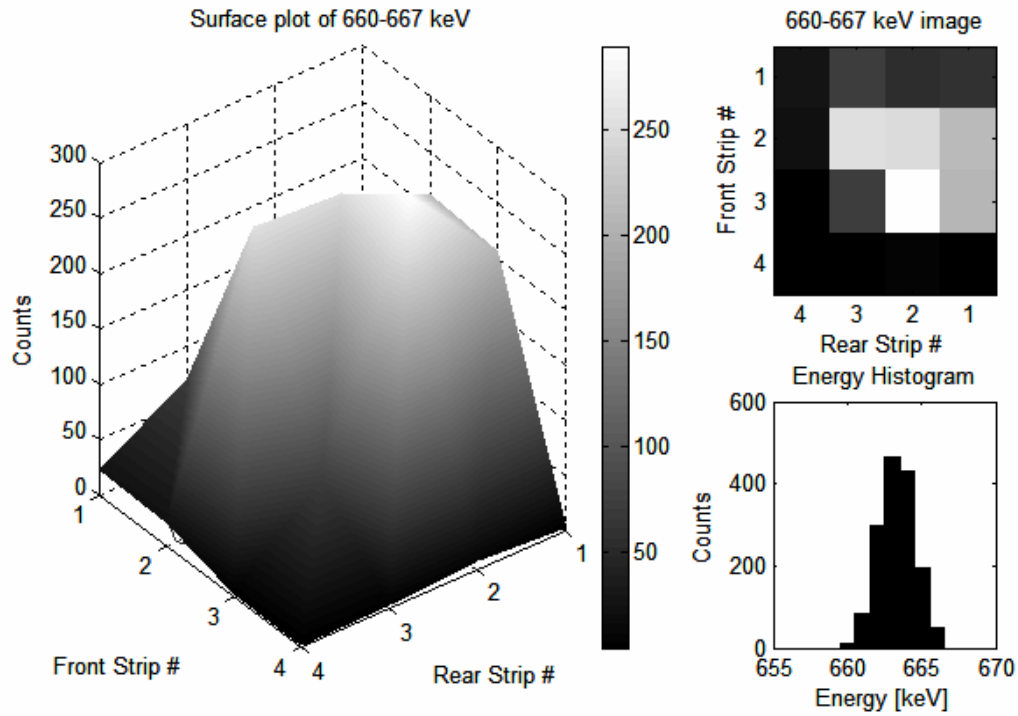


Figure 52: Image of Cs-137 pit simulation source 71 cm from detector

Figure 53 shows the image acquired from the Eu-152 source at a distance of 71 cm for a collection time of approximately 10 hours. Comparison of Figure 52 and Figure 53 clearly shows the ability of the system to distinguish a point source from a distributed source in a configuration consistent with that encountered during on site weapon inspections.

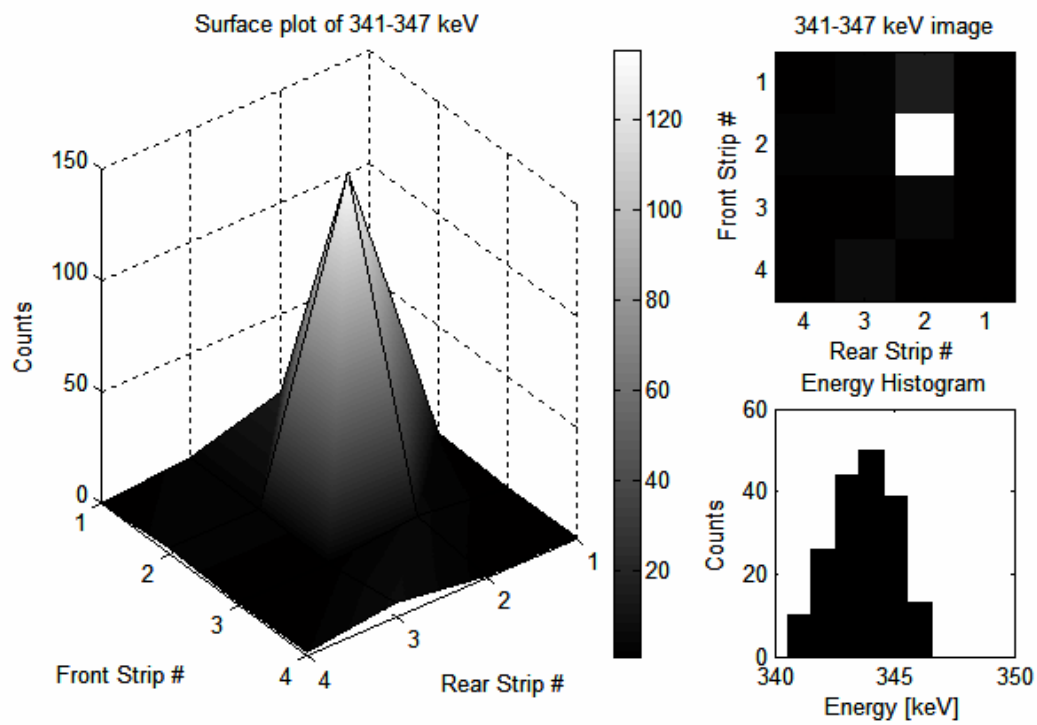


Figure 53: Image of Eu-152 source 71 cm from detector

VI. Conclusions and Recommendations

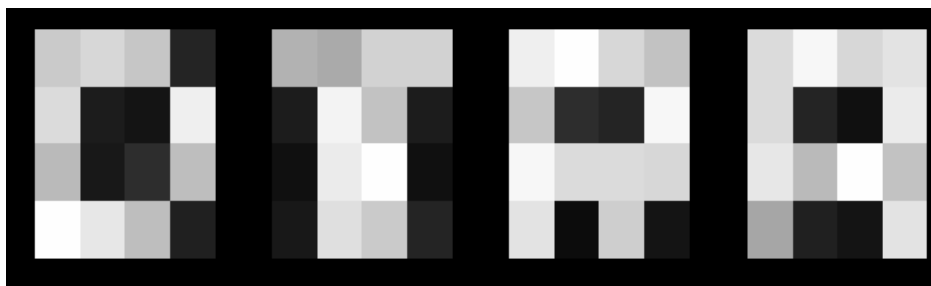


Figure 54: Combination of four images to spell DTRA

Figure 54 was created by combining four images that were produced by placing the activated Sn strip sources in a configuration that formed the letters D,T,R, and A. An example of the placement of the radiation sources for the “T” is shown in Figure 55.

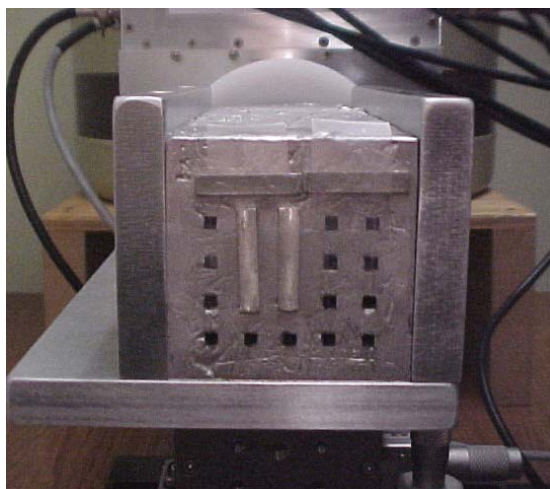


Figure 55: Source positioning for activated Sn strips to produce the DTRA “T”

Chapter Overview

The principle objective of this project was to develop an improved HPGe strip detector imaging system to help determine the basic size, shape and composition of SNM in a nuclear weapon pit. Key areas of interest included the performance of the detector,

performance of the input logic module, performance of the digital gamma finder modules, the application of a converging hole collimator, and application of a new image processing code.

Detector Performance

The performance of the detector was essentially what was expected for a high purity germanium detector. The resolution of the charge collecting strips was slightly poorer than a typical HPGe detector, but the efficiency measurements were in agreement with expectations for a detector of this size. The XIA module control software version 3.04 proved to be an improvement over version 3.02 which was used in previous work with this detector.

Resolution: The resolution measurements made using the XIA modules were consistently poorer (larger) than those quoted by ORTEC, the detector manufacturer. Table 11 shows the resolutions reported by the manufacturer, the measured resolutions using the XIA hardware with optimized and non-optimized settings, and the measured resolutions using the settings required for imaging. As mentioned in Chapter 4, the energy filter rise time had to be the same value for all charge collection strips in order to maintain a 100 ns coincidence window for imaging. This explains why the imaging settings provided optimum resolution for only two strips, R1 and R2. Further investigation is needed to determine if different module settings can be used to truly optimize the resolution of all detector strips at the same time while not sacrificing the length of the coincidence window.

Table 11: Detector FWHM measurements

| Strip | Manufacturer Reported FWHM (122 keV) | XIA Optimized Settings (635 keV) | XIA Non-optimized Settings (635 keV) | Imaging Settings (635 keV) |
|-------|---|---|---|-------------------------------|
| F1 | 1.64 | 2.53 | 3.08 | 2.76 |
| F2 | 1.62 | 2.47 | 3.07 | 2.78 |
| F3 | 1.23 | 2.11 | 2.80 | 2.55 |
| F4 | 1.31 | 2.31 | 2.53 | 2.41 |
| R1 | 1.48 | 2.44 | 2.61 | 2.44 |
| R2 | 1.50 | 2.81 | 3.37 | 2.81 |
| R3 | 1.41 | 2.25 | 2.65 | 2.56 |
| R4 | 1.40 | 2.24 | 2.79 | 2.76 |

Efficiency: The NRL has a 45mm x 45mm x 10mm germanium strip detector, with an efficiency of 2% at 662 keV. The detector efficiency calculated during this work for a 25mm x 25mm x 9mm germanium strip detector was 1.0875% at 662 keV.

Considering the difference in detector thickness as viewed from the source, the results from this work agree well. Also the plot of efficiency as a function of energy, shown in Figure 36, followed the expected trend of decreasing efficiency with increasing gamma energy.

Input Logic Module Performance

The inability to start and stop DGF modules at the same time during previous research with this system was overcome by the addition of the ORTEC input logic module. The input logic module provided the appropriate signal to start and stop both modules at the same time. This was evident by the ability to accurately pair together

events coincident in both time and energy which occurred after both modules were stopped and restarted by the input logic module.

Digital Gamma Finder Module Performance

The DGF modules proved to be quite effective for this work. The ability to change settings for individual strips and individual modules was crucial to optimizing the system. Being able to analyze data using the DGF controlling software greatly reduced the amount of time required to analyze data and make any necessary adjustments. The biggest shortfall of the modules is the inability to download information in real time.

Collimator Performance

The converging hole collimator designed and built for this research effectively collimated all sources used for imaging. While imaging point sources, the resulting images had relatively very few counts recorded in outlying pixels which were not illuminated by the sources. As expected, while imaging the distributed sources, more events were recorded in the outlying pixels than with the point sources. However, the collimation was sufficient to produce images with good contrast between illuminated and non-illuminated pixels.

The collimator was designed to provide the ability to image sources up to a 5 cm square shape at a distance of 71 cm. This ability was demonstrated by the use of the pit simulation source.

Imaging Performance

The images produced during this work met all expectations of being able to distinguish a point source from a distributed source. The combination of the new image processing code and the converging collimator made it possible to distinguish a point source from a distributed source even in a configuration consistent with those encountered during on site weapon inspections. The new image processing code also provided the ability to image across multiple energy windows. This allows the user to produce a viable image in shorter time by adding together the counts within multiple energy windows for a single source nuclide. It also provides the ability to obtain information about the relative position of multiple nuclides within the source region.

An additional improvement of the image processing code was the decrease in the amount of time to process a single image. The previous code required several hours to produce an image across a single energy window. The new code can process an image across two energy windows in approximately 30 seconds. This greatly reduces the amount of time required for image analysis.

Recommendations for Future Work

The current XIA software does not allow data to be downloaded to the host computer until the entire data set has been collected. It would have been extremely helpful if the data could have been transferred to the host computer at near real time. This would have allowed an image to be built up over time and the operator could determine when enough data had been collected. Currently, an estimate of the time

required must be made and the data collected followed by image processing to determine if there was indeed enough time.

Because of limitations on the number of inputs for each DGF module, only a 4 by 4 pixel image was produced. Although this was sufficient to distinguish a point source from a distributed source, the addition of a third DGF module, along with some basic updates to the image processing code, would make it possible to produce a 5 by 5 pixel image with the collimator built for this work. More image pixels over the same area would theoretically allow one to obtain better shape information.

A more important contribution which can be made to this project is developing the ability to get sub pixel resolution for the charge collecting strips. The idea of using edge pixel collimator holes proved to be inefficient at high photon energies. However, according to the Navy Research Lab [8], it is possible to determine which portion of the charge collecting strip actually collected the charge by viewing the induced noise of the two strips adjacent to the one that collected the charge. This would allow an image array of 10 x 10, if the position could be determined within 2.5 mm. The advantage to processing the data in this way to increase the resolution as opposed to simply creating a strip detector with 10 strips on each side is that the increase in hardware is minimal with this method, and if the system is to be used for treaty monitoring, portability is a concern and hardware must be minimized.

Summary

The ability to use an HPGeDSSD coupled with a converging hole collimator as an imaging device to detect spoof weapons has been demonstrated. Although the spatial

resolution of the detector could not be improved using edge hole pixels, the current spatial resolution proved to be sufficient for distinguishing a point source from a distributed source. The use of a converging collimator provided the ability to image a source that was larger than the detector in a configuration consistent with that encountered during on site weapon inspections. The addition of an input logic module, combined with a new image processing code, made it possible to acquire and process three strip events for imaging. The new image processing code also provided the ability to simultaneously identify multiple nuclides by imaging across multiple energy windows. In addition, this was all made possible while greatly reducing the time required for processing an image.

Appendix A. Collimator Design Code

Graphics'Graphics'

Collimator design code

Purpose: This code is used to help design effective collimators for imaging special nuclear material using a HPGe Double Sided Strip Detector with a 5 x 5 array of 5 x 25 mm strips.

CPT Doug Rothenbush

Version 1.0

6Dec04

All measurements are in [mm] unless noted.

Input parameters

holewidth=2.9;

collimatorthickness=190;

focallength=1160;

caskradius=710;

Find slope of centerlines

$$\text{lineslope}[1] = \frac{50.}{\text{focallength}}$$

$$\text{angle}[1] = \text{ArcTan}[\text{lineslope}[1]] * \frac{180}{\pi};$$

$$\text{lineslope}[2] = \frac{25.}{\text{focallength}}$$

$$\text{angle}[2] = \text{ArcTan}[\text{lineslope}[2]] * \frac{180}{\pi};$$

$$\text{lineslope}[3] = 0$$

$$\text{angle}[3] = 0;$$

0.0431034

0.0215517

0

Determine critical locations

sourceface=focallength-caskradius (* collimator must be atleast the cask radius from the source *)

450

detface=sourceface-collimatorthickness

260

$$\text{crystalcenter} = \frac{10}{\text{lineslope}[1]}$$

232.

detectorhousing=crystalcenter+19.5 (* must be less than detface *)

251.5

Compute the y value of the centerlines at the collimator source face (inside face of source endplate) [mm]

Do[sourcecenter[n]=sourceface*lineslope[n],{n,1,3}]

sourcecenter[1]

sourcecenter[2]

sourcecenter[3]

```

19.3966
9.69828
0
Convert to inches
Do[sourcecenterinches[n]=sourcecenter[n]/25.4,{n,1,3}]
sourcecenterinches[1]
sourcecenterinches[2]
sourcecenterinches[3]
0.763644
0.381822
0
Compute the y value of the centerlines at the outside face of source endplate[mm]
Do[outsidecenter[n]=(sourceface+6.35)*lineslope[n],{n,1,3}]
outsidecenter[1]
outsidecenter[2]
outsidecenter[3]
19.6703
9.83513
0
Convert to inches
Do[outsidecenterinches[n]=outsidecenter[n]/25.4,{n,1,3}]
outsidecenterinches[1]
outsidecenterinches[2]
outsidecenterinches[3]
0.77442
0.38721
0
Compute the y value of the centerlines at the collimator detector face (inside face of
detector endplate) [mm]
Do[detcenter[n]=detface*lineslope[n],{n,1,3}]
detcenter[1]
detcenter[2]
detcenter[3]
11.2069
5.60345
0
Convert to inches
Do[detcenterinches[n]=detcenter[n]/25.4,{n,1,3}]
detcenterinches[1]
detcenterinches[2]
detcenterinches[3]
0.441216
0.220608
0
Compute the y value of the centerlines at the outside face of detector endplate[mm]

```

```

Do[outsidedetcenter[n]=(detface-6.35)*lineslope[n],{n,1,3}]
outsidedetcenter[1]
outsidedetcenter[2]
outsidedetcenter[3]
10.9332
5.46659
0
Convert to inches
Do[outsidedetcenterinches[n]=outsidedetcenter[n]/25.4,{n,1,3}]
outsidedetcenterinches[1]
outsidedetcenterinches[2]
outsidedetcenterinches[3]
0.430441
0.21522
0
Find the width of the holes at the collimator faces and endplate faces

$$\Delta y[1] = \frac{.5 * \text{holewidth}}{\text{Cos}[\text{ArcTan}[\text{lineslope}[1]]]}$$


$$\Delta y[2] = \frac{.5 * \text{holewidth}}{\text{Cos}[\text{ArcTan}[\text{lineslope}[2]]]}$$


$$\Delta y[3] = .5 * \text{holewidth}$$

1.45135
1.45034
1.45
Convert to inches
□yinches[1] = □y[1]/25.4
□yinches[2] = □y[2]/25.4
□yinches[3] = □y[3]/25.4
0.0571396
0.0570999
0.0570866
Find y value for top of holes on the source side (inside of source endplate)
Do[topsource[n]=sourcecenter[n]+□y[n],{n,1,3}];
topsource[1]
topsource[2]
topsource[3]
20.8479
11.1486
1.45
Convert to inches
Do[topsourceinches[n]=topsource[n]/25.4,{n,1,3}];
topsourceinches[1]
topsourceinches[2]
topsourceinches[3]
0.820783

```

```

0.438922
0.0570866
Find y value for bottom of holes on the source side (inside of source endplate)
Do[bottomsource[n]=sourcecenter[n]-□y[n],{n,1,3}];
bottomsource[1]
bottomsource[2]
bottomsource[3]
17.9452
8.24794
-1.45
Convert to inches
Do[bottomsourceinches[n]=bottomsource[n]/25.4,{n,1,3}];
bottomsourceinches[1]
bottomsourceinches[2]
bottomsourceinches[3]
0.706504
0.324722
-0.0570866
Find y value for top of holes on the outside of source endplate
Do[topoutsidesource[n]=outsidesourcecenter[n]+□y[n],{n,1,3}];
topoutsidesource[1]
topoutsidesource[2]
topoutsidesource[3]
21.1216
11.2855
1.45
Convert to inches
Do[topoutsidesourceinches[n]=topoutsidesource[n]/25.4,{n,1,3}];
topoutsidesourceinches[1]
topoutsidesourceinches[2]
topoutsidesourceinches[3]
0.831559
0.44431
0.0570866
Find y value for bottom of holes on the outside of source endplate
Do[bottomoutsidesource[n]=outsidesourcecenter[n]-□y[n],{n,1,3}];
bottomoutsidesource[1]
bottomoutsidesource[2]
bottomoutsidesource[3]
18.2189
8.38479
-1.45
Convert to inches
Do[bottomoutsidesourceinches[n]=bottomoutsidesource[n]/25.4,{n,1,3}];
bottomoutsidesourceinches[1]

```

```

bottomoutsidesourceinches[2]
bottomoutsidesourceinches[3]
0.71728
0.33011
-0.0570866
Find y value for top of holes on the detector side (inside of detector endplate)
Do[topdet[n]=detcenter[n]+□y[n],{n,1,3}]
topdet[1]
topdet[2]
topdet[3]
12.6582
7.05378
1.45
Convert to inches
Do[topdetinches[n]=topdet[n]/25.4,{n,1,3}]
topdetinches[1]
topdetinches[2]
topdetinches[3]
0.498356
0.277708
0.0570866
Find y value for bottom of holes on the detector side (inside of detector endplate)
Do[bottomdet[n]=detcenter[n]-□y[n],{n,1,3}]
bottomdet[1]
bottomdet[2]
bottomdet[3]
9.75555
4.15311
-1.45
Convert to inches
Do[bottomdetinches[n]=bottomdet[n]/25.4,{n,1,3}]
bottomdetinches[1]
bottomdetinches[2]
bottomdetinches[3]
0.384077
0.163508
-0.0570866
Find y value for top of holes on the outside of detector endplate
Do[topoutsidedet[n]=outsidedetcenter[n]+□y[n],{n,1,3}]
topoutsidedet[1]
topoutsidedet[2]
topoutsidedet[3]
12.3845
6.91693
1.45

```

Convert to inches

Do[topoutsidedet[inches][n]=topoutsidedet[n]/25.4,{n,1,3}]

topoutsidedet[inches][1]

topoutsidedet[inches][2]

topoutsidedet[inches][3]

0.48758

0.27232

0.0570866

Find y value for bottom of holes on the outside of detector endplate

Do[bottomoutsidedet[n]=outsidedetcenter[n]-y[n],{n,1,3}]

bottomoutsidedet[1]

bottomoutsidedet[2]

bottomoutsidedet[3]

9.48184

4.01626

-1.45

Convert to inches

Do[bottomoutsidedet[inches][n]=bottomoutsidedet[n]/25.4,{n,1,3}]

bottomoutsidedet[inches][1]

bottomoutsidedet[inches][2]

bottomoutsidedet[inches][3]

0.373301

0.15812

-0.0570866

Find the equations for the field of view lines and the centerlines

Do[lineA[n, x_] = $\left(\frac{\text{bottomsource}[n] - \text{topdet}[n]}{\text{collimatorthickness}} \right) \times (x - \text{detface}) + \text{topdet}[n];$

lineB[n, x_] = $\left(\frac{\text{topsource}[n] - \text{bottomdet}[n]}{\text{collimatorthickness}} \right) \times (x - \text{detface}) + \text{bottomdet}[n];$ centerline[n, x_] = lineslope[n] * x;

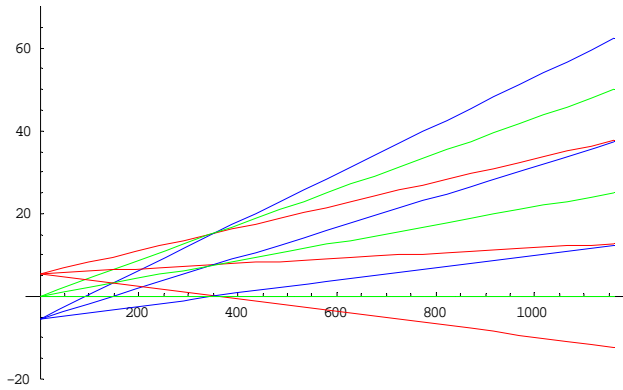
topline[n, x_] = $\left(\frac{\text{topsource}[n] - \text{topdet}[n]}{\text{collimatorthickness}} \right) \times (x - \text{detface}) + \text{topdet}[n];$

bottomline[n, x_] = $\left(\frac{\text{bottomsource}[n] - \text{bottomdet}[n]}{\text{collimatorthickness}} \right) \times (x - \text{detface}) + \text{bottomdet}[n], \{n, 1, 3\}]$

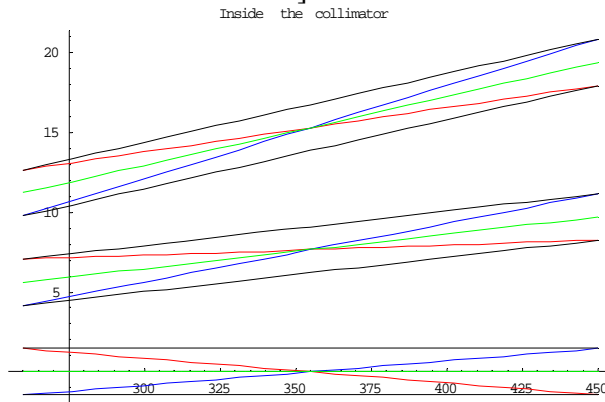
Plot field of view and centerlines

Plot[{lineA[1,x],lineB[1,x],centerline[1,x],lineA[2,x],lineB[2,x],centerline[2,x],lineA[3,x],lineB[3,x],centerline[3,x]},{x,0,focallength},PlotStyle->{{RGBColor[1,0,0]},RGBColor[0,0,1]},{RGBColor[0,1,0]}},PlotRange->{-20,70}]

(*PlotLegend->{"line A1","line B1","centerline1","line A2","line B2","centerline2","line A3","line B3","centerline3"},LegendPosition->{-1.5,-.1},LegendSize->{.4,.8}*)



Plot[{lineA[1,x],lineB[1,x],centerline[1,x],topline[1,x],bottomline[1,x],lineA[2,x],lineB[2,x],centerline[2,x],topline[2,x],bottomline[2,x],lineA[3,x],lineB[3,x],centerline[3,x],topline[3,x],bottomline[3,x]}, {x,detface,sourceface},PlotStyle[{{RGBColor[1,0,0]},RGBColor[0,0,1]}, {RGBColor[0,1,0]}, {RGBColor[0,0,0]}],PlotLabel ->"Inside the collimator"]



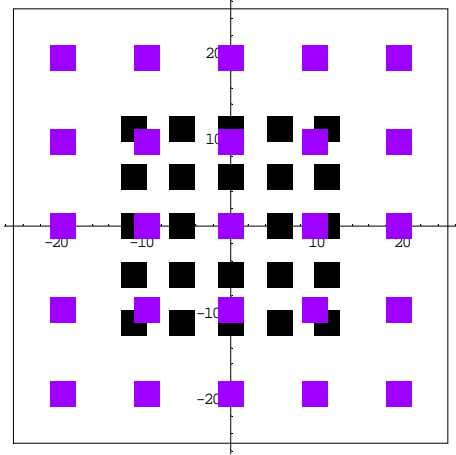
Plot holes on the collimator front and back faces

```
ColFrontHoles1=Table[Graphics[Rectangle[{lineB[n,sourceface],lineB[t,sourceface]}, {lineA[n,sourceface],lineA[t,sourceface]}]], {n,1,3}, {t,1,3}];
ColBackHoles1=Table[Graphics[Rectangle[{lineB[n,detface],lineB[t,detface]}, {lineA[n,detface],lineA[t,detface]}]], {n,1,3}, {t,1,3}];
ColFrontHoles2=Table[Graphics[Rectangle[{-lineA[n,sourceface],lineB[t,sourceface]}, {-lineB[n,sourceface],lineA[t,sourceface]}]], {n,1,3}, {t,1,3}];
ColBackHoles2=Table[Graphics[Rectangle[{-lineA[n,detface],lineB[t,detface]}, {-lineB[n,detface],lineA[t,detface]}]], {n,1,3}, {t,1,3}];
ColFrontHoles3=Table[Graphics[Rectangle[{-lineA[n,sourceface],-lineA[t,sourceface]}, {-lineB[n,sourceface],-lineB[t,sourceface]}]], {n,1,3}, {t,1,3}];
ColBackHoles3=Table[Graphics[Rectangle[{-lineA[n,detface],-lineA[t,detface]}, {-lineB[n,detface],-lineB[t,detface]}]], {n,1,3}, {t,1,3}];
ColFrontHoles4=Table[Graphics[Rectangle[{lineB[n,sourceface],-lineA[t,sourceface]}, {lineA[n,sourceface],-lineB[t,sourceface]}]], {n,1,3}, {t,1,3}];
```

```

ColBackHoles4=Table[Graphics[Rectangle[{lineB[n,detface],-
lineA[t,detface]},{lineA[n,detface],-lineB[t,detface]}]],{n,1,3},{t,1,3}];
Colors2=Graphics[Hue[.77]];
BackFace=Table[Graphics[Line[{{-15,-15},{-15,15},{15,15},{15,-15},{-15,-15}}]]];
FrontFace=Table[Graphics[Line[{{-25,-25},{-25,25},{25,25},{25,-25},{-25,-25}}]]];
Show[ColBackHoles1,ColBackHoles2,ColBackHoles3,ColBackHoles4,FrontFace,Colors
2,ColFrontHoles1,ColFrontHoles2, ColFrontHoles3, ColFrontHoles4,AspectRatio-
>Automatic,Axes True]

```



Plot fields of view on the detector front and back faces

```

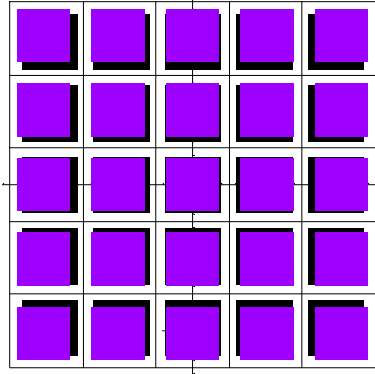
FrontHoles1=Table[Graphics[Rectangle[{lineA[n,crystalcenter+4.5],lineA[t,crystalcenter
+4.5]},{lineB[n,crystalcenter+4.5],lineB[t,crystalcenter+4.5]}]],{n,1,3},{t,1,3}];
BackHoles1=Table[Graphics[Rectangle[{lineA[n,crystalcenter-4.5],lineA[t,crystalcenter-
4.5]},{lineB[n,crystalcenter-4.5],lineB[t,crystalcenter-4.5]}]],{n,1,3},{t,1,3}];
FrontHoles2=Table[Graphics[Rectangle[{-
lineB[n,crystalcenter+4.5],lineA[t,crystalcenter+4.5]},{-
lineA[n,crystalcenter+4.5],lineB[t,crystalcenter+4.5]}]],{n,1,2},{t,1,3}];
BackHoles2=Table[Graphics[Rectangle[{-lineB[n,crystalcenter-
4.5],lineA[t,crystalcenter-4.5]},{-lineA[n,crystalcenter-4.5],lineB[t,crystalcenter-
4.5]}]],{n,1,2},{t,1,3}];
FrontHoles3=Table[Graphics[Rectangle[{-lineB[n,crystalcenter+4.5],-
lineA[t,crystalcenter+4.5]},{-lineA[n,crystalcenter+4.5],-
lineB[t,crystalcenter+4.5]}]],{n,1,3},{t,1,2}];
BackHoles3=Table[Graphics[Rectangle[{-lineB[n,crystalcenter-4.5],-
lineA[t,crystalcenter-4.5]},{-lineA[n,crystalcenter-4.5],-lineB[t,crystalcenter-
4.5]}]],{n,1,3},{t,1,2}];
FrontHoles4=Table[Graphics[Rectangle[{lineA[n,crystalcenter+4.5],-
lineB[t,crystalcenter+4.5]},{lineB[n,crystalcenter+4.5],-
lineA[t,crystalcenter+4.5]}]],{n,1,2},{t,1,2}];
BackHoles4=Table[Graphics[Rectangle[{lineA[n,crystalcenter-4.5],-
lineB[t,crystalcenter-4.5]},{lineB[n,crystalcenter-4.5],-lineA[t,crystalcenter-
4.5]}]],{n,1,2},{t,1,2}];

```

```

Colors1=Graphics[Hue[.77]];
BackStrips=Table[Graphics[Line[{{n,-12.5},{n,12.5}}]],{n,-12.5,12.5,5}];
FrontStrips=Table[Graphics[Line[{{-12.5,n},{12.5,n}}]],{n,-12.5,12.5,5}];
Show[BackHoles1,BackHoles2,BackHoles3,BackHoles4,BackStrips,FrontStrips,Colors1,
FrontHoles1,FrontHoles2,FrontHoles3,FrontHoles4,AspectRatio->Automatic,Axes True]

```

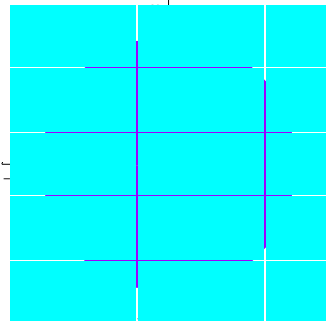


Plot fields of view on the source

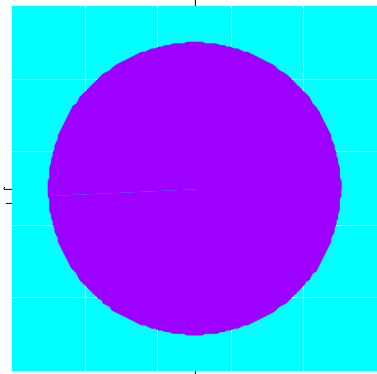
```

SourceHoles1=Table[Graphics[Rectangle[{lineB[n,focallength],lineB[t,focallength]},{lineA[n,focallength],lineA[t,focallength]}]],{n,1,3},{t,1,3}];
SourceHoles2=Table[Graphics[Rectangle[{-lineA[n,focallength],lineB[t,focallength]},{-lineB[n,focallength],lineA[t,focallength]}]],{n,1,3},{t,1,3}];
SourceHoles3=Table[Graphics[Rectangle[{-lineA[n,focallength],-lineA[t,focallength]},{-lineB[n,focallength],-lineB[t,focallength]}]],{n,1,3},{t,1,3}];
SourceHoles4=Table[Graphics[Rectangle[{lineB[n,focallength],-lineA[t,focallength]},{lineA[n,focallength],-lineB[t,focallength]}]],{n,1,3},{t,1,3}];
Source=Graphics[Disk[{0,0},50]];
Colors3=Graphics[Hue[.77]];
Colors4=Graphics[Hue[.5]];
Show[Colors3,Source,Colors4,SourceHoles1,SourceHoles2,SourceHoles3,SourceHoles4,
AspectRatio->Automatic,Axes True]
Show[Colors4,SourceHoles1,SourceHoles2,SourceHoles3,SourceHoles4,Colors3,Source,
AspectRatio->Automatic,Axes True]

```



□ Graphics □



□ Graphics □

Appendix B. Image Processing Code

```
% HPGe Double Sided Strip Detector Imaging code
% CPT Doug Rothenbush
% Version 1.0 31Dec04
% This code takes a text file of data from a HPGe DSSD and
% converts it into an image of the source. The data is taken from two
% DGF-4C modules. Module 1 has four rear strips, and module 2 has four
% front strips.
%
% Code outline
% 1. Read in raw data and user inputs
% 2. Sort the data into separate matrices for each module
% 3. Compare each module 1 event with those in module 2 to find a
% two strip event coincident in time and energy.
% 4. Determine which pixel received the hit and add 1 to its image value.
% 5. Compare each module 1 coincident event with those in module 2 to find a
% three strip event coincident in time and energy.
% 6. Determine which pixel received the hit (earliest timestamp)and add 1 to its image
% value.
% 7. Compare each module 2 coincident event with those in module 1 to find a
% three strip event coincident in time and energy.
% 8. Determine which pixel received the hit (earliest timestamp)and add 1 to its image
% value.
% 9. Display the image along with a surface plot and a histogram of hits.
% module 1 are rear strips
% module 2 are front strips
% 1. Read in the raw data and user inputs
clear % clear workspace
load 'data.txt';
windows = input('How many energy windows would you like to image, 1 or 2?')
lower_limit2 = 0;
upper_limit2 = 0;
if windows == 2
    lower_limit = input('What is the lower limit of your first imaging window in keV?')
    upper_limit = input('What is the upper limit of your first imaging window in keV?')
    lower_limit2 = input('What is the lower limit of your second imaging window in
keV?')
    upper_limit2 = input('What is the upper limit of your second imaging window in
keV?')
    range_upper_limit = upper_limit2;
else
    lower_limit = input('What is the lower limit of your imaging window in keV?')
    upper_limit = input('What is the upper limit of your imaging window in keV?')
    range_upper_limit = upper_limit;
```

```

end
three_strip_use = input('Would you like to use three strip events? (1) Yes (2) No
(Default is yes)')
disp('Calibration is of the form energy = (channel # - a)/b')
disp('Currently a = -20.2 and b = 38.852')
keep_cal = input('Is this the calibration you want to use? (1)yes (2)no')
if keep_cal == 2
    a = input('Enter your new value for a?')
    b = input('Enter your new value for b?')
else
    a = 85;
    b = 38.634;
end
threshold = b * lower_limit + a;
threshold_max = b * upper_limit + a;
threshold2 = b * lower_limit2 + a;
threshold_max2 = b * upper_limit2 + a;
% initialize image matrices
two_strip_image = zeros(4,4);
three_strip_image = zeros(4,4);
full_image=zeros(4,4);
% Define time and energy window to define a hit
deltatime=10;
deltaenergy=200;
j=1;
spill_size = data(j,1);
mod1 = [];
mod2 = [];
totalheader=[];
coinc_data1 = [];
coinc_data2 = [];
hit_hist=[];
% pull out first header
header = data(j:j+5,1);
totalheader= [totalheader header];
% jump to first hit pattern
j=7;
hit_patt=data(j,1);
mod=header(2,1);
while mod > 0
    % 2. Sort data
    while (j < spill_size)
        % find coincident events for module 1 and put into coinc_data1 matrix
        if ( hit_patt == 3) | (hit_patt == 6 ) % 3 = 0011 6 = 0110
            coinc_event = data(j:(j+6),1);

```

```

    coinc_energy = coinc_event(5,1) + coinc_event(7,1);
    if ((coinc_energy > threshold) & (coinc_energy < threshold_max)) | ((coinc_energy >
threshold2) & (coinc_energy < threshold_max2))
        if mod==1
            coinc_data1 = [coinc_data1 coinc_event];
        elseif mod==2
            coinc_data2 = [coinc_data2 coinc_event];
        end
    end
    j=j+7;
elseif ( hit_patt == 12 ) % 12 = 1100
    coinc_event = data(j:(j+6),1);
    coinc_energy = coinc_event(5,1) + coinc_event(7,1);
    if ((coinc_energy > threshold) & (coinc_energy < threshold_max)) | ((coinc_energy >
threshold2) & (coinc_energy < threshold_max2))
        if mod==1
            coinc_data1 = [coinc_data1 coinc_event];
        elseif mod==2
            coinc_data2 = [coinc_data2 coinc_event];
        end
    end
    j=j+7;
else
    event = data(j:j+4,1);
    if ((event(5,1) > threshold) & (event(5,1) < threshold_max)) | ((event(5,1) >
threshold2) & (event(5,1) < threshold_max2))
        if mod==1
            mod1 = [mod1 event];
        elseif mod==2
            mod2 = [mod2 event];
        end
    end
    j=j+5;
end
hit_patt = data(j,1);
end
header=data(j:j+5,1);
totalheader=[totalheader header];
spill_size = spill_size + header(1,1);
mod=header(2,1);
% jump past the header
j=j+6;
hit_patt=data(j,1);
end
disp('Sorting is now complete')

```

```

% module data are now separated and ready to be compared
% 3. Determine two strip events
[mod1_rows,mod1_col] = size(mod1);
[mod2_rows , mod2_col] = size(mod2);
minm=1;
for n = 1:mod1_col
    for m = minm:mod2_col
        % find if event time hi words are equal
        if (mod1(2,n)==mod2(2,m))
            % find if fast trigger times are within deltatime
            if (abs(mod1(4,n) - mod2(4,m)) < deltatime)
                % if energies are within deltaenergy we have a two
                % strip hit
                if (abs(mod1(5,n) - mod2(5,m)) < deltaenergy)
                    hit_energy = (mod2(5,m)-a)/b;
                    hit_hist = [hit_hist hit_energy];
                    % 4. Determine which pixel gets the hit and add 1 to
                    % its image value
                    r=[];
                    f=[];
                    % determine which rear strip got hit
                    if (mod1(1,n)==1)
                        r=1;
                    elseif (mod1(1,n)==2)
                        r=2;
                    elseif (mod1(1,n)==4)
                        r=3;
                    elseif (mod1(1,n)==8)
                        r=4;
                    end
                    % determine which front strip got hit
                    if (mod2(1,m)==1)
                        f=1;
                    elseif (mod2(1,m)==2)
                        f=2;
                    elseif (mod2(1,m)==4)
                        f=3;
                    elseif (mod2(1,m)==8)
                        f=4;
                    end
                    % add hit count to image at (f,r)
                    two_strip_image(f,r)=two_strip_image(f,r) + 1;
                    minm=m;
                    m=mod2_col;
                end
            end
        end
    end
end

```



```

        end
    end
end
two_strip_hits=sum(sum(two_strip_image))
% end of two strip event section
% compute 3 strip events
% 5. Compare each module 1 coincident event with those in module 2 to find a
% three strip event coincident in time and energy.
[coinc_data1_rows,coinc_data1_col] = size(coinc_data1);
for n = 1:coinc_data1_col
    for m = 1:mod2_col
        % see if sum of coincident energies are above the energy threshold
        coinc_energy = coinc_data1(5,n)+ coinc_data1(7,n);
        % find if event time hi words are equal
        if (coinc_data1(2,n)==mod2(2,m))
            % find if fast trigger times are within deltatime
            if (abs(coinc_data1(4,n) - mod2(4,m)) < deltatime)
                % if energies are within deltaenergy we have a two
                % strip hit
                if (abs(coinc_energy - mod2(5,m)) < deltaenergy)
                    hit_energy = (mod2(5,m)-a)/b;
                    hit_hist = [hit_hist hit_energy];
                    % 6. Determine which pixels received the hit and add 0.5 to their image
                    % value.
                    r=[];
                    f=[];
                    % determine which rear strip got hit
                    if (coinc_data1(1,n)==3)
                        if coinc_data1(4,n)<coinc_data1(6,n)
                            r=1;
                        else
                            r=2;
                        end
                        %r1=1;
                        %r2=2;
                    elseif (coinc_data1(1,n)==6)
                        if coinc_data1(4,n)<coinc_data1(6,n)
                            r=2;
                        else
                            r=3;
                        end
                        %r1=2;
                        %r2=3;
                    else

```

```

        if coinc_data1(4,n)<coinc_data1(6,n)
            r=3;
        else
            r=4;
        end
        %r1=3;
        %r2=4;
    end
    % determine which front strip got hit
    if (mod2(1,m)==1)
        f=1;
    elseif (mod2(1,m)==2)
        f=2;
    elseif (mod2(1,m)==4)
        f=3;
    elseif (mod2(1,m)==8)
        f=4;
    end
    % add hit count to image at (f,r)
    three_strip_image(f,r)=three_strip_image(f,r) + 1;
    %three_strip_image(f,r2)=three_strip_image(f,r2) + 0.5;
end
end
end
end
end
% 7. Compare each module 2 coincident event with those in module 1 to find a
% three strip event coincident in time and energy.
[coinc_data2_rows,coinc_data2_col] = size(coinc_data2);
for n = 1:coinc_data2_col
    for m = 1:mod1_col
        % see if sum of coincident energies are above the energy threshold
        coinc_energy = coinc_data2(5,n)+ coinc_data2(7,n);
        % find if event time hi words are equal
        if (coinc_data2(2,n)==mod1(2,m))
            % find if fast trigger times are within deltatime
            if (abs(coinc_data2(4,n) - mod1(4,m)) < deltatime)
                % if energies are within deltaenergy we have a two
                % strip hit
                if (abs(coinc_energy - mod1(5,m)) < deltaenergy)
                    hit_energy = (mod1(5,m)-a)/b;
                    hit_hist = [hit_hist hit_energy];
                    % 8. Determine which pixels received the hit and add 0.5 to their image
                    % value.
                    r=[];

```

```

f1=[];
f2=[];
% determine which front strips got hit
if (coinc_data2(1,n)==3)
    if coinc_data2(4,n)<coinc_data2(6,n)
        f=1;
    else
        f=2;
    end
    %f1=1;
    %f2=2;
elseif (coinc_data2(1,n)==6)
    if coinc_data2(4,n)<coinc_data2(6,n)
        f=2;
    else
        f=3;
    end
    %f1=2;
    %f2=3;
else
    if coinc_data2(4,n)<coinc_data2(6,n)
        f=3;
    else
        f=4;
    end
    %f1=3;
    %f2=4;
end
% determine which rear strip got hit
if (mod1(1,m)==1)
    r=1;
elseif (mod1(1,m)==2)
    r=2;
elseif (mod1(1,m)==4)
    r=3;
elseif (mod1(1,m)==8)
    r=4;
end
% add hit count to image at (f,r)
three_strip_image(f,r)=three_strip_image(f,r) + 1;
%three_strip_image(f2,r)=three_strip_image(f2,r) + 0.5;
end
end
end
end
end

```

```

end
three_strip_hits=sum(sum(three_strip_image))
if three_strip_use == 2
    full_image = two_strip_image;
else
    full_image = two_strip_image + three_strip_image;
end
total_hits = sum(sum(full_image))
image_max=max(max(full_image));
range = min(hit_hist):1:max(max(hit_hist));
[X,Y] = meshgrid([1:1:4]);
% 9. Display the image along with a surface plot and a histogram of hits.
if windows == 2;
subplot(2,3,[1 2 4 5])
surf(X,Y,full_image)
title(['Surface plot of ',num2str(lower_limit),'-',num2str(upper_limit),' and ',
',num2str(lower_limit2),'-',num2str(upper_limit2),' keV'])
zlabel('Counts')
shading interp
set(gca,'YDir','reverse')
set(gca,'XDir','reverse')
subplot(2,3,3); imagesc(full_image,[0 max(max(full_image))]); colormap(gray);
title([num2str(lower_limit),'-',num2str(upper_limit),' and ',num2str(lower_limit2),'-',
',num2str(upper_limit2),' keV image'])
xlabel('Rear Strip #')
ylabel('Front Strip #')
set(gca,'XDir','reverse')
subplot(2,3,6), hist(hit_hist,range)
xlabel('Energy [keV]')
ylabel('Counts')
title('Energy Histogram')
else
subplot(2,3,[1 2 4 5])
surf(X,Y,full_image)
title(['Surface plot of ',num2str(lower_limit),'-',num2str(upper_limit),' keV'])
xlabel('Rear Strip #')
ylabel('Front Strip #')
zlabel('Counts')
shading interp
set(gca,'YDir','reverse')
set(gca,'XDir','reverse')
axis normal
subplot(2,3,3); imagesc(full_image,[0 max(max(full_image))]); colormap(gray);
title([num2str(lower_limit),'-',num2str(upper_limit),' keV image'])
xlabel('Rear Strip #')

```

```
ylabel('Front Strip #')
set(gca,'XDir','reverse')
subplot(2,3,6), hist(hit_hist,range)
xlabel('Energy [keV]')
ylabel('Counts')
title('Energy Histogram')
end
```

Appendix C. Resolution Measurement Spectra

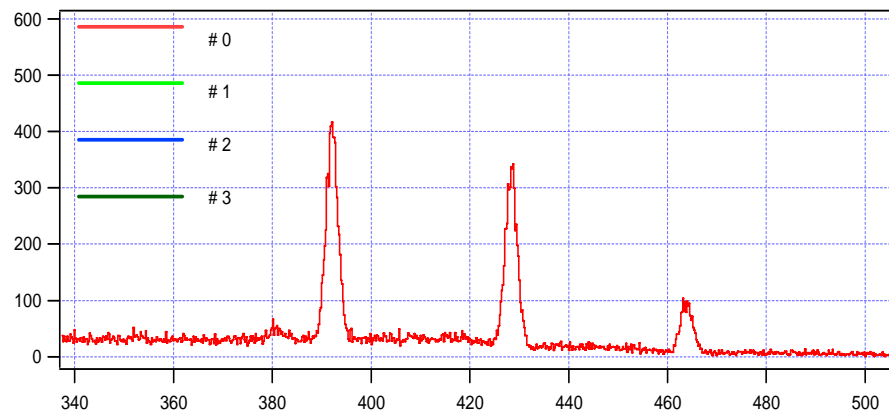


Figure 56: Strip F1 activated Sn spectrum

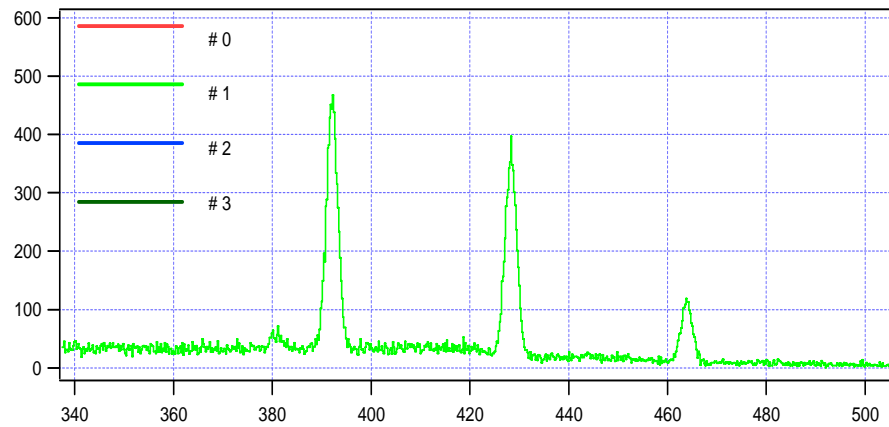


Figure 57: Strip F2 activated Sn spectrum

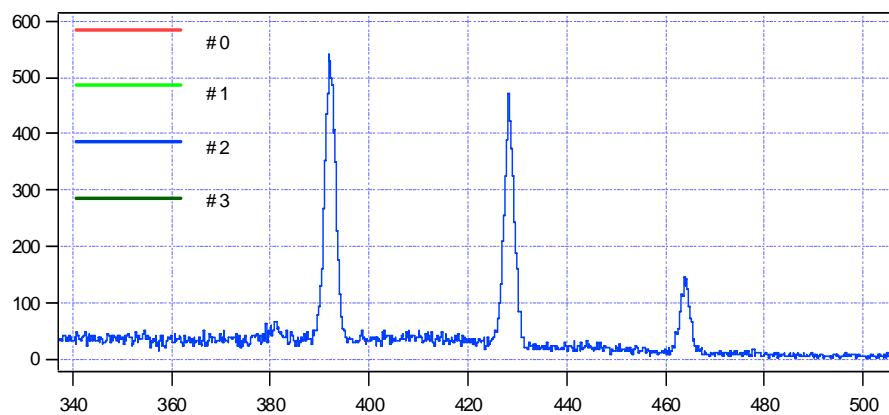


Figure 58: Strip F3 activated Sn spectrum

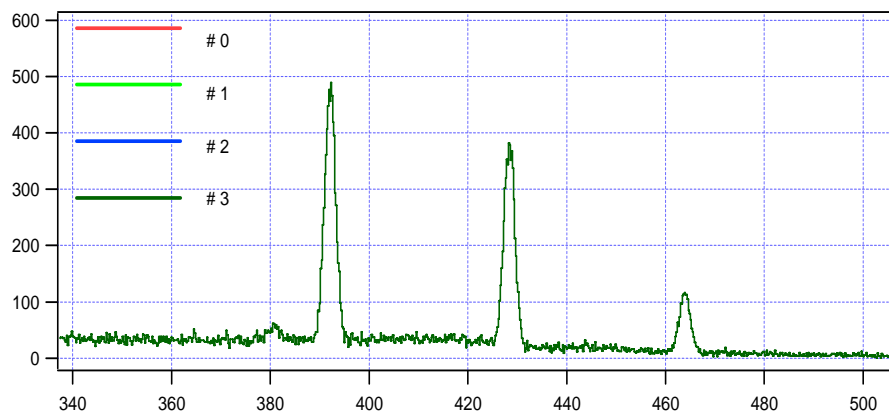


Figure 59: Strip F4 activated Sn spectrum

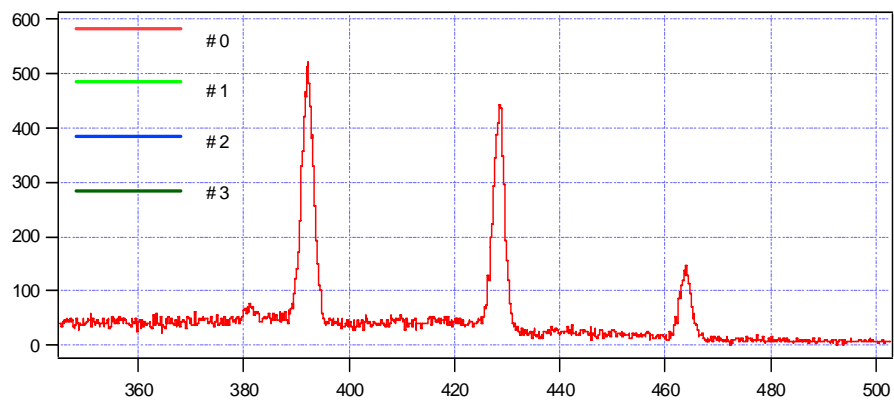


Figure 60: Strip R1 activated Sn spectrum

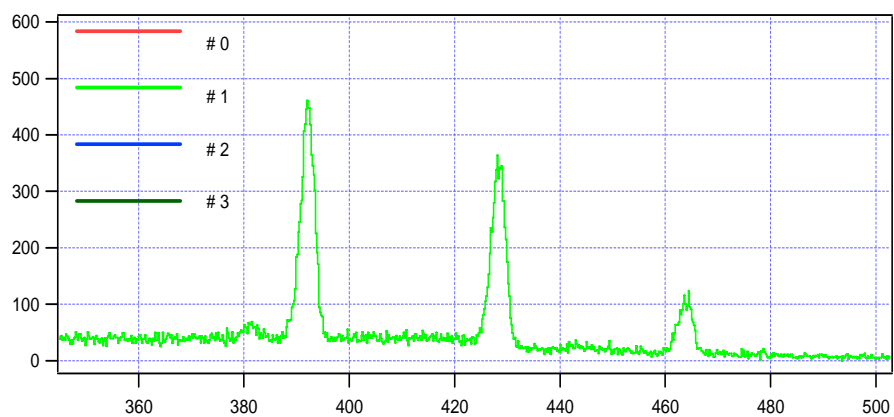


Figure 61: Strip R2 activated Sn spectrum

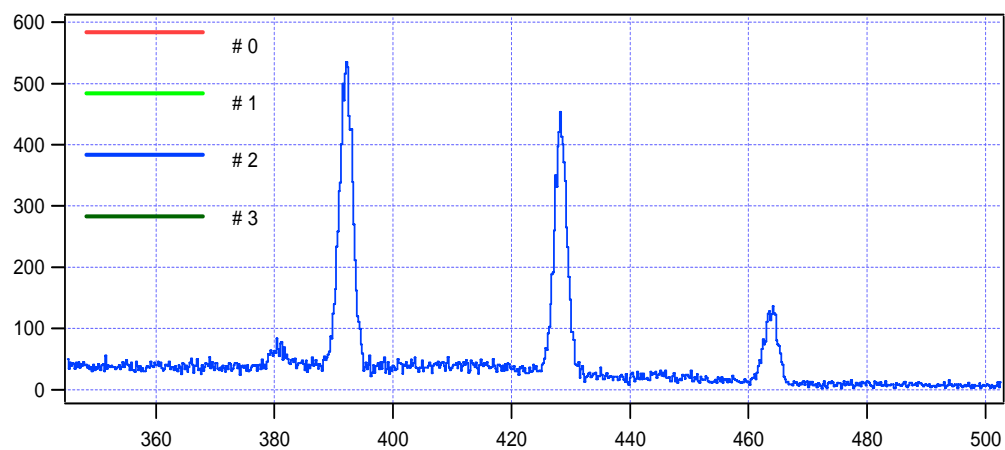


Figure 62: Strip R3 activated Sn spectrum

Bibliography

- [1] H.O. Anger, "Scintillation Camera," *Rev. Sci. Instrum*, vol. 29, pp. 27-33, 1958.
- [2] S. Fetter, T.B. Cochran, L. Grodzins, H.L. Lynch and M.S. Zucker, "Gamma-Ray Measurements of a Soviet Cruise-Missile Warhead," *Science*, vol. 248, pp. 828-834, 18 May 1990.
- [3] S. Fetter, V.A. Frolov, M. Miller, R. Mozley, O.F. Prilutsky, S.N. Rodionov and R.Z. Sagdeev, "Detecting Nuclear Weapons," *Science and Global Security*, vol. 1, pp. 225-302, 1990.
- [4] Idaho National Engineering & Environmental Laboratory, "Ge(Li)-Si(Li) Gamma Spectrum Catalogue <http://wastenot.inel.gov/gamma/data1.html>."
- [5] Jorway Corporation, Instruction Manual, Model 73A, SCSI Bus CAMAC Crate Controller.
- [6] G.F. Knoll, *Radiation Detection and Measurement*, New York: John Wiley & Sons, Inc., 2000.
- [7] J.D. Kurfess, W.N. Johnson, R.A. Kroeger, B.F. Philips and E.A. Wulf, "Development and applications of position-sensitive solid-state gamma ray detectors," *Nuclear Instruments and Methods in Physics Research A*, vol. 505, pp. 256-264, 2003.
- [8] Naval Research Laboratory, "Gamma and Cosmic Ray Astrophysics Branch <http://hese.nrl.navy.mil/gamma/detector/detector.htm>,"
- [9] M. B. Nelson, "Detection of Special Nuclear Material with High Purity Germanium and Mercuric Iodide Gamma Detectors," *Graduate School of Engineering and Management, Air Force Institute of Technology (AU), Wright-Patterson AFB OH*, March 2003.
- [10] ORTEC, High-purity Germanium Double-Sided Strip Detector -HPGeDSSD- Operating Manual.
- [11] ORTEC, Quad 4-Input Logic Unit Operating and Service Manual.
- [12] G. Rossi, J. Morse, and D. Protic, "Energy and Position Resolution of Germanium Microstrip Detectors at X-Ray Energies from 15 to 100 keV," *IEEE Transactions on Nuclear Science*, vol. 46, No. 3, pp. 765-771, 1999.
- [13] J. C. Russ, *The Image Processing Handbook*, New York: CRC Press, 2002.
- [14] C.V. Sulham, "Special Nuclear Material Imaging Using a High Purity Germanium Double Sided Strip Detector," *Graduate School of Engineering and Management, Air Force Institute of Technology (AU), Wright-Patterson AFB OH*, March 2004.

- [15] S. Vaughn, "Investigation of a Passive, Temporal, Neutron Monitoring System that Functions within the Confines of START I," *Graduate School of Engineering and Management, Air Force Institute of Technology (AU), Wright-Patterson AFB OH*, March 2003.
- [16] W-ie-Ne-R, NIM / CAMAC User's and Service-Manual.
- [17] X-ray Instrumentation Associates, DGF-4C Users Manual, Version 3.04.

Vita

Captain Fred D. Rothenbush Jr. was born in Owensboro, Kentucky, where he graduated from Daviess County High School. He entered the Army as a Nuclear Weapons Maintenance Technician and completed assignments with the 528th US Army Artillery Group at Cakmakli, Turkey and the 833rd Ordnance Company at Seneca Army Depot, New York. He then became an Explosive Ordnance Disposal Technician and was assigned to the 54th Ordnance Detachment (EOD) at Fort Monmouth, New Jersey. Next, he received an Army Green-to-Gold scholarship and attended Jackson State University. Upon completion of his Bachelor of Science degree in Physics, he was commissioned as a Second Lieutenant. He attended rotary wing flight training at Fort Rucker, Alabama, where he was trained to be a UH-60 Blackhawk pilot. From there, he served as a UH-60 Platoon Leader and Assistant Brigade Training Officer for the 25th Aviation Brigade at Schofield Barracks, Hawaii. Upon completion of the Army Aviation Captain Career Course at Fort Rucker, Alabama, he was assigned to the 1st Battalion, 58th Aviation Regiment at Ft. Bragg, North Carolina. While there, he served as the Battalion Logistics Officer, Headquarters and Headquarters Company Commander and Assistant Battalion Training Officer. He then entered the School of Engineering Physics, Air Force Institute of Technology at Wright-Patterson AFB, Ohio. Upon completion of his master's degree, he will be assigned as a physics instructor at the United States Military Academy at West Point, NY.

| REPORT DOCUMENTATION PAGE | | | | Form Approved OMB No. 074-0188 | |
|---|------------------|-----------------------------------|--------------------------------------|--|---|
| <p>The public reporting burden for this collection of information is estimated to average 1 hour per response, including the time for reviewing instructions, searching existing data sources, gathering and maintaining the data needed, and completing and reviewing the collection of information. Send comments regarding this burden estimate or any other aspect of the collection of information, including suggestions for reducing this burden to Department of Defense, Washington Headquarters Services, Directorate for Information Operations and Reports (0704-0188), 1215 Jefferson Davis Highway, Suite 1204, Arlington, VA 22202-4302. Respondents should be aware that notwithstanding any other provision of law, no person shall be subject to a penalty for failing to comply with a collection of information if it does not display a currently valid OMB control number.</p> <p>PLEASE DO NOT RETURN YOUR FORM TO THE ABOVE ADDRESS.</p> | | | | | |
| 1. REPORT DATE (DD-MM-YYYY) 13-June-2005 | | 2. REPORT TYPE Master's Thesis | | 3. DATES COVERED (From – To) March 2003 – June 2005 | |
| 4. TITLE AND SUBTITLE IMPROVED MULTINUCLIDE IMAGING OF SPECIAL NUCLEAR MATERIAL USING A HIGH PURITY GERMANIUM DOUBLE SIDED STRIP DETECTOR | | | | 5a. CONTRACT NUMBER | |
| | | | | 5b. GRANT NUMBER | |
| | | | | 5c. PROGRAM ELEMENT NUMBER | |
| 6. AUTHOR(S) Rothenbush, Fred D., Captain, USA | | | | 5d. PROJECT NUMBER 03379 | |
| | | | | 5e. TASK NUMBER | |
| | | | | 5f. WORK UNIT NUMBER | |
| 7. PERFORMING ORGANIZATION NAMES(S) AND ADDRESS(S) Air Force Institute of Technology Graduate School of Engineering and Management (AFIT/EN) 2950 Hobson Way, Building 640 WPAFB OH 45433-8865 | | | | 8. PERFORMING ORGANIZATION REPORT NUMBER AFIT/GNE/ENP/05-09 | |
| 9. SPONSORING/MONITORING AGENCY NAME(S) AND ADDRESS(ES) Defense Threat Reduction Agency (Attn: Dr. Mark Byers DTRA/TD) 8725 John J. Kingman Road Stop 6201 Fort Belvoir, VA 22060-6201 | | | | 10. SPONSOR/MONITOR'S ACRONYM(S) | |
| | | | | 11. SPONSOR/MONITOR'S REPORT NUMBER(S) | |
| 12. DISTRIBUTION/AVAILABILITY STATEMENT APPROVED FOR PUBLIC RELEASE; DISTRIBUTION UNLIMITED. | | | | | |
| 13. SUPPLEMENTARY NOTES | | | | | |
| 14. ABSTRACT <p>In the conduct of this research effort, neutron activated Sn sources and standard radioactive sources were used to simulate the gamma energy spectrum of a nuclear weapon pit. A converging hole collimator was designed, constructed, and mated with an HPGe Double Sided Strip Detector. A MATLAB image processing code was developed to produce a grayscale image of the sources. A variety of source configurations was examined to demonstrate the system's ability to obtain proper spatial distribution information for a multinuclide gamma emitting source. By replacing the converging hole collimator with a second detector array (as in a Compton camera) to improve detector efficiency, HPGe strip detectors may be used for the intended application of identifying the presence of a "spoofer" weapon pit consisting of multiple nuclide sources meant to mimic a real weapon pit.</p> | | | | | |
| 15. SUBJECT TERMS Gamma Spectroscopy, HPGe Strip Detector, Special Nuclear Material Imaging | | | | | |
| 16. SECURITY CLASSIFICATION OF: Unclassified | | | 17. LIMITATION OF ABSTRACT UU | 18. NUMBER OF PAGES 132 | 19a. NAME OF RESPONSIBLE PERSON Dr. Larry W. Burggraf, AFIT-ENP |
| a. REPORT U | b. ABSTRACT U | c. THIS PAGE U | | | 19b. TELEPHONE NUMBER (Include area code) (937) 255-6565, ext 4507 (lburggraf@afit.edu) |